Numerical Simulation of Surface Waves using Meshfree Methods

by

Subasha Wickramarachchi

A thesis
presented to the University of Waterloo
in fulfillment of the
thesis requirement for the degree of
Master of Mathematics
in
Applied Mathematics

Waterloo, Ontario, Canada, 2009

I hereby declare that I am the sole author of this thesis. This is a true copy of the thesis, including any required final revisions, as accepted by my examiners.

I understand that my thesis may be made electronically available to the public.

Abstract

Smoothed Particle Hydrodynamics (SPH) is a Lagrangian-based numerical method used for simulating problems in fluid and solid mechanics. In this thesis, a basic introduction to particle and Smoothed Particle (SP) approximations is given first. Application of SP approximations to Euler and Navier-Stokes equations is discussed, followed by an improvement to restore first order consistency in SPH. Then, simulations of 2D free-surface waves in a weakly incompressible fluid are conducted. If the artificial viscosity used is small, results indicate that the accuracy of SPH scheme is reasonably good; however, a low artificial viscosity leads to a rugged air-water interface. Furthermore, application of the LES filter used in [9] has negligible effects. It is also observed that the use of Renormalized SPH (R-SPH) increases diffusivity but does not increase accuracy significantly. Hence, for 2D surface waves in weakly incompressible fluids, basic SPH formulation without any modification is as good as the R-SPH or LES-SPH methods.

Acknowledgements

I express my sincere thanks to my supervisor, Prof. N. Lanson, for her guidance, patience, and for the resources made available to me. I also thank Prof. K. Lamb for his guidance in the absence of my supervisor. My thanks goes to Robyn Landers for providing technical support to tame the troublesome ifort compiler; his support saved a lot of time. Thank you Prof. Marek Stastna for showing me how to make a soliton, a simple but crucial step in my research. My thanks to Helen Warren for being an extraordinary graduate secretary. Special thanks to Prof. H. J. M. De Sterck, Prof. M. Stastna, and Prof. C. Devaud for reading this thesis. I also wish to express my thanks to all staff members, my colleagues, friends and my family members for providing an environment conducive to studies.

Contents

List of Tables

List of Figures

Chapter 1

Introduction

Fluids play crucial roles in nature. For example, the circulation of fluids distributes and stabilizes global temperatures. Fluids act as mediums in which matter chemically interacts, including interactions which most likely gave rise to life itself. Apart from essential roles fluids play in nature, fluids help in numerous other ways. In terms of transportation, air enables planes to fly, oceanic waters enable ships to sail, etc. Fluids not only give life, but at times they take life. Storms and volcanic eruptions often leave trails of destruction that sometimes last for hundreds of years. For centuries, people have been finding ways to control fluids. For example, people divert waterways for irrigation, flood control, or create dams for electricity generation. Thus, understanding fluid dynamics is important.

What is the most basic way we can understand fluid dynamics? Manipulating real fluids is the only sure way that we can understand fluid dynamics. But, currently, it is sometimes difficult to experiment with fluids. Going to the surf zone at a beach for studying may result in you being dragged out to the sea. Hands-on experimentation with larger phenomena such as storms is a lot more dangerous. Apart from dangers, it is sometimes difficult or impossible to carry out controlled experiments, especially at sub-planetary scales. Hence, there is an element of restriction in conducting real experiments. One way out of these difficult situations is to model fluids. In other words, we develop a mathematical model that correlates well with observations. Unfortunately, nature is highly complex, and almost all dynamics are stubbornly non-linear. Analytical insight into these non-linear problems is hard to come by. One way out of this situation is to look for numerical solutions.

Over the years, many different numerical methods have been employed to solve problems in fluid dynamics. One of the simplest methods is the Finite Difference Method (FDM), which is based on the Eulerian frame of reference. Often, in FDM, non-linear terms are handled by linearizing the problem to some degree. Thus, some of the non-linear effects are lost. Methods that are less robust but highly accurate are spectral methods. Spectral methods have the ability to easily handle non-linear terms. For elliptic equations, Finite Element Method (FEM) is often used. FEM is robust but is prone to mesh entanglement. Adaptive mesh generation for complex

geometries is also a challenge in FEM.

Compared to schemes based on the Eulerian frame of reference, Smoothed Particle Hydrodynamics (SPH), a numerical scheme based on the Lagrangian frame of reference, provides a good way of handling the non-linear term in Euler equations. That is, the use of characteristics to transform Euler equations to a system of Ordinary Differential Equations (ODEs) removes the non-linear advection term. SPH was first formulated by Lucy [24], Gingold and Monaghan [25] in 1977. SPH was first used to study phenomena in astrophysics; SPH has since been applied to a wide range of problems, including problems in fluid and solid mechanics.

Simulation of surface waves using SPH has been carried out by many researchers. One of the earliest simulations was done by Monaghan [17] in 1992: he tested the 2D dam breaking problem, generated surface waves by a piston-paddle, and studied solitary waves in a beach [18]. A more dynamic motion was studied by G. Oger et al. [26], where 2D wedge water entries were studied. A numerical simulation of inter-facial flows was studied by Andrea et al. [27]. Incompressible SPH simulation of wave breaking with turbulence using the $k-\epsilon$ model was carried out by Shao [28]. Edmond et al. [29] studied near-shore solitary wave mechanics using incompressible LES-SPH (SPH with the LES filter) simulations. Numerical modelling of water waves with SPH was carried out by Dalrymple et al. [9] for a weakly incompressible fluid using LES modelling.

In this thesis, I will first present the basic particle approximation of functions and Smoothed Particle (SP) approximation of derivatives. In Chapter 3, the application of SP approximation to Euler equations is discussed, and SPH is introduced. In Chapter 4, an improvement to SPH is discussed, an improvement called Renormalized-SPH. Chapter 5 focuses on the application of SPH to Navier-Stokes equations. Chapter 6 consists of 2D free-surface waves simulations. Most of the simulation focuses on solitary waves. The thesis ends with a conclusion discussing some of the results obtained and their implications for the use of SPH methods.

Chapter 2

Particle Approximations

Functions can be approximated in many ways. Two simple approximation methods are linear interpolation and approximation using step functions. Particle approximation of a function can be considered as an interpolation using the sifting property of the Dirac-delta function. Smoothed Particle (SP) approximation is an interpolation scheme using functions taken from smooth delta sequences. In this chapter, we look at how functions are approximated using the particle and SP methods.

2.1 Approximating an integral

Consider a function $f : \Omega \to \mathbb{R}$, where Ω is a bounded subset of $\mathbb{R}^n$ for some $n \in \mathbb{N}$. Let $P = \{\Omega_j : j \in I\}$, where $I = \{1, 2, 3, ..., m\}$, be a partition of Ω, i.e. $\cup_{j\in I}\Omega_j = \Omega$. Let $\omega_j = |\Omega_j|$ be the volume of Ω_j. Then the integral of f corresponding to the partition P is approximated as

$$\int_\Omega f(\mathbf{x})d\mathbf{x} \approx \sum_{j\in I} f(\mathbf{x}_j)\omega_j, \tag{2.1}$$

where $\mathbf{x}_j \in \Omega_j$ for each $j \in I$.

2.2 Approximating a function

Using the approximation of an integral (2.1) and the relation

$$f(\mathbf{x}) = \int_\Omega f(\mathbf{x}')\delta(\mathbf{x} - \mathbf{x}')d\mathbf{x}', \tag{2.2}$$

where $\delta(\mathbf{x})$ is the Dirac-delta function, the particle approximation f_h of the function f is given by

$$f_h(\mathbf{x}) = \sum_{j\in I} f(\mathbf{x}_j)\delta(\mathbf{x} - \mathbf{x}_j)\omega_j. \tag{2.3}$$

To approximate a function in terms of volumes in a Lagrangian frame of reference, assume that there is a function ϕ such that $\mathbf{x}(t) = \phi(\xi, t)$, where ξ is the position at $t = 0$. Then (2.2) can be written as

$$\begin{aligned} f(\mathbf{x}, t) &= \int_{\Omega(t)} f(\mathbf{x}', t)\delta(\mathbf{x} - \mathbf{x}')d\mathbf{x}' \\ &= \int_{\Omega(0)} f(\phi(\xi, t), t)\delta(\mathbf{x} - \phi(\xi, t))|J(\xi, t)|d\xi, \end{aligned} \tag{2.4}$$

where $J = \frac{\partial \phi}{\partial \xi}$ is the Jacobian of the transformation $\mathbf{x}(t) = \phi(\xi, t)$. If the initial partition P is uniform with volume $|\Omega_j| = \omega_j = h_1 h_2 ... h_n$, where h_i's are the dimensions of an n-dimensional hyper-rectangle, the spatially discretized approximation $f_h(\mathbf{x}, t)$ of (2.4) is given by

$$\begin{aligned} f_h(\mathbf{x}, t) &= \sum_{j \in I} f(\phi(\xi_j, t), t)\delta(\mathbf{x} - \phi(\xi_j, t))|J(\xi_j, t)|\omega_j \\ &= \sum_{j \in I} f(\phi(\xi_j, t), t)\delta(\mathbf{x} - \phi(\xi_j, t))\omega_j(t), \end{aligned} \tag{2.5}$$

where $\omega_j(t) = \omega_j |J(\xi_j, t)|$, $\Omega(t) = \phi(\Omega(0), t)$, and $\Omega(0) = \Omega$. A uniform partition in 2D with rectangles of dimensions h_1 and h_2 is shown in Figure 2.1; in the figure, "particles" refers to the points at which the function is evaluated.

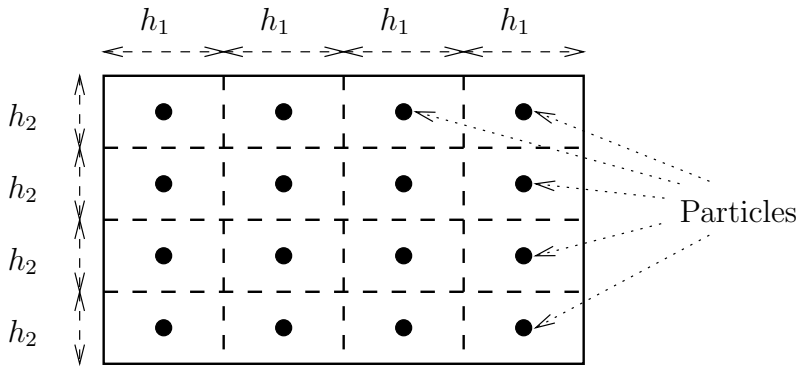

Figure 2.1: Regular grid in 2D

2.3 Smoothed Particle approximation

In hydrodynamic equations like Euler equations, spatial derivatives are present. Thus, in order to apply particle approximations to equations with spatial derivatives, particle approximation of derivatives is required. In (2.3) and (2.5), the derivative of a function is not defined in the classical sense. To circumvent this difficulty of evaluating the derivative, it is necessary to replace the Dirac-delta

function by a differentiable function, which approaches the Dirac-delta function in the limit. The approximation so obtained is called the Smoothed Particle (SP) approximation, and is given by

$$f_h^\epsilon(\mathbf{x}) \approx \int_{\mathbb{R}^n} f(\mathbf{x}')\psi_\epsilon(\mathbf{x}-\mathbf{x}')d\mathbf{x}', \tag{2.6}$$

where the regularized function ψ_ϵ satisfies the conditions

$$\begin{aligned} \lim_{\epsilon\to 0}\psi_\epsilon(\mathbf{x}) &= \delta(\mathbf{x}), & (2.7)\\ \int_{\mathbb{R}^n}\psi_\epsilon(\mathbf{x})d\mathbf{x} &= 1, & (2.8)\\ \psi_\epsilon(\mathbf{x}) &\in C^1(\mathbb{R}^n). & (2.9) \end{aligned}$$

ϵ is called the *smoothing length* and ψ_ϵ is referred to as the *kernel function*. In practice, two further conditions are imposed:

$$\begin{aligned} \psi_\epsilon &\in C_0^1(\mathbb{R}^n), & (2.10)\\ \psi_\epsilon(\mathbf{x}) &= \psi_\epsilon(\|\mathbf{x}\|). & (2.11) \end{aligned}$$

ψ_ϵ is chosen with compact support to reduce the computational domain involved when evaluating the integral - as shown in Figure 2.2, only the particles with label j inside the support ϵ_i of particle i contributes to the summations in Equations (2.3) and (2.5).

The term "Smoothed" in "Smoothed Particle" comes from the substitution of the smooth function $\psi_\epsilon(\mathbf{x})$ for the point (particle) function $\delta(\mathbf{x})$. As shown in Figure 2.2, the smoothing length defines the neighbours of a given particle i: 2.2(a) and 2.2(b) show the cases where particles are evenly and unevenly distributed respectively. Condition (2.9) allows the direct approximation of the derivative:

$$D_\alpha^\epsilon f(\mathbf{x}) \approx \int_{\mathbb{R}^n} f(\mathbf{x}')D_\alpha\psi_\epsilon(\mathbf{x}-\mathbf{x}')d\mathbf{x}', \tag{2.12}$$

where D_α is the partial derivative with respect to the coordinate index $\alpha \in \{1,2,3,...,n\}$. Observe that the differentiation is transferred to the kernel function. Replacing the Dirac-delta function δ by ψ_ϵ in (2.4), and using the discretization outlined in (2.5), the discretized SP approximation of a function and its derivative are given by

$$\begin{aligned} f_h^\epsilon(\mathbf{x},t) &= \sum_j f(\mathbf{x}_j,t)\psi_\epsilon(\mathbf{x}-\mathbf{x}_j)\omega_j(t), & (2.13)\\ D_{\alpha,h}^\epsilon f(\mathbf{x},t) &= \sum_j f(\mathbf{x}_j,t)D_\alpha\psi_\epsilon(\mathbf{x}-\mathbf{x}_j)\omega_j(t). & (2.14) \end{aligned}$$

Equation (2.14) may not give $D_{\alpha,h}^\epsilon 1 = 0$ when the particle distribution is inhomo-

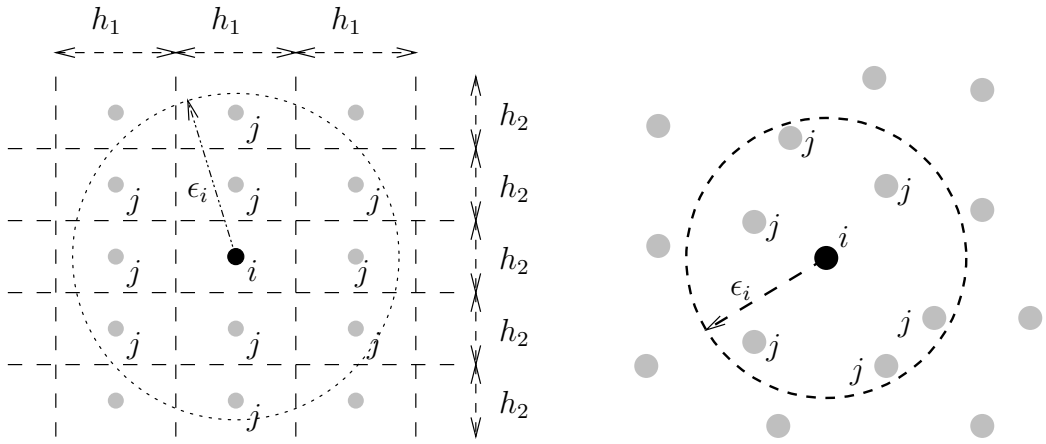

(a) Regular distribution (b) Irregular distribution

Figure 2.2: Smoothing length

geneous, but this flaw can be easily corrected:

$$D^{\epsilon}_{\alpha,h} f(\mathbf{x},t) = \sum_j \left(f(\mathbf{x}_j,t) - f(\mathbf{x},t)\right) D_\alpha \psi_\epsilon(\mathbf{x}-\mathbf{x}_j)\omega_j(t). \tag{2.15}$$

Using (2.15), the gradient and divergence operators can be written as

$$\nabla f(\mathbf{x},t) \approx \sum_j \left(f(\mathbf{x}_j,t) - f(\mathbf{x},t)\right) \nabla_{\mathbf{x}} \psi_\epsilon(\mathbf{x}-\mathbf{x}_j)\omega_j(t), \tag{2.16}$$

$$\nabla \cdot \mathbf{f}(\mathbf{x},t) \approx \sum_j \left(\mathbf{f}(\mathbf{x}_j,t) - \mathbf{f}(\mathbf{x},t)\right) \cdot \nabla_{\mathbf{x}} \psi_\epsilon(\mathbf{x}-\mathbf{x}_j)\omega_j(t). \tag{2.17}$$

2.3.1 Kernel functions

One of the earliest 1D kernel functions used was the modified Gaussian kernel

$$\psi_\epsilon(x) = \begin{cases} \frac{1}{a\epsilon\sqrt{\pi}} \exp\left(-\frac{1}{a^2}\left|\frac{x^2}{\epsilon^2}\right|\right), & \text{for } |x| \le \epsilon, \\ 0, & \text{otherwise,} \end{cases} \tag{2.18}$$

where a is a constant chosen small enough so that the normalization condition (2.8) is sufficiently accurate. One of the kernel functions commonly used is the cubic B-spline kernel defined by

$$\psi_\epsilon(\mathbf{x}) = \frac{C(n)}{\epsilon^n} \begin{cases} 1 - \frac{3}{2}\left|\frac{\mathbf{x}}{\epsilon}\right|^2 + \frac{3}{4}\left|\frac{\mathbf{x}}{\epsilon}\right|^3, & \text{for } |\mathbf{x}| \le \epsilon, \\ \frac{1}{4}\left(2 - \left|\frac{\mathbf{x}}{\epsilon}\right|\right)^3, & \text{for } \epsilon < |\mathbf{x}| \le 2\epsilon, \\ 0, & \text{for } |\mathbf{x}| > 2\epsilon, \end{cases} \tag{2.19}$$

where $n(=1,2,3)$ is the spatial dimension, and

$$C(n) = \begin{cases} 2/3, & \text{for } n = 1, \\ 10/7\pi, & \text{for } n = 2, \\ 1/\pi, & \text{for } n = 3 \end{cases} \tag{2.20}$$

is the constant used to impose the normalization condition (2.8). A plot of ψ_ϵ and its derivative for $n = 1$ are shown in Figure 2.3. Observe that ψ_ϵ is C^2. In this

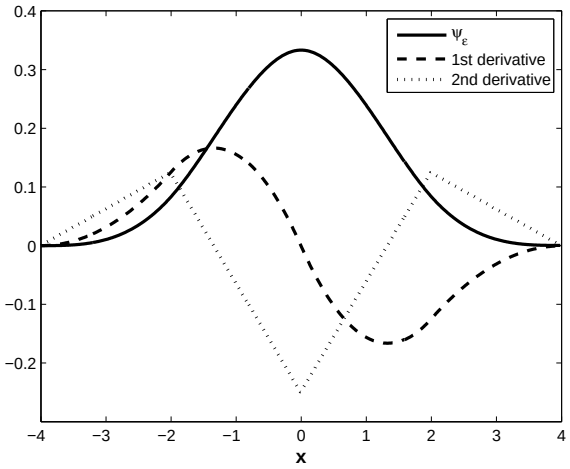

Figure 2.3: Kernel function and its derivatives

thesis, (2.19) is used for all simulations. A higher order spline kernel is [8]

$$\psi_\epsilon(\mathbf{x}) = \frac{C(n)}{\epsilon^n} \begin{cases} \left[3 - \left|\frac{\mathbf{x}}{\epsilon}\right|\right]^5 - 6\left[2 - \left|\frac{\mathbf{x}}{\epsilon}\right|\right]^5 + 15\left[1 - \left|\frac{\mathbf{x}}{\epsilon}\right|\right]^5, & \text{if } |\mathbf{x}| \le \epsilon, \\ \left[3 - \left|\frac{\mathbf{x}}{\epsilon}\right|\right]^5 - 6\left[2 - \left|\frac{\mathbf{x}}{\epsilon}\right|\right]^5, & \text{if } \epsilon < |\mathbf{x}| \le 2\epsilon, \\ \left[3 - \left|\frac{\mathbf{x}}{\epsilon}\right|\right]^5, & \text{if } 2\epsilon < |\mathbf{x}| \le 3\epsilon, \\ 0, & \text{if } |\mathbf{x}| > 2\epsilon. \end{cases} \tag{2.21}$$

2.3.2 Smoothing Length

The accuracy of (2.15)-(2.17) depends on the ratio ϵ/h, a measure of the number of particles within the smoothing length. For a uniform distribution of points in 2D, the curve with label "*" in Figure 2.4 shows how the accuracy of $\nabla_h x$ vary with the ratio ϵ/h. The curve with label "1" is the SP approximation 1_h of 1, obtained using (2.13). The computational efficiency of evaluating (2.13), (2.15)-(2.17) depends largely on the ratio ϵ/h: a higher ratio gives a slower execution time. Observe that the minimum ratio ϵ/h for which the accuracy of both $\nabla_h x$ and 1_h is highest is when $\epsilon/h \approx 1.2$; hence, $\epsilon/h = 1.2$ is used as the initial ($t = 0$) smoothing length in simulations. Furthermore, if ϵ/h varies, the accuracy varies. It is important to note

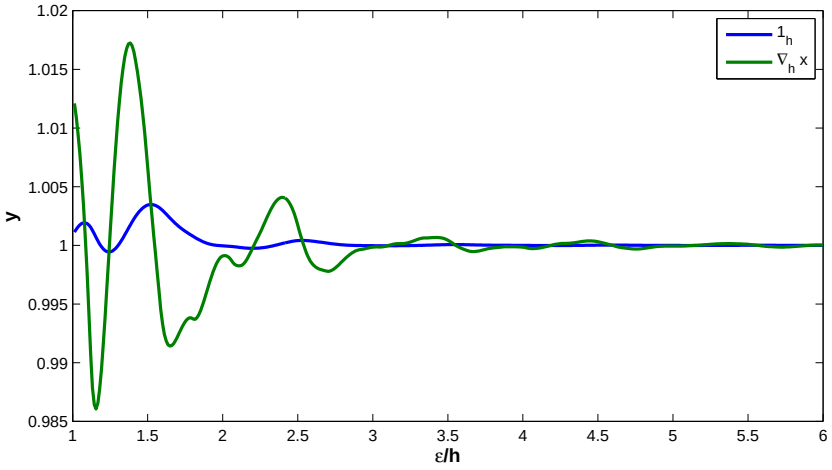

Figure 2.4: Variation of 1_h and $\nabla_h x$ with ϵ/h

that this reasoning is true only if points are uniformly distributed, an assumption which does not hold in most practical problems.

As we shall see in Chapter 3, for fluid flows, ideally, we require that a constant number of particles remain within the radius of influence (volume) associated with a particle, i.e. $\rho\epsilon^n = \textit{constant}$ along the flow, which on differentiating gives an expression for evolving the smoothing length:

$$\frac{d\epsilon_i}{dt} = -\frac{\epsilon_i}{n\rho_i}\frac{d\rho_i}{dt} = \frac{\epsilon_i}{n}\nabla \cdot \mathbf{u}, \tag{2.22}$$

where $\frac{d\rho_i}{dt} = -\rho_i \nabla \cdot \mathbf{u}_i$ is coming from Euler equations.

2.3.3 SP and centered FD approximations

There is a similarity between Smoothed Particle (SP) and centered Finite Difference (FD) approximations, a similarity which causes schemes based on SP approximations to be numerically unstable. Consider the SP approximation (2.14) in 1D, without time dependence:

$$D_h^\epsilon f(x_i) = \sum_j f(x_j) D\psi_{\epsilon_i}(x_i - x_j)\omega_j, \text{ for all } i \in I, \tag{2.23}$$

where $D = \frac{\partial}{\partial x}$, and D_h^ϵ is the SP approximation of the operator D. As shown in Figure 2.5, assume that particles are evenly distributed with inter-particle distance $x_{i+1} - x_i = \Delta l$; assume also that ϵ_i/h is small enough that only the particles i, $i+1$, and $i-1$ constitute the neighbours of the particle i. Then (2.23) simplifies

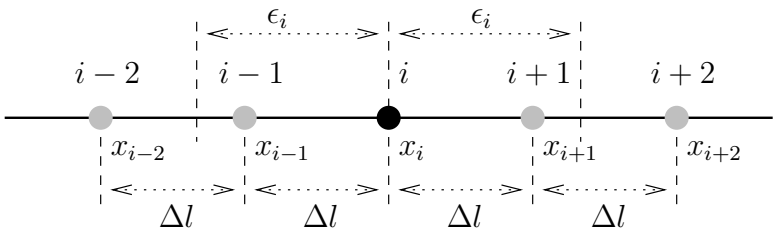

Figure 2.5: Regular grid in 1D

as follows:

$$\begin{aligned} D_h^\epsilon f(x_i) &= \sum_j f(x_j) D\psi_{\epsilon_i}(x_i - x_j)\Delta l \\ &= \left[f(x_{i+1}) D\psi_{\epsilon_i}(-\Delta l) + f(x_{i-1}) D\psi_{\epsilon_i}(\Delta l)\right]\Delta l \\ &= -\Delta l D\psi_{\epsilon_i}(\Delta l)\left[f(x_{i+1}) - f(x_{i-1})\right], \end{aligned} \tag{2.24}$$

since $D\psi_{\epsilon_i}(-\Delta l) = -D\psi_{\epsilon_i}(\Delta l)$. As shown in Figure 2.3, $D\psi_\epsilon(\Delta l) \leq 0$. Furthermore, as kernels (2.18) and (2.19) imply, the dimension $[D\psi_{\epsilon_i}(\Delta l)] = 1/L^2$, where L is the dimension of distance. Hence, SP approximation is similar to centered FD approximation. For the Gaussian kernel (2.18), (2.24) can be made exactly equal to the centered FD approximation if the shape parameter a is suitably chosen.

Chapter 3

Application to Euler Equations

An outline of the basic idea of this chapter is given here. Consider space to be composed of discrete particles or points. For example, consider a smooth 1D density distribution as shown in Figure 3.1. As we shall see in Section 3.1, the application of

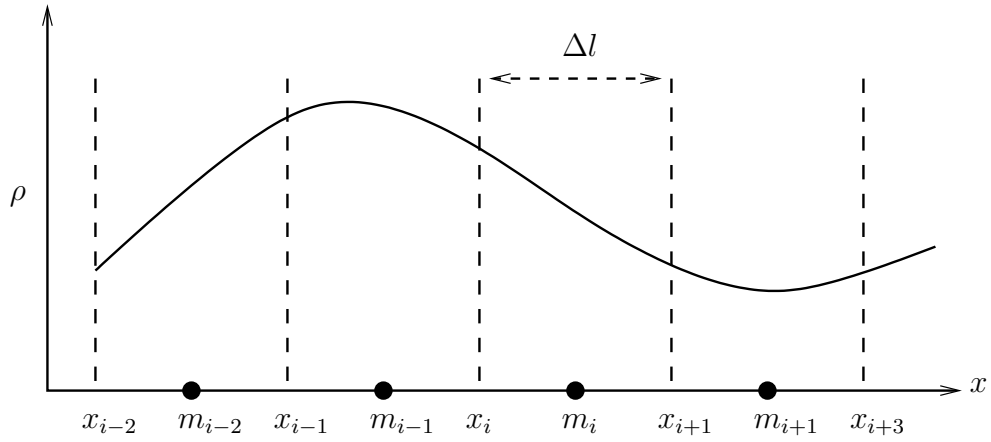

Figure 3.1: Particle approximation

particle approximation to Euler equations gives rise to a quantity which is equivalent to a particle with mass; for the 1D density distribution, particles with mass are shown as black dots with mass m_i in Figure 3.1. If the particles are uniformly distributed, the density distribution is approximated by assigning mass m_i and density ρ_i to each particle i as

$$m_i = \int_{x_i}^{x_i+\Delta l} \rho dx \quad \text{and} \quad \rho_i = \frac{m_i}{l}, \tag{3.1}$$

where $\Delta l = x_i - x_{i-1}$ for each i. However, in particle methods, the continuum is often approximated with an uneven distribution of equal-mass particles; thus, particle density is higher in the places where density is higher. If equal-mass particles are used, density ρ_i and length Δl_i associated with each particle i may be assigned

as

$$\rho_i = \rho(x_i) \quad \text{and} \quad \Delta l_i = \tfrac{m}{\rho_i}, \tag{3.2}$$

where m is the constant mass of each particle.

Now consider a situation where there is a time-dependent velocity field. Then

$$\frac{dx}{dt} = u \tag{3.3}$$

is used to update particle positions. Since the number of particles and the mass of each particle is fixed, mass conservation is an inherent property of the scheme. As shown in Figure 3.2, the volume associated with a particle changes depending on the closeness of neighbouring particles. Thus, the smoothing length ϵ is updated using (2.22):

$$\frac{d\epsilon}{dt} = \epsilon u_x. \tag{3.4}$$

Density is updated using

$$\frac{d\rho}{dt} = -\rho u_x. \tag{3.5}$$

Other quantities of interest are also expressed as ODEs; the set of ODEs is then solved using any scheme used to solve ODEs. In SPH, explicit schemes are often used; furthermore, 2-step Runge-Kutta scheme is most commonly used.

As a Lagrangian-based scheme, one of the advantages of SPH is its ability to track particle paths. As we will see in the Section 3.1, SPH is applied to Euler equations without linearizing, thus enabling the capture of non-linear effects.

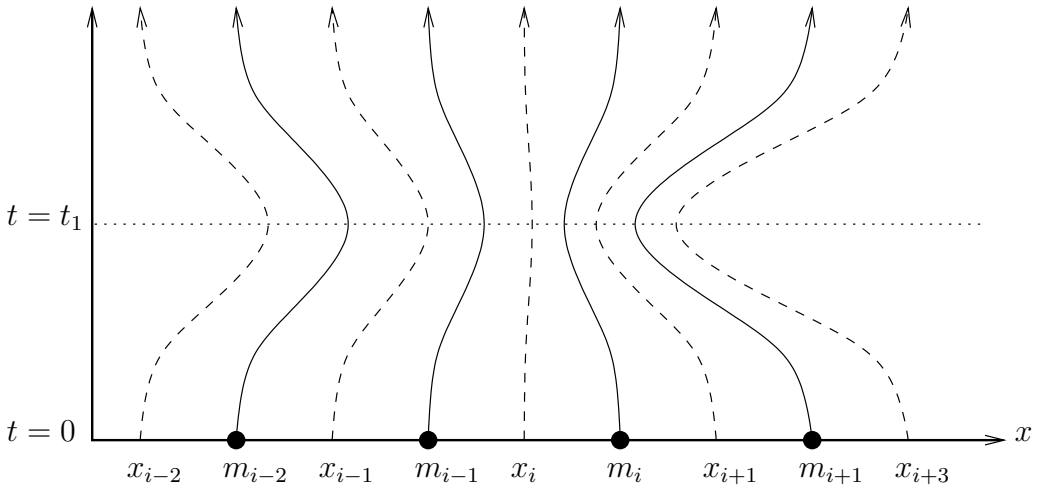

Figure 3.2: Particle evolution

3.1 Direct particle approximation of Euler equations

Euler equations are given by

$$\begin{aligned} \frac{d\rho}{dt} &= -\rho \nabla \cdot \mathbf{u}, && (3.6) \\ \frac{d\mathbf{u}}{dt} &= -\frac{\nabla p}{\rho}, && (3.7) \\ \frac{de}{dt} &= -\frac{p}{\rho} \nabla \cdot \mathbf{u}, && (3.8) \end{aligned}$$

where ρ is the density, $\mathbf{u}$ is the velocity, p is the pressure, and e is the specific internal energy. Let $\rho_i(t) = \rho(\mathbf{x}_i(t), t)$ and $\mathbf{u}_i(t) = \mathbf{u}(\mathbf{x}_i(t), t)$ be the density and velocity at a point $\mathbf{x}_i(t) = \phi(\xi_i, t)$. If $\mathbf{x}(t) = \phi(\xi, t)$ is invertible and C^2, we have

$$J(\xi, t) > 0 \quad \text{and} \quad \tfrac{\partial J}{\partial t}(\xi, t) = (\nabla \cdot u)\, J(\xi, t). \tag{3.9}$$

Thus,

$$\begin{aligned} \frac{d}{dt}(\omega_i(t)\rho_i(t)) &= \omega_i \left[\rho_i(t) \frac{\partial J}{\partial t}(\xi_i, t) + J(\xi_i, t) \frac{d\rho_i}{dt} \right] \\ &= \omega_i \left[\rho_i(t) J(\xi_i, t) \nabla \cdot \mathbf{u}_i(t) + J(\xi_i, t) \frac{d\rho_i}{dt} \right] \\ &= \omega_i J(\xi_i, t) \left[\frac{d\rho_i}{dt} + \rho_i(t) \nabla \cdot \mathbf{u}_i(t) \right] = 0, \qquad (3.10) \end{aligned}$$

by (3.6). Hence,

$$\omega_i(t)\rho_i(t) = constant, \tag{3.11}$$

following the flow. Since (3.11) has the dimension of mass, it is associated with the mass of the particle initially ($t = 0$) at ξ_i. Thus, let $m_i = \omega_i(t)\rho_i(t) = \omega_i(0)\rho_i(0)$, p_i and e_i be the mass, pressure, and internal energy of particle i. Then (3.6)-(3.8) take the discretized form

$$\begin{aligned} \frac{d\rho_i}{dt} &= -\sum_j \frac{\rho_i m_j}{\rho_j} (\mathbf{u}_j - \mathbf{u}_i) \cdot \nabla_{\mathbf{x}_i} \psi_{\epsilon_i}(\mathbf{x}_i - \mathbf{x}_j), && (3.12) \\ \frac{d\mathbf{u}_i}{dt} &= -\sum_j \frac{m_j}{\rho_i \rho_j} (p_j - p_i) \nabla_{\mathbf{x}_i} \psi_{\epsilon_i}(\mathbf{x}_i - \mathbf{x}_j), && (3.13) \\ \frac{de_i}{dt} &= -\sum_j \frac{p_i m_j}{\rho_i \rho_j} (\mathbf{u}_j - \mathbf{u}_i) \cdot \nabla_{\mathbf{x}_i} \psi_{\epsilon_i}(\mathbf{x}_i - \mathbf{x}_j), && (3.14) \end{aligned}$$

when the particle approximations (2.16) and (2.17) are applied. The smoothing length is updated using (2.22):

$$\begin{aligned}\frac{d\epsilon_i}{dt} &= \frac{\epsilon_i}{n}\nabla\cdot\mathbf{u}_i \\ &= -\frac{\epsilon_i}{n}\sum_j \frac{\rho_i m_j}{\rho_j}(\mathbf{u}_j-\mathbf{u}_i)\cdot\nabla_{\mathbf{x}_i}\psi_{\epsilon_i}(\mathbf{x}_i-\mathbf{x}_j). \end{aligned} \tag{3.15}$$

Note that any SPH formulation can be used for the part $\nabla\cdot\mathbf{u}$ in (3.15); here, we made use of the discretized part $\nabla\cdot\mathbf{u}$ of (3.12).

3.1.1 Artificial viscosity

In Section 2.3.2, for the special case of equi-distributed particles, SP approximation of derivatives was shown to be similar to the centered FD scheme. Furthermore, since explicit time discretization will be used, numerical diffusivity must be added to stabilize the SPH scheme (3.12)-(3.14). In addition to stabilizing the scheme, a suitable numerical diffusivity will help resolve shocks or discontinuities by smoothing discontinuities over several inter-particle distances (equivalent to several grid spacings in FD schemes). In 1D, heuristically, the second derivative of a function f can be approximated as

$$\begin{aligned} D^2_{\epsilon_i} f(x_i) &= \sum_j Df(x_j) D\psi_{\epsilon_i}\omega_j \\ &\approx \sum_j \frac{f(x_j)-f(x_i)}{x_j-x_i} D\psi_{\epsilon_i}\omega_j \\ &= \sum_j \frac{m_j}{\rho_j}\frac{f_{ji}}{x_{ji}} D\psi_{\epsilon_i}, \end{aligned} \tag{3.16}$$

where $f_{ji} = f(x_j) - f(x_i)$ and $x_{ji} = x_j - x_i$. In higher dimensions, by a similar argument, we can show that

$$\sum_j \frac{m_j}{\rho_j}\frac{\mathbf{f}_{ji}\cdot\mathbf{x}_{ji}}{\|\mathbf{x}_{ji}\|^2}\nabla_{\mathbf{x}_i}\psi_{\epsilon_i}(\mathbf{x}_{ij}) \tag{3.17}$$

is a term containing diffusivity (see Appendix A).

In SPH, the commonly used numerical diffusivity is equivalent to the diffusivity introduced for FD schemes by Von Neumann and Richtmyer [21]. Von Neumann-Richtmyer diffusivity is introduced as a pseudo-viscous pressure added to the physical pressure (see Appendix B). Von Neumann-Richtmyer diffusivity for SPH is given by

$$\Pi_{ij} = \begin{cases} -\alpha\bar{c}_{ij}\bar{\rho}_{ij}\mu_{ij} + \beta\bar{\rho}_{ij}\mu_{ij}^2, & \text{for } \mathbf{u}_{ij}\cdot\mathbf{x}_{ij} < 0, \\ 0, & \text{for } \mathbf{u}_{ij}\cdot\mathbf{x}_{ij} \geq 0, \end{cases} \tag{3.18}$$

where

$$\mu_{ij} = \frac{\bar{\epsilon}_{ij}\mathbf{u}_{ij}\cdot\mathbf{x}_{ij}}{\|\mathbf{x}_{ij}\|^2+\eta^2}, \tag{3.19}$$

and $\bar{c}_{ij}$, $\bar{\rho}_{ij}$, and $\bar{\epsilon}_{ij}$ are the average speed, density, and smoothing length of the particles i and j; $\alpha > 0$, $\beta > 0$, and η are constants, η is used to remove a possible singularity as a result of $\|\mathbf{x}_{ij}\| \approx 0$, which occur if two particles are close to each other. If $\beta = 0$, the artificial diffusivity given by (3.18) can be considered as (3.17) with the restriction $\mathbf{u}_{ji}\cdot\mathbf{x}_{ji} \le 0$ to satisfy the entropy condition (see Section 3.1.3). Note that

$$\begin{array}{rlll} \Pi_{ij} & > 0, & \text{if} & \mathbf{u}_{ij}\cdot\mathbf{x}_{ij} < 0, \quad \text{(approaching particles)} \\ & = 0, & \text{if} & \mathbf{u}_{ij}\cdot\mathbf{x}_{ij} \ge 0, \quad \text{(receding particles).} \end{array} \tag{3.20}$$

The final equations with the artificial viscosity are

$$\frac{d\rho_i}{dt} = -\sum_j \frac{\rho_i m_j}{\rho_j}(\mathbf{u}_j-\mathbf{u}_i)\cdot\nabla_{\mathbf{x}_i}\psi_{\epsilon_i}(\mathbf{x}_i-\mathbf{x}_j), \tag{3.21}$$

$$\frac{d\mathbf{u}_i}{dt} = -\sum_j \frac{m_j}{\rho_i\rho_j}(p_j-p_i+\Pi_{ij})\nabla_{\mathbf{x}_i}\psi_{\epsilon_i}(\mathbf{x}_i-\mathbf{x}_j), \tag{3.22}$$

$$\frac{de_i}{dt} = -\sum_j \frac{m_j}{\rho_i\rho_j}\left(p_i+\frac{1}{2}\Pi_{ij}\right)(\mathbf{u}_j-\mathbf{u}_i)\cdot\nabla_{\mathbf{x}_i}\psi_{\epsilon_i}(\mathbf{x}_i-\mathbf{x}_j), \tag{3.23}$$

$$\frac{d\epsilon_i}{dt} = -\frac{\epsilon_i}{n}\sum_j \frac{\rho_i m_j}{\rho_j}(\mathbf{u}_j-\mathbf{u}_i)\cdot\nabla_{\mathbf{x}_i}\psi_{\epsilon_i}(\mathbf{x}_i-\mathbf{x}_j). \tag{3.24}$$

3.1.2 Conservation properties

It is shown here that Equations (3.21)-(3.23) do not conserve linear momentum, angular momentum, or energy.

Consider a domain Ω. Suppose that Ω is discretized using N points. Let $\rho_i = \rho(\mathbf{x}_i(t),t)$ and $\mathbf{u}_i = \mathbf{u}(\mathbf{x}_i(t),t)$. Then the rate of change of linear momentum

$$\begin{aligned} \frac{d}{dt}\int_\Omega \rho(\mathbf{x},t)\mathbf{u}(\mathbf{x},t)d\mathbf{x} &= \frac{d}{dt}\sum_{i=1}^N \rho_i\mathbf{u}_i\omega_i(t) \\ &= \sum_{i=1}^N\left[\rho_i\omega_i(t)\frac{d\mathbf{u}_i}{dt}+\mathbf{u}_i\frac{d}{dt}(\rho_i\omega_i(t))\right] \\ &= \sum_{i=1}^N m_i\frac{d\mathbf{u}_i}{dt}, \end{aligned} \tag{3.25}$$

since $\frac{d}{dt}(\rho_i\omega_i(t)) = \frac{dm_i}{dt} = 0$. Similar procedures give expressions for the rate of change of angular momentum and total energy. Hence, the global conservation of linear momentum, angular momentum, and energy for a N-particle system can be

stated as

$$\frac{d}{dt}\left(\sum_{i=1}^{N} m_i \mathbf{u}_i\right) = 0, \tag{3.26}$$

$$\frac{d}{dt}\left(\sum_{i=1}^{N} m_i \mathbf{x}_i \times \mathbf{u}_i\right) = 0, \tag{3.27}$$

$$\frac{d}{dt}\left(\sum_{i=1}^{N} m_i E_i\right) = 0, \tag{3.28}$$

where $E_i = \rho e_i + \frac{1}{2}\mathbf{u}_i \cdot \mathbf{u}_i$ is the total energy and e_i is the internal energy of particle i.

If the conservation of linear momentum holds for a N-particle system, it should necessarily hold for a 2-particle system. We will show that (3.26)-(3.28) does not hold for a 2-particle system. For clarity, let us consider (3.21)-(3.23) without the artificial viscosity. Consider a system consisting of two particles i_1 and i_2 at positions $\mathbf{x}_{i_1}(t)$ and $\mathbf{x}_{i_2}(t)$. Assume that both particles are of equal mass m, and have the same smoothing length ϵ. Then the rate of change of momentum for the system is given by

$$\begin{aligned}\frac{d}{dt}\left(\sum_{i=1}^{2} m_i \mathbf{u}_i\right) &= -\sum_{i=1}^{2}\sum_{j=1}^{2} \frac{m_i m_j}{\rho_i \rho_j}\left(p_j - p_i\right)\nabla_{\mathbf{x}_i}\psi_\epsilon(\mathbf{x}_i - \mathbf{x}_j) \\ &= -2\frac{m^2}{\rho_{i_1}\rho_{i_2}}(p_{i_2} - p_{i_1})\nabla_{\mathbf{x}_{i_1}}\psi_\epsilon(\mathbf{x}_{i_1} - \mathbf{x}_{i_2}),\end{aligned} \tag{3.29}$$

which is zero only if $p_{i_2}(\mathbf{x}_{i_2}(t), t) = p_{i_1}(\mathbf{x}_{i_1}(t), t)$ as $\mathbf{x}_{i_1}(t) \neq \mathbf{x}_{i_2}(t)$. Physically, this condition is satisfied only if the pressure gradient vanishes. Therefore, linear momentum is not conserved in general. The problem that led to the lack of the conservation of momentum and energy can be seen if we consider forces that each particle experience. The force $F_{i_1}(i_2)$ exerted on particle i_{i_1} by i_{i_2} is given by

$$\begin{aligned}F_{i_1}(i_2) &= m\frac{d\mathbf{u}_{i_2}}{dt} = \frac{1}{\rho_{i_1}\rho_{i_2}}\left(p_{i_2} - p_{i_1}\right)\nabla_{\mathbf{x}_{i_1}}\psi_\epsilon(\mathbf{x}_{i_1} - \mathbf{x}_{i_2}) \\ &= \frac{(p_{i_2} - p_{i_1})}{\rho_{i_1}\rho_{i_2}}\frac{(\mathbf{x}_{i_1} - \mathbf{x}_{i_2})}{\|\mathbf{x}_{i_1} - \mathbf{x}_{i_2}\|}\frac{1}{\epsilon}\frac{d}{dr}\psi_\epsilon(r),\end{aligned} \tag{3.30}$$

where $r = \|\mathbf{x}_{i_1} - \mathbf{x}_{i_2}\|$. The force $F_{i_2}(i_1)$ exerted on particle i_{i_2} by i_{i_1} is

$$\begin{aligned}F_{i_2}(i_1) &= m\frac{d\mathbf{u}_{i_1}}{dt} = \frac{1}{\rho_{i_2}\rho_{i_1}}\left(p_{i_1} - p_{i_2}\right)\nabla_{\mathbf{x}_{i_2}}\psi_\epsilon(\mathbf{x}_{i_2} - \mathbf{x}_{i_1}) \\ &= \frac{(p_{i_1} - p_{i_2})}{\rho_{i_2}\rho_{i_1}}\frac{(\mathbf{x}_{i_2} - \mathbf{x}_{i_1})}{\|\mathbf{x}_{i_2} - \mathbf{x}_{i_1}\|}\frac{1}{\epsilon}\frac{d}{dr}\psi_\epsilon(r),\end{aligned} \tag{3.31}$$

where $r = \|\mathbf{x}_{i_2} - \mathbf{x}_{i_1}\|$. Then $F_{i_2}(i_1) = F_{i_1}(i_2)$, but the forces act in the same direction when there is a pressure difference. Magnitude of the forces will also

be different if the two particles had different smoothing lengths. According to Newton's third law of motion, the forces are expected to be equal in magnitude and opposite in direction. If the pressure term was symmetric in i_1 and i_2, then the forces will be in opposite directions. In addition, if the smoothing length ϵ is symmetric in i_1 and i_2, then the forces are of the same magnitude.

The rate of change of angular momentum is

$$\begin{aligned}\frac{d}{dt}\left(\sum_{i=1}^{2} m_i \mathbf{u}_i \times \mathbf{x}_i\right) &= \sum_{i=1}^{2} m_i \frac{d\mathbf{u}_i}{dt} \times \mathbf{x}_i \\ &= \frac{m^2}{\rho_{i_1}\rho_{i_2}}(p_{i_1} - p_{i_2})(\mathbf{x}_{i_1} + \mathbf{x}_{i_2}) \times \nabla_{\mathbf{x}_{i_1}} \psi_\epsilon(\mathbf{x}_{i_1} - \mathbf{x}_{i_2}) \\ &= \frac{m^2}{\rho_{i_1}\rho_{i_2}}(p_{i_1} - p_{i_2}) \frac{(\mathbf{x}_{i_1} + \mathbf{x}_{i_2}) \times (\mathbf{x}_{i_1} - \mathbf{x}_{i_2})}{\|\mathbf{x}_{i_1} - \mathbf{x}_{i_2}\|} \frac{1}{\epsilon} \frac{d}{dr} \psi_\epsilon(r),\end{aligned} \tag{3.32}$$

where $r = \|\mathbf{x}_{i_1} - \mathbf{x}_{i_2}\|$. Again, (3.32) is not necessarily zero, and we can see that the problem can be resolved if the pressure term is symmetric in i_1 and i_2. The rate of change of total energy is given by

$$\begin{aligned}\frac{d}{dt}\left(\sum_{i=1}^{2} m_i E_i\right) &= \sum_{i=1}^{2} m_i \frac{de_i}{dt} + \sum_{i=1}^{2} m_i \mathbf{u}_i \cdot \frac{d\mathbf{u}_i}{dt} \\ &= -\sum_{i=1}^{2}\sum_{j=1}^{2} \frac{m_i m_j}{\rho_i \rho_j}(p_i \mathbf{u}_j + p_j \mathbf{u}_i - 2p_i \mathbf{u}_i) \cdot \nabla_{\mathbf{x}_i} \psi_\epsilon(\mathbf{x}_i - \mathbf{x}_j) \\ &= -\frac{m^2}{\rho_{i_1}\rho_{i_2}}(p_{i_1}\mathbf{u}_{i_1} - p_{i_2}\mathbf{u}_{i_2}) \cdot \nabla_{\mathbf{x}_{i_1}} \psi_\epsilon(\mathbf{x}_{i_1} - \mathbf{x}_{i_2}),\end{aligned} \tag{3.33}$$

which is not necessarily zero.

3.1.3 Entropy

Particles must satisfy the second law of thermodynamics. The second law of thermodynamics for reversible processes can be stated as

$$T\frac{dS}{dt} = \frac{dQ}{dt}, \tag{3.34}$$

where S is the entropy, Q is the heat energy, and T is the thermodynamic temperature. The first law of thermodynamics can be stated as

$$\frac{dQ}{dt} = \frac{de}{dt} + \frac{dW}{dt}, \tag{3.35}$$

where e is the internal energy and W is the work done on the system. Using (3.34), (3.35), (3.21), and (3.23), for a particle i,

$$\begin{aligned}
\frac{dQ_i}{dt} &= \frac{de_i}{dt} + \frac{dW}{dt} = \frac{de_i}{dt} - \frac{p_i}{\rho_i^2}\frac{d\rho_i}{dt} \\
&= \frac{1}{2}\sum_j \frac{m_j}{\rho_i \rho_j}\Pi_{ij}\left(\mathbf{u}_i - \mathbf{u}_j\right) \cdot \nabla_{\mathbf{x}_i}\psi_{\epsilon_{ij}}(\mathbf{x}_i - \mathbf{x}_j) \\
&= \frac{1}{2}\sum_j \frac{m_j}{\rho_i \rho_j}\Pi_{ij}\left(\mathbf{u}_i - \mathbf{u}_j\right) \cdot \frac{\mathbf{x}_i - \mathbf{x}_j}{\|\mathbf{x}_i - \mathbf{x}_j\|}\frac{1}{\epsilon}\frac{d}{dr}\psi_\epsilon(r) \\
&\geq 0,
\end{aligned} \tag{3.36}$$

which follows from

$$\frac{d}{dr}\psi_\epsilon(r) \leq 0, \tag{3.37}$$

and from (3.20) as

$$\begin{array}{lll}
\Pi_{ij}\left(\mathbf{u}_{ij} \cdot \mathbf{x}_{ij}\right) & < 0 \quad \text{if} \quad & \mathbf{u}_{ij} \cdot \mathbf{x}_{ij} < 0 \\
& = 0 \quad \text{if} \quad & \mathbf{u}_{ij} \cdot \mathbf{x}_{ij} \geq 0 \quad ,
\end{array} \tag{3.38}$$

where $x_{ij} = \mathbf{x}_i - \mathbf{x}_j$ and $r = \|\mathbf{x}_i - \mathbf{x}_j\|$.

3.2 Equations with conservative properties

Equations that guarantee the exact conservation of linear momentum, angular momentum, and energy of the discretized SPH equations can be derived. Conservation of momentum is guaranteed by deriving the momentum equation as follows:

$$\begin{aligned}
\frac{d\mathbf{u}}{dt} &= -\frac{\nabla p}{\rho} \\
&= -\left[\nabla\left(\frac{p}{\rho}\right) + \frac{p}{\rho^2}\nabla\rho\right]. \qquad (3.39) \\
\Rightarrow \frac{d\mathbf{u}_i}{dt} &= -\sum_j m_j\left(\frac{p_j}{\rho_j^2} + \frac{p_i}{\rho_i^2}\right)\nabla_{\mathbf{x}_i}\psi_{\epsilon_i}(\mathbf{x}_i - \mathbf{x}_j). \qquad (3.40)
\end{aligned}$$

An energy equation that conserves energy can be obtained as follows. First derive the energy equation as

$$\begin{aligned}
\frac{de}{dt} &= -\frac{p}{\rho}\nabla \cdot \mathbf{u} \\
&= -\left(\frac{p}{\rho^2}\right)\rho\nabla \cdot \mathbf{u}
\end{aligned}$$

$$= -\left(\frac{p}{\rho^2}\right)\left[\nabla\cdot(\rho\mathbf{u}) - \mathbf{u}\nabla\rho\right]. \tag{3.41}$$

$$\Rightarrow \frac{de_i}{dt} = \frac{p_i}{\rho_i^2}\sum_j m_j \mathbf{u}_{ij}\cdot\nabla_{\mathbf{x}_i}\psi_{\epsilon_i}(\mathbf{x}_i - \mathbf{x}_j). \tag{3.42}$$

Now derive the discretized energy equation as

$$\frac{de}{dt} = -\frac{p}{\rho}\nabla\cdot\mathbf{u}$$

$$= -\left[\nabla\cdot\left(\frac{p\mathbf{u}}{\rho}\right) + \mathbf{u}\cdot\nabla\left(\frac{p}{\rho}\right)\right]. \tag{3.43}$$

$$\Rightarrow \frac{de_i}{dt} = -\sum_j \frac{p_j m_j}{\rho_j^2}\mathbf{u}_{ji}\cdot\nabla_{\mathbf{x}_i}\psi_{\epsilon_i}(\mathbf{x}_i - \mathbf{x}_j). \tag{3.44}$$

Now taking the average of (3.42) and (3.44), we get

$$\frac{de_i}{dt} = -\frac{1}{2}\sum_j m_j\left(\frac{p_j}{\rho_j^2} + \frac{p_i}{\rho_i^2}\right)\mathbf{u}_{ji}\cdot\nabla_{\mathbf{x}_i}\psi_{\epsilon_i}(\mathbf{x}_i - \mathbf{x}_j), \tag{3.45}$$

where $\mathbf{u}_{ji} = \mathbf{u}_j - \mathbf{u}_i$. One further modification is required to ensure conservation of momentum and energy. The modification is to ensure that the gradient of the kernel is antisymmetric with respect to $\mathbf{x}_i - \mathbf{x}_j$, i.e. gradient of the kernel must satisfy

$$\nabla_{\mathbf{x}_i}\psi_{\epsilon_{ij}}(\mathbf{x}_i - \mathbf{x}_j) = -\nabla_{\mathbf{x}_j}\psi_{\epsilon_{ij}}(\mathbf{x}_j - \mathbf{x}_i). \tag{3.46}$$

To enforce antisymmetry, we replace ϵ_i by $\epsilon_{ij} = \frac{1}{2}(\epsilon_i + \epsilon_j)$. The proofs that (3.40) and (3.45) conserve linear momentum, angular momentum, and energy are given in Section 3.2.1. Many other discretized SPH forms of Euler equations can be derived.

Depending on the form of the energy equation, the discretized form of the continuity equation is derived so that the entropy condition is satisfied. Here, we derive a suitable continuity equation by using the discretized part $p\nabla\cdot\mathbf{u}/\rho$ of (3.45) :

$$\frac{d\rho}{dt} = -\rho\nabla\cdot\mathbf{u} = -\frac{\rho^2}{p}\left(\frac{p}{\rho}\nabla\cdot\mathbf{u}\right). \tag{3.47}$$

$$\Rightarrow \frac{d\rho_i}{dt} = -\frac{\rho_i^2}{p_i}\left[\frac{1}{2}\sum_j m_j\left(\frac{p_j}{\rho_j^2} + \frac{p_i}{\rho_i^2}\right)\mathbf{u}_{ji}\cdot\nabla_{\mathbf{x}_i}\psi_{ij}(\mathbf{x}_i - \mathbf{x}_j)\right]$$

$$= -\frac{1}{2}\frac{\rho_i^2}{p_i}\sum_j m_j\left(\frac{p_j}{\rho_j^2} + \frac{p_i}{\rho_i^2}\right)\mathbf{u}_{ji}\cdot\nabla_{\mathbf{x}_i}\psi_{ij}(\mathbf{x}_i - \mathbf{x}_j). \tag{3.48}$$

As before, the smoothing length is updated using (2.22) and the discretized part

$\nabla \cdot \mathbf{u}$ of (3.48):

$$\begin{aligned}\frac{d\epsilon_i}{dt} &= \frac{\epsilon_i}{n}\nabla \cdot \mathbf{u} \\ &= -\frac{\epsilon_i}{2n}\frac{\rho_i^2}{p_i}\sum_j m_j \left(\frac{p_j}{\rho_j^2}+\frac{p_i}{\rho_i^2}\right)\mathbf{u}_{ji}\cdot\nabla_{\mathbf{x}_i}\psi_{ij}(\mathbf{x}_i-\mathbf{x}_j). \qquad (3.49)\end{aligned}$$

The final equations with the artificial viscosity are

$$\begin{aligned}\frac{d\rho_i}{dt} &= -\frac{1}{2}\frac{\rho_i^2}{p_i}\sum_j m_j \left(\frac{p_j}{\rho_j^2}+\frac{p_i}{\rho_i^2}\right)\mathbf{u}_{ji}\cdot\nabla_{\mathbf{x}_i}\psi_{ij}(\mathbf{x}_i-\mathbf{x}_j), \qquad (3.50)\\ \frac{d\mathbf{u}_i}{dt} &= -\sum_j m_j \left(\frac{p_j}{\rho_j^2}+\frac{p_i}{\rho_i^2}+\frac{\Pi_{ij}}{\bar{\rho}_{ij}^2}\right)\nabla_{\mathbf{x}_i}\psi_{ij}(\mathbf{x}_i-\mathbf{x}_j), \qquad (3.51)\\ \frac{de_i}{dt} &= -\frac{1}{2}\sum_j m_j \left(\frac{p_j}{\rho_j^2}+\frac{p_i}{\rho_i^2}+\frac{\Pi_{ij}}{\bar{\rho}_{ij}^2}\right)\mathbf{u}_{ji}\cdot\nabla_{\mathbf{x}_i}\psi_{ij}(\mathbf{x}_i-\mathbf{x}_j), \qquad (3.52)\\ \frac{d\epsilon_i}{dt} &= -\frac{\epsilon_i}{2n}\frac{\rho_i^2}{p_i}\sum_j m_j \left(\frac{p_j}{\rho_j^2}+\frac{p_i}{\rho_i^2}\right)\mathbf{u}_{ji}\cdot\nabla_{\mathbf{x}_i}\psi_{ij}(\mathbf{x}_i-\mathbf{x}_j), \qquad (3.53)\\ \frac{d\mathbf{x}_i}{dt} &= \mathbf{u}_i. \qquad (3.54)\end{aligned}$$

Note that the artificial viscosity (3.18) is divided by $\bar{\rho}_{ij}^2$ since Π_{ij} has the dimension of stress or pressure; moreover, Π_{ij} can be added to the pressures instead. Π_{ij} is inserted as in (3.51) and (3.52) to obtain less cluttered equations.

Since local mass conservation is an intrinsic property of the particle formulation (because $m_i = \omega_i(t)\rho_i(t)$), density can be updated using

$$\rho_i(t) = \sum_j \rho_j(t)\psi_{\epsilon_i}(\mathbf{x}_i-\mathbf{x}_j)\omega_j = \sum_j m_j\psi_{\epsilon_i}(\mathbf{x}_i-\mathbf{x}_j), \qquad (3.55)$$

instead of using (3.12).

However, the use of (3.55) has some disadvantages. One of the disadvantages is that the density of particles is determined by the spatial distribution of particles; thus, as shown in Figure 2.4, depending on ϵ/h, the density will be slightly more or less than the expected density, unless the density summation is modified to satisfy zeroth order consistency. Another problem is that the use of (3.55) smooths the density near interfaces where density varies sharply. For example, as Diagram 3.3 depicts, the expected sharp density variation γ_E across the interface is smoothed to γ_S due to the gradual decrease in the number of neighbours as particles get closer to the interface, e.g. observe the decrease in the number of neighbours for particles n, l, k.

There are also computational disadvantages of using (3.55). One computational disadvantage is the need to compute ψ_ϵ, in addition to $\nabla\psi_\epsilon$. Moreover, the density must be updated after updating the positions, thus needing to loop over the particles

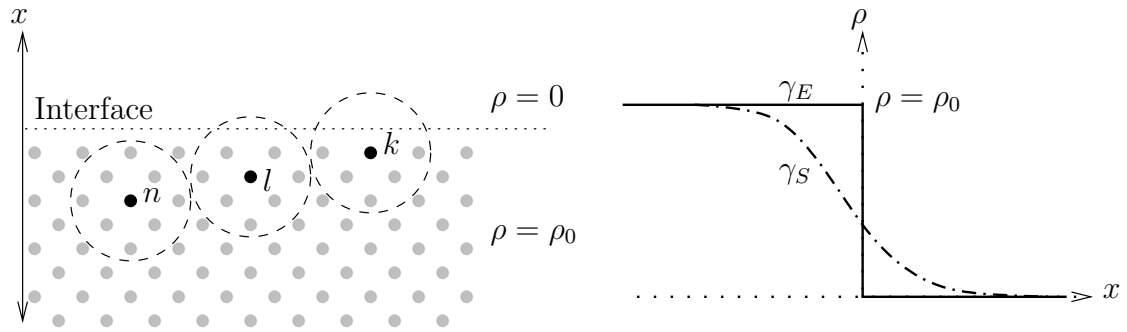

Figure 3.3: Interface

an additional time. For simulations in this thesis, only equations explicitly derived from the continuity equation will be used to evolve density.

3.2.1 Conservation properties

We show here that the time-continuous spatially discretized SPH formulations (3.51) and (3.52) conserve momentum and energy. However, fully discretized equations, i.e. temporally and spatially discretized, may not conserve momentum or energy exactly. For a N-particle system, the conservation of linear momentum, angular momentum, and energy are stated by (3.26), (3.27), and (3.28) respectively.

The properties of the kernel and artificial viscosity that ensure the conservation of momentum and energy are

$$\nabla_{\mathbf{x}_i}\psi_{\epsilon_{ij}}(\mathbf{x}_i-\mathbf{x}_j) = -\nabla_{\mathbf{x}_j}\psi_{\epsilon_{ij}}(\mathbf{x}_j-\mathbf{x}_i), \tag{3.56}$$

$$\nabla_{\mathbf{x}_i}\psi_{\epsilon_{ij}}(\mathbf{x}_i-\mathbf{x}_j) = \frac{\mathbf{x}_i-\mathbf{x}_j}{\|\mathbf{x}_i-\mathbf{x}_j\|}\frac{1}{\epsilon_{ij}}\frac{d}{dr}\psi_{\epsilon_{ij}}(r), \tag{3.57}$$

$$\Pi_{ij} = \Pi_{ji}, \tag{3.58}$$

where $r=\|\mathbf{x}_i-\mathbf{x}_j\|$. Equations (3.51) and (3.58) give

$$\begin{aligned}\frac{d}{dt}\left(\sum_i m_i\mathbf{u}_i\right) &= -\sum_i\sum_j\left(\frac{p_j}{\rho_j^2}+\frac{p_i}{\rho_i^2}+\frac{\Pi_{ij}}{\bar{\rho}_{ij}^2}\right)\nabla_{\mathbf{x}_i}\psi_{\epsilon_{ij}}(\mathbf{x}_i-\mathbf{x}_j)m_im_j\\ &= -\frac{1}{2}\sum_i\sum_j\left(\frac{p_j}{\rho_j^2}+\frac{p_i}{\rho_i^2}+\frac{\Pi_{ij}}{\bar{\rho}_{ij}^2}\right)\nabla_{\mathbf{x}_i}\psi_{\epsilon_{ij}}(\mathbf{x}_i-\mathbf{x}_j)m_im_j\\ &\quad -\frac{1}{2}\sum_j\sum_i\left(\frac{p_i}{\rho_i^2}+\frac{p_j}{\rho_j^2}+\frac{\Pi_{ij}}{\bar{\rho}_{ij}^2}\right)\nabla_{\mathbf{x}_i}\psi_{\epsilon_{ji}}(\mathbf{x}_j-\mathbf{x}_i)m_jm_i\\ &= 0,\end{aligned} \tag{3.59}$$

where (3.56) is used for the last step. Angular momentum is conserved by (3.56)-

(3.58):

$$\begin{aligned}
\frac{d}{dt}\left(\sum_i m_i \mathbf{x}_i \times \mathbf{u}_i\right) &= \sum_i m_i \left(\mathbf{x}_i \times \frac{d\mathbf{u}_i}{dt} + \frac{d\mathbf{x}_i}{dt} \times \mathbf{u}_i\right) \\
&= \sum_i \sum_j \left(\frac{p_j}{\rho_j^2} + \frac{p_i}{\rho_i^2} + \frac{\Pi_{ij}}{\bar{\rho}_{ij}^2}\right) \mathbf{x}_i \times \nabla_{\mathbf{x}_i} \psi_{\epsilon_{ij}}(\mathbf{x}_i - \mathbf{x}_j) m_i m_j \\
&= \frac{1}{2} \sum_i \sum_j \left(\frac{p_j}{\rho_j^2} + \frac{p_i}{\rho_i^2} + \frac{\Pi_{ij}}{\bar{\rho}_{ij}^2}\right) (\mathbf{x}_i - \mathbf{x}_j) \times \nabla_{\mathbf{x}_i} \psi_{\epsilon_{ij}}(\mathbf{x}_i - \mathbf{x}_j) m_i m_j \\
&= 0. \qquad (3.60)
\end{aligned}$$

Conservation of total energy can be shown by using the same argument used to show the conservation of linear momentum:

$$\begin{aligned}
\frac{d}{dt}\left(\sum_i m_i E_i\right) &= \sum_i m_i \frac{de_i}{dt} + \sum_j m_i \mathbf{u}_i \cdot \frac{d\mathbf{u}_i}{dt} \\
&= \frac{1}{2} \sum_i \sum_j \left(\frac{p_j}{\rho_j^2} + \frac{p_i}{\rho_i^2} + \frac{\Pi_{ij}}{\bar{\rho}_{ij}^2}\right) (\mathbf{u}_i + \mathbf{u}_j) \nabla_{\mathbf{x}_i} \psi_{\epsilon_{ij}}(\mathbf{x}_i - \mathbf{x}_j) m_i m_j, \qquad (3.61)
\end{aligned}$$

where (3.51) and (3.52) are used for $d\mathbf{u}_i/dt$ and de_i/dt.

3.2.2 Entropy

Following the same line of argument as in Section 3.1.3, using (3.36), (3.50), and (3.52), we get

$$\begin{aligned}
\frac{dQ_i}{dt} &= \frac{de_i}{dt} - \frac{p_i}{\rho_i^2} \frac{d\rho_i}{dt} \\
&= \frac{1}{2} \sum_j \frac{m_j}{\bar{\rho}_{ij}^2} \Pi_{ij} (\mathbf{u}_i - \mathbf{u}_j) \cdot \nabla_{\mathbf{x}_i} \psi_{\epsilon_{ij}}(\mathbf{x}_i - \mathbf{x}_j) \\
&= \frac{1}{2} \sum_j \frac{m_j}{\bar{\rho}_{ij}^2} \Pi_{ij} (\mathbf{u}_i - \mathbf{u}_j) \cdot \frac{\mathbf{x}_i - \mathbf{x}_j}{\|\mathbf{x}_i - \mathbf{x}_j\|} \frac{1}{\epsilon_{ij}} \frac{d}{dr} \psi_{\epsilon_{ij}}(r) \\
&\geq 0. \qquad (3.62)
\end{aligned}$$

3.3 Weak Formulation

3.3.1 Derivation

In Section 3.2, SPH formulation was derived directly from Euler equations. Thus, velocity and pressure must be at least once differentiable. To relax this regularity requirement, we formulate the weak form. Consider Euler equations in the

conservation form:

$$\frac{\partial \rho}{\partial t} + \nabla \cdot (\rho \mathbf{u}) = 0, \tag{3.63}$$

$$\frac{\partial (\rho \mathbf{u})}{\partial t} + \nabla \cdot (\rho \mathbf{u} \otimes \mathbf{u}) + \nabla p = 0, \tag{3.64}$$

$$\frac{\partial E}{\partial t} + \nabla \cdot (\mathbf{u}(E+p)) = 0, \tag{3.65}$$

where $E = \rho\left(e + \frac{1}{2}\mathbf{u}^2\right)$ is the total energy. In 2D, (3.63)-(3.65) can be written in the general form

$$L_{\mathbf{u}}(\mathbf{\Phi}) + \nabla \cdot \mathbf{F}(\mathbf{\Phi}, \mathbf{x}, t) = \mathbf{S}(\mathbf{\Phi}, \mathbf{x}, t), \tag{3.66}$$

where $L_{\mathbf{u}}(\Phi) = \frac{\partial \Phi}{\partial t} + \nabla \cdot (\mathbf{u}\Phi)$ is the transport operator, $\mathbf{S} = \mathbf{0}$,

$$\mathbf{\Phi} = \begin{bmatrix} \rho \\ \rho u \\ \rho v \\ E \end{bmatrix}, \quad \mathbf{F}_1 = \begin{bmatrix} 0 \\ p \\ 0 \\ up \end{bmatrix}, \quad \mathbf{F}_2 = \begin{bmatrix} 0 \\ 0 \\ p \\ vp \end{bmatrix}, \tag{3.67}$$

where $\mathbf{u} = (u, v)$ and $\mathbf{F} = (\mathbf{F}_1, \mathbf{F}_2)$.

Now we will derive the weak formulation for (3.66). Let the test functions $\phi(\mathbf{x}, t) \in C_0^2(\mathbb{R}^n,]0, T[)$, for some $T > 0$. We look for a weak solution $\Phi(\mathbf{x}, t)$ of the PDE (3.66), i.e. we look for a solution that satisfies the condition

$$\int_{\mathbb{R}^n \times]0,T[} \left(L_{\mathbf{u}}(\Phi) + \nabla \cdot \mathbf{F}(\Phi, x, t) - S(\Phi, x, t)\right) \phi(x, t) d\mathbf{x} dt = 0, \tag{3.68}$$

for all $\phi(\mathbf{x}, t) \in C_0^2(\mathbb{R}^n,]0, T[)$. Using $\phi(\mathbf{x}, t) \in C_0^2(\mathbb{R}^n,]0, T[)$ and integrating by parts, we get

$$\int_{\mathbb{R}^n \times]0,T[} \left(\Phi \frac{d\phi}{dt} + \mathbf{F} \cdot \nabla \phi - S\phi\right) dx dt = 0. \tag{3.69}$$

Applying (2.1) and integrating by parts, we get

$$\sum_i \int_{]0,T[} \left[\frac{d}{dt}(\Phi_i \omega_i)\phi_i - \underbrace{\mathbf{F}_i \cdot \nabla \phi_i \omega_i}_{*} - S_i \phi_i \omega_i\right] dt = 0, \tag{3.70}$$

where $\omega_i = \omega_i(t), \mathbf{x}_i = \mathbf{x}_i(t), \phi_i = \phi(\mathbf{x}_i, t), \Phi_i = \Phi(\mathbf{x}_i, t), \mathbf{F}_i = \mathbf{F}(\Phi_i, \mathbf{x}_i, t)$, and $S_i = S(\Phi_i, \mathbf{x}_i, t)$. For the part with label *, putting the SPH approximation (2.15) for $\nabla \phi_i$ and interchanging the indexes, we get

$$\sum_i \int_{]0,T[} \left[\frac{d}{dt}(\Phi_i \omega_i) + \sum_j (\mathbf{F}_i + \mathbf{F}_j) \cdot \nabla_{\mathbf{x}_j} \psi_\epsilon(\mathbf{x}_i - \mathbf{x}_j) \omega_j \omega_i - S_i \omega_i\right] \phi_i(t) dt = 0.$$

(3.71)

Since (3.71) must hold for all $\phi(\mathbf{x},t) \in C_0^2(\mathbb{R}^n,]0,T[)$, it follows that

$$\frac{d}{dt}(\Phi_i\omega_i) + \sum_j (\mathbf{F}_i + \mathbf{F}_j)\cdot\nabla_{\mathbf{x}_j}\psi_\epsilon(\mathbf{x}_i - \mathbf{x}_j)\phi_j\omega_j\omega_i - S_i\omega_i = 0. \tag{3.72}$$

See Appendix C for a detailed derivation. Using (3.66) and (3.72), SPH evolution equations for (3.63)-(3.65) can be written as

$$\frac{d}{dt}(\rho_i\omega_i) = 0, \tag{3.73}$$

$$\frac{d\mathbf{u}_i}{dt} + \sum_j \frac{m_j}{\rho_i\rho_j}(p_j + p_i)\nabla_{\mathbf{x}_j}\psi_\epsilon(\mathbf{x}_i - \mathbf{x}_j) = 0, \tag{3.74}$$

$$\frac{de_i}{dt} + \sum_j \frac{m_j p_j}{\rho_i\rho_j}(\mathbf{u}_j - \mathbf{u}_i)\cdot\nabla_{\mathbf{x}_j}\psi_\epsilon(\mathbf{x}_i - \mathbf{x}_j) = 0, \tag{3.75}$$

where $e_i = e(\mathbf{x}_i(t),t)$ is the internal energy of the particle i. As before, the continuity equation is derived so that the entropy condition holds. Following the same procedure for deriving (3.48),

$$\frac{d\rho}{dt} = -\rho\nabla\cdot\mathbf{u} = -\frac{\rho^2}{p}\left(\frac{p}{\rho}\nabla\cdot\mathbf{u}\right). \tag{3.76}$$

$$\begin{aligned}\Rightarrow \frac{d\rho_i}{dt} &= \frac{\rho_i^2}{p_i}\left[\sum_j \frac{m_j p_j}{\rho_i\rho_j}(\mathbf{u}_j - \mathbf{u}_i)\cdot\nabla_{\mathbf{x}_j}\psi_{\epsilon_{ij}}(\mathbf{x}_i - \mathbf{x}_j)\right] \\ &= \sum_j \frac{m_j\rho_i p_j}{\rho_j p_i}(\mathbf{u}_j - \mathbf{u}_i)\cdot\nabla_{\mathbf{x}_j}\psi_{\epsilon_{ij}}(\mathbf{x}_i - \mathbf{x}_j).\end{aligned} \tag{3.77}$$

As given in Section 2.3.2, the equation for evolving the smoothing length is

$$\frac{d\epsilon_i}{dt} = -\frac{\epsilon_i}{n\rho_i}\frac{d\rho_i}{dt} = \frac{\epsilon_i}{n}\nabla\cdot\mathbf{u}, \tag{3.78}$$

which is discretized using any method, e.g. using the discretized part $\nabla\cdot\mathbf{u}$ of (3.77). Adding the Von Neumann-Richtmyer numerical diffusivity (3.18) to (3.74) and (3.75), the complete set of equations obtained for the weak SPH formulation is given by

$$\frac{d\rho_i}{dt} = \sum_j \frac{m_j\rho_i p_j}{\rho_j p_i}(\mathbf{u}_j - \mathbf{u}_i)\cdot\nabla_{\mathbf{x}_i}\psi_{\epsilon_{ij}}(\mathbf{x}_i - \mathbf{x}_j), \tag{3.79}$$

$$\frac{d\mathbf{u}_i}{dt} = -\sum_j \frac{m_j}{\rho_i\rho_j}(p_j + p_i + \Pi_{ij})\nabla_{\mathbf{x}_i}\psi_{\epsilon_{ij}}(\mathbf{x}_i - \mathbf{x}_j), \tag{3.80}$$

$$\frac{de_i}{dt} = -\sum_j \frac{m_j}{\rho_i\rho_j}\left(p_j + \frac{1}{2}\Pi_{ij}\right)(\mathbf{u}_j - \mathbf{u}_i)\cdot\nabla_{\mathbf{x}_i}\psi_{\epsilon_{ij}}(\mathbf{x}_i - \mathbf{x}_j), \tag{3.81}$$

$$\frac{d\epsilon_i}{dt} = -\frac{\epsilon_i}{n}\sum_j \frac{m_j p_j}{\rho_j p_i}(\mathbf{u}_j - \mathbf{u}_i)\cdot\nabla_{\mathbf{x}_i}\psi_{\epsilon_{ij}}(\mathbf{x}_i - \mathbf{x}_j), \tag{3.82}$$

$$\frac{d\mathbf{x}_i}{dt} = \mathbf{u}_i. \tag{3.83}$$

NOTE: The SPH equations derived in Section 3.2 can be derived using the weak form.

3.3.2 Conservation properties and entropy

Following the same procedure as in Section 3.2.1, (3.80) and (3.81) can be shown to conserve linear momentum, angular momentum, and total energy. Furthermore, (3.79) was derived so as to satisfy the entropy condition.

3.4 Time stepping

Explicit time stepping schemes are used in SPH. For simulations in this thesis, a two-step Runge-Kutta method is used. The following is a brief explanation of the Runge-Kutta method used. In all SPH formulations described in the previous sections, the governing equations take the form

$$\frac{d\mathbf{\Phi}_i}{dt} = \mathbf{F}_i, \tag{3.84}$$

where $\mathbf{\Phi}_i = (\mathbf{u}_i, e_i, \epsilon_i, \mathbf{r}_i)$ and $\mathbf{F}_i = \left(\mathbf{F}_i^{(1)}, F_i^{(2)}, F_i^{(3)}, \mathbf{F}_i^{(4)}\right)$ are the summations from the particles; $\mathbf{u}_i, e_i, \epsilon_i, \mathbf{r}_i$ is the velocity, internal energy, smoothing length, and position respectively. The sequence of updates to $\mathbf{\Phi}_i$ is

$$\mathbf{\Phi}_i^* = \mathbf{\Phi}_i^n + 0.5\Delta t\mathbf{F}_i^n, \tag{3.85}$$

$$\mathbf{\Phi}_i^{**} = \mathbf{\Phi}_i^n + 0.5\Delta t\mathbf{F}_i^*, \tag{3.86}$$

$$\mathbf{\Phi}_i^{n+1} = 2\mathbf{\Phi}_i^{**} - \mathbf{\Phi}_i^n. \tag{3.87}$$

Since an explicit time-stepping scheme is used, the time step Δt must be restricted. If variable time stepping is used, the time step Δt can be chosen as [18]

$$\Delta t_c = \min_i \frac{\epsilon_i}{c_i + \max_j \left\| \frac{\epsilon_i \mathbf{u}_{ij}\cdot\mathbf{x}_{ij}}{\mathbf{x}_{ij}\cdot\mathbf{x}_{ij}} \right\|}, \tag{3.88}$$

$$\Delta t_F = \min_a \sqrt{\frac{\epsilon_i}{\left\|\mathbf{F}_i^{(1)}\right\|}}, \tag{3.89}$$

$$\Delta t = 0.3\min(\Delta t_c, \Delta t_F), \tag{3.90}$$

where c_i is the speed of sound of particle i, $\mathbf{x}_{ij} = \mathbf{x}_i - \mathbf{x}_j$, and $\mathbf{u}_{ij} = \mathbf{u}_i - \mathbf{u}_j$.

The time-discretization (3.85)-(3.87) does not conserve momentum or energy exactly. In general, most standard numerical schemes for solving ODEs does not conserve momentum or energy exactly. A modified Runge-Kutta [6] method that ensures exact momentum conservation is given in (3.91) and (3.92). Let

$$\frac{d\mathbf{\Phi}_i}{dt} = \mathbf{F}_i \quad \text{and} \quad \frac{d\mathbf{x}_i}{dt} = \mathbf{U}_i, \tag{3.91}$$

where $\mathbf{\Phi}_i = (\mathbf{u}_i, e_i, \epsilon_i)$. The updates are performed as follows:

$$\begin{array}{ll} \mathbf{\Phi}_i^* = \mathbf{\Phi}_i^n + \Delta t \mathbf{F}_i^n, & \mathbf{x}_i^* = \mathbf{x}_i^n + \Delta t \mathbf{U}_i^n, \\ \mathbf{\Phi}_i^{n+1/2} = \frac{1}{2}(\mathbf{\Phi}_i^* + \mathbf{\Phi}_i^n), & \mathbf{x}_i^{n+1/2} = \frac{1}{2}(\mathbf{x}_i^* + \mathbf{x}_i^n), \\ \mathbf{\Phi}_i^{n+1} = \mathbf{\Phi}_i^n + \Delta t \mathbf{F}_i^{n+1/2}, & \mathbf{x}_i^{n+1} = \mathbf{x}_i^n + \frac{1}{2}\Delta t(\mathbf{U}_i^* + \mathbf{U}_i^n). \end{array} \tag{3.92}$$

Chapter 4

Improvements to SP Approximations

One of the problems in SP approximation is the lack of consistency, e.g., in 1D, SP approximation cannot exactly reproduce the polynomials $1, x, x^2, ...$ However, the zeroth order consistency is satisfied by (2.15). Section 4.1 explains one method used to enforce linear consistency. In Appendix D, another method used to enforce linear *and higher* order consistency is discussed.

4.1 Renormalized Meshfree Derivatives (RMD)

Equation (2.15) ensures $D^{\epsilon}_{\alpha,h} f = 0$ for any function $f \in \mathbb{P}^0(\mathbb{R}^n)$, the constant functions in $\mathbb{R}^n$; however, as shown in Figure 2.4, the accuracy of $D^{\epsilon}_{\alpha,h} x$ varies depending on the ratio ϵ/h. It follows that $D^{\epsilon}_{\alpha,h} f$ also depends on ϵ/h for any $f \in \mathbb{P}^1(\mathbb{R}^n)$, the linear functions in $\mathbb{R}^n$. RMD [4] is a method to modify the operator $D^{\epsilon}_{\alpha,h}$ so that $D^{\epsilon}_{\alpha,h} f = \textit{constant}$ for any $f \in \mathbb{P}^1(\mathbb{R}^n)$ irrespective of the ratio ϵ/h, so long as there are enough neighbouring particles. For clarity, let us first consider RMD in 1D and 2D. In 1D, linear consistency is easily enforced by modifying $D^{\epsilon}_{\alpha,h}$ with the introduction of a function $c(x)$ such that

$$D^{\epsilon}_{x,h} x = \sum_j c(x)(x_j - x) \frac{\partial \psi_\epsilon}{\partial x}(x - x_j)\omega_j = 1. \tag{4.1}$$

Similarly in 2D, the modification of $D^{\epsilon}_{\alpha,h}$ to satisfy the four conditions

$$D^{\epsilon}_{x,h} x = 1, \quad D^{\epsilon}_{x,h} y = 0, \quad D^{\epsilon}_{y,h} x = 0, \quad D^{\epsilon}_{y,h} y = 1 \tag{4.2}$$

require four functions, say $b_{11}(\mathbf{x}), b_{12}(\mathbf{x}), b_{21}(\mathbf{x}), b_{22}(\mathbf{x})$. For any function f, the coefficients $b_{11}(\mathbf{x}), b_{12}(\mathbf{x}), b_{21}(\mathbf{x}), b_{22}(\mathbf{x})$ are added as follows:

$$\nabla_h f(\mathbf{x}) = \sum_j \omega_j \left[f(\mathbf{x}_j) - f(\mathbf{x})\right] \begin{pmatrix} b_{11}(\mathbf{x}) & b_{12}(\mathbf{x}) \\ b_{21}(\mathbf{x}) & b_{22}(\mathbf{x}) \end{pmatrix} \nabla \psi_{\epsilon_{ij}}(\mathbf{x} - \mathbf{x}_j). \tag{4.3}$$

The functions are found by solving the equations

$$D^{\epsilon}_{x,h} x = \sum_j (x_j - x) \left[b_{11}(\mathbf{x}) \frac{\partial \psi_\epsilon}{\partial x}(\mathbf{x} - \mathbf{x}_j) + b_{12}(\mathbf{x}) \frac{\partial \psi_\epsilon}{\partial y}(\mathbf{x} - \mathbf{x}_j) \right] \omega_j = 1, \tag{4.4}$$

$$D^{\epsilon}_{x,h} y = \sum_j (y_j - y) \left[b_{11}(\mathbf{x}) \frac{\partial \psi_\epsilon}{\partial x}(\mathbf{x} - \mathbf{x}_j) + b_{12}(\mathbf{x}) \frac{\partial \psi_\epsilon}{\partial y}(\mathbf{x} - \mathbf{x}_j) \right] \omega_j = 0, \tag{4.5}$$

$$D^{\epsilon}_{y,h} x = \sum_j (x_j - x) \left[b_{11}(\mathbf{x}) \frac{\partial \psi_\epsilon}{\partial x}(\mathbf{x} - \mathbf{x}_j) + b_{12}(\mathbf{x}) \frac{\partial \psi_\epsilon}{\partial y}(\mathbf{x} - \mathbf{x}_j) \right] \omega_j = 0, \tag{4.6}$$

$$D^{\epsilon}_{y,h} y = \sum_j (y_j - y) \left[b_{11}(\mathbf{x}) \frac{\partial \psi_\epsilon}{\partial x}(\mathbf{x} - \mathbf{x}_j) + b_{12}(\mathbf{x}) \frac{\partial \psi_\epsilon}{\partial y}(\mathbf{x} - \mathbf{x}_j) \right] \omega_j = 1, \tag{4.7}$$

giving

$$\begin{aligned} B(\mathbf{x}) &= \begin{bmatrix} b_{11}(\mathbf{x}) & b_{11}(\mathbf{x}) \\ b_{21}(\mathbf{x}) & b_{22}(\mathbf{x}) \end{bmatrix} \\ &= \begin{bmatrix} \sum_j (x_j - x) \frac{\partial \psi_\epsilon}{\partial x}(\mathbf{x} - \mathbf{x}_j) \omega_j & \sum_j (y_j - y) \frac{\partial \psi_\epsilon}{\partial x}(\mathbf{x} - \mathbf{x}_j) \omega_j \\ \sum_j (x_j - x) \frac{\partial \psi_\epsilon}{\partial y}(\mathbf{x} - \mathbf{x}_j) \omega_j & \sum_j (y_j - y) \frac{\partial \psi_\epsilon}{\partial y}(\mathbf{x} - \mathbf{x}_j) \omega_j \end{bmatrix}^{-1}, \end{aligned} \tag{4.8}$$

where $\mathbf{x} - \mathbf{x}_j = (x - x_j, y - y_j)$. The same methodology extends to 3D.

RMD for any dimension n, and a result pertaining to the error bound is described as follows. Generalize (2.15) by replacing the kernel $D_\alpha \psi_\epsilon(\mathbf{x}_i - \mathbf{x}_j)$ by $\sum_{\beta=1}^n B_i^{\alpha\beta} \mu_{ij}^\beta$, where $\mu_{ij}^\beta = D_\beta \psi_\epsilon(\mathbf{x}_i - \mathbf{x}_j)$ and $B_i^{\alpha\beta}$ is a $n \times n$ matrix whose coefficients are to be determined. The gradient operator then takes the form

$$D_{\alpha,h} f_i = \sum_j \omega_j \left(f_j - f_i\right) A_{ij}^\alpha, \tag{4.9}$$

where $A_{ij}^\alpha = \sum_{\beta=1}^n B_i^{\alpha\beta} \mu_{ij}^\beta$ and $f_i = f(x_i)$. The matrix B_i is computed to satisfy the condition

$$D_{\alpha,h} f = D_\alpha f, \text{ for all } f \in \mathbb{P}^1(\mathbb{R}^n) \text{ and } \alpha \in \{1, 2, 3, ..., n\}. \tag{4.10}$$

It can be shown that (4.10) is satisfied if $B_i = B(x_i)$ is computed as $B_i = (E_i)^{-1}$, where

$$E_i^{\alpha\beta} = \sum_j \omega_j \left(x_j^\beta - x_i^\beta\right) \mu_{ij}^\alpha, \text{ for all } (\alpha, \beta) \in \{1, 2, 3, ..., n\}^2, \tag{4.11}$$

which is given by (4.8) in 2D. To obtain error bounds for RMD, the following conditions are assumed: there exists two constants $C, D \in \mathbb{R}$ such that

$$\epsilon_0 \leq \epsilon \leq C\epsilon_0, \tag{4.12}$$

$$\|\mu(\mathbf{x}, \mathbf{y})\| \leq \frac{D}{\epsilon_0^{d+1}}, \tag{4.13}$$

$$\mu(\mathbf{x}, \mathbf{y}) = 0 \text{ for } \|\mathbf{x} - \mathbf{y}\| \geq \epsilon(\mathbf{x}, \mathbf{y}), \tag{4.14}$$

for every $\mathbf{x}, \mathbf{y} \in \mathbb{R}^n$. Note that (4.12) holds if $\mathbf{u} \in C^2(\mathbb{R}^n, [0, T])^n$.

The result on the error bound and the proof is given in [4]. Suppose the matrix $E(\mathbf{x})$ defined in (4.11) is invertible for all $\mathbf{x}$, and that (4.12)-(4.14) hold. Then there exists $C > 0$ such that for all $\phi \in W^{2,\infty}(\mathbb{R}^n)$, the RMD (4.9) computed with (4.11) satisfy

$$\|D_h\phi(\mathbf{x}) - D\phi(\mathbf{x})\| \leq C\epsilon_0\|B(\mathbf{x})\|\|D^2\phi\|_\infty, \tag{4.15}$$

where D^2 denotes the matrix of the second order derivative of ϕ. To ensure local conservation,

$$B_{ij} = \frac{B_i + B_j}{2} \tag{4.16}$$

is chosen in place of B_i in (4.9) [4]. With this choice, under the assumptions (4.12)-(4.14), and the added assumption

$$\|\mathbf{x}_i - \mathbf{x}_j\| \leq C\epsilon \Rightarrow B_j = B_i + O(\epsilon), \tag{4.17}$$

for all i, j, the the error bound for the approximation becomes

$$\|D_h\phi(\mathbf{x}) - D\phi(\mathbf{x})\| \leq C\epsilon_0\|B(\mathbf{x})\| \left(\|D^2\phi\|_\infty + \|D\phi\|_\infty\right). \tag{4.18}$$

For an initial distribution of particles regular enough, (4.17) is satisfied as proved in Reference [4] under the assumption $\mathbf{u} \in C^2$.

With the application of RMD to (3.79)-(3.83), the set of equations obtained is

$$\frac{d\rho_i}{dt} = \sum_j \frac{m_j\rho_i p_j}{\rho_j p_i}(\mathbf{u}_j - \mathbf{u}_i) \cdot B_{ij}\nabla_{\mathbf{x}_i}\psi_{\epsilon_{ij}}(\mathbf{x}_i - \mathbf{x}_j), \tag{4.19}$$

$$\frac{d\mathbf{u}_i}{dt} = -\sum_j \frac{m_j}{\rho_i\rho_j}(p_j + p_i + \Pi_{ij})B_{ij}\nabla_{\mathbf{x}_i}\psi_{\epsilon_{ij}}(\mathbf{x}_i - \mathbf{x}_j), \tag{4.20}$$

$$\frac{de_i}{dt} = -\sum_j \frac{m_j}{\rho_i\rho_j}\left(p_j + \frac{1}{2}\Pi_{ij}\right)(\mathbf{u}_j - \mathbf{u}_i) \cdot B_{ij}\nabla_{\mathbf{x}_i}\psi_{\epsilon_{ij}}(\mathbf{x}_i - \mathbf{x}_j), \tag{4.21}$$

$$\frac{d\epsilon_i}{dt} = -\frac{\epsilon_i}{n}\sum_j \frac{m_j p_j}{\rho_j p_i}(\mathbf{u}_j - \mathbf{u}_i) \cdot B_{ij}\nabla_{\mathbf{x}_i}\psi_{\epsilon_{ij}}(\mathbf{x}_i - \mathbf{x}_j), \tag{4.22}$$

$$\frac{d\mathbf{x}_i}{dt} = \mathbf{u}_i, \tag{4.23}$$

where B_{ij} is the renormalization matrix (4.16). Note that (3.79)-(3.83) is the same as (4.19)-(4.23) if

$$B_{ij} = \begin{bmatrix} 1 & 0 \\ 0 & 1 \end{bmatrix}. \tag{4.24}$$

4.2 Comparisons of approximations formulae

Figures 4.1-4.3 show the results obtained using SPH given by (3.50)-(3.54), weak SPH (W-SPH) given by (3.79)-(3.83), and weak renormalized SPH (R-SPH) given by (4.19)-(4.23) for the two dimensional shock tube problem with the initial conditions

$$\rho(x,y) = \begin{cases} 2, & \text{for } 0 \le x \le 0.5, \quad 0 \le y \le 1, \\ 1, & \text{for } 0.5 < x \le 1, \quad 0 \le y \le 1, \end{cases} \tag{4.25}$$

$$e(x,y) = 1, \text{ for } 0 \le x \le 1, \quad 0 \le y \le 1, \tag{4.26}$$

$$\mathbf{u}(x,y) = \mathbf{0}, \text{ for } 0 \le x \le 1, \quad 0 \le y \le 1, \tag{4.27}$$

where $\rho, e, \mathbf{u}$ are respectively the density, internal energy, and velocity. The results were computed using 10,000 particles in the interior. The initial particle distribution is shown in Figure 4.4(a) . No-slip-reflective boundary condition is imposed; As shown in Figure 4.4(b), ghost particles are used for creating the boundaries (see Section 6.1). In Figures 4.1-4.3, the "Exact" solution was obtained from a Riemann solver.

Comparing Figures 4.1-4.3, differences in the solutions are more noticeable for higher ratios of initial densities. Considering the 1:2 initial density ratio, Figures 4.1(a)-(c), SPH and W-SPH tend to slightly overestimate or underestimate the plateau regions. The overestimation can be clearly seen in the velocity profile for 1:4 ratio, Figure 4.2(c). For the 1:8 ratio, considering the velocity profile, Figure 4.3(c), the R-SPH performs a lot better compared to SPH and W-SPH.

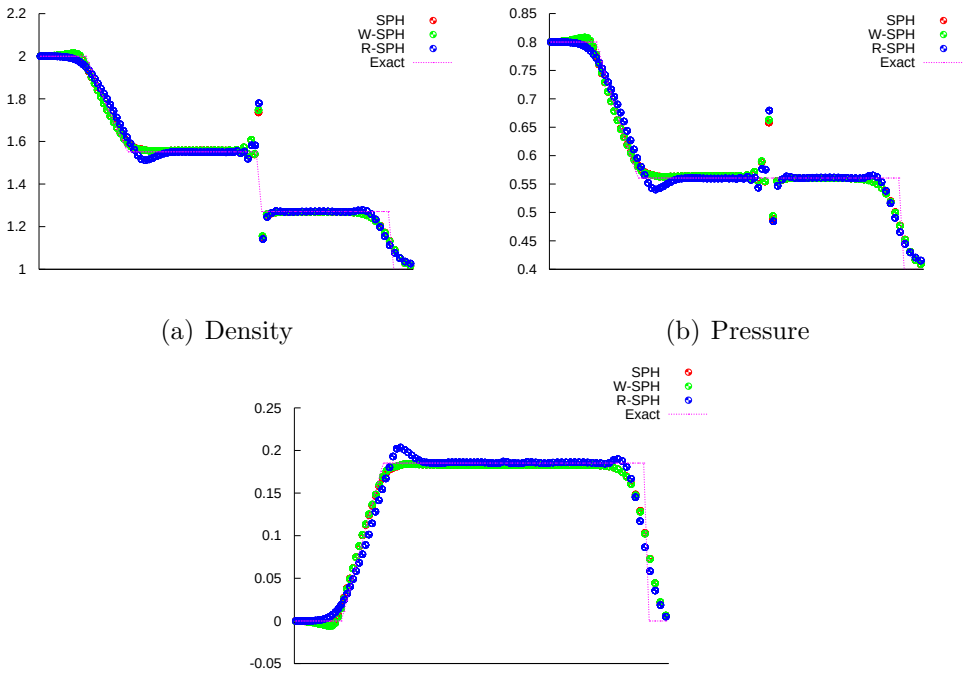

(a) Density

(b) Pressure

(c) Velocity

Figure 4.1: Profiles, Ratio 1:2

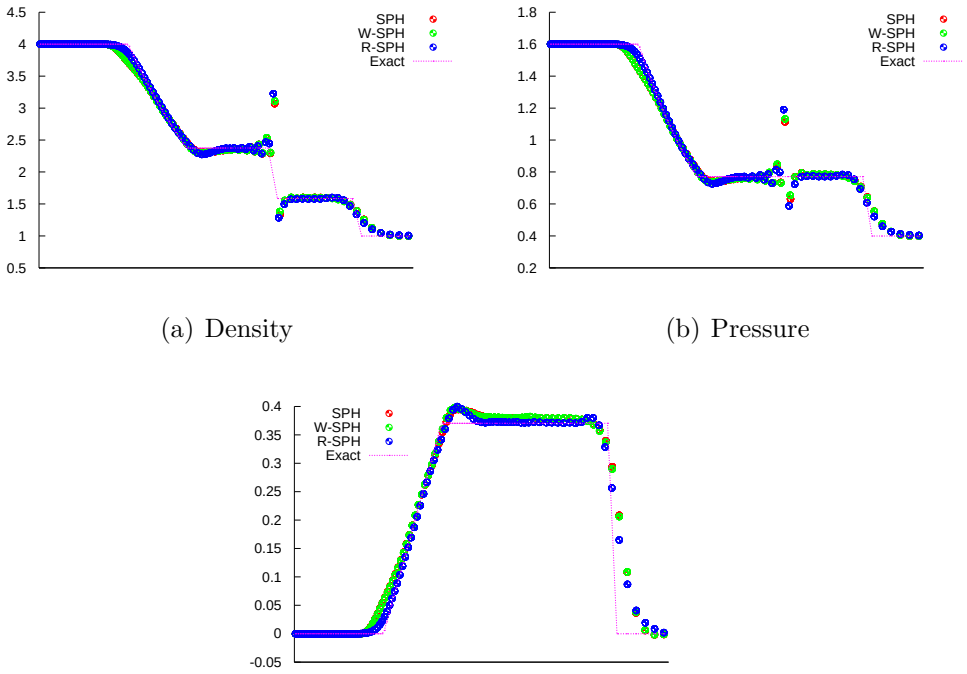

(a) Density

(b) Pressure

(c) Velocity

Figure 4.2: Profiles, Ratio 1:4

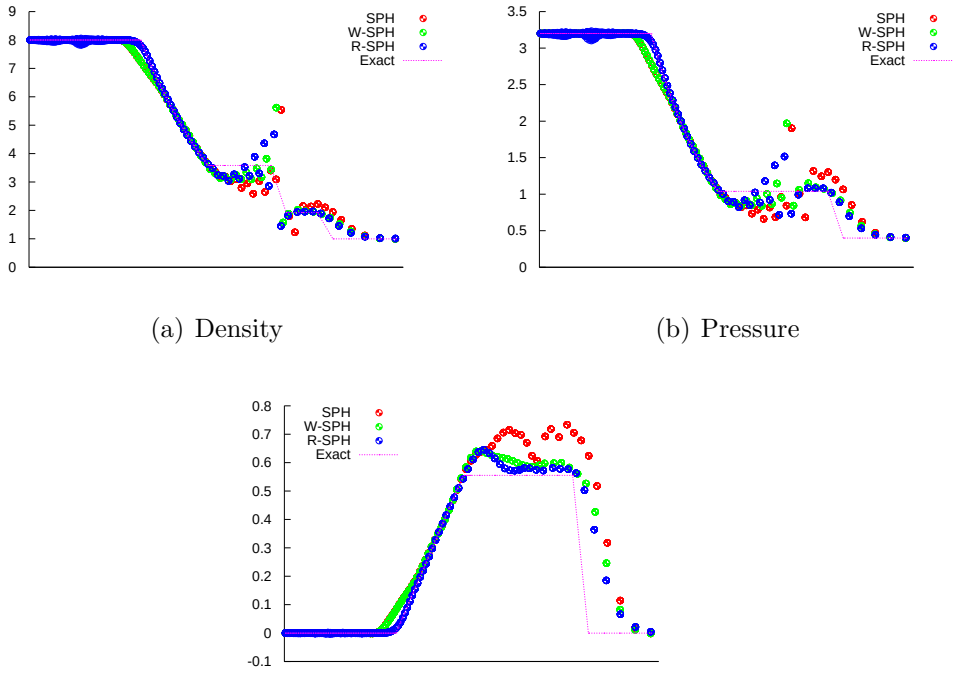

(a) Density

(b) Pressure

(c) Velocity

Figure 4.3: Profiles, Ratio 1:8

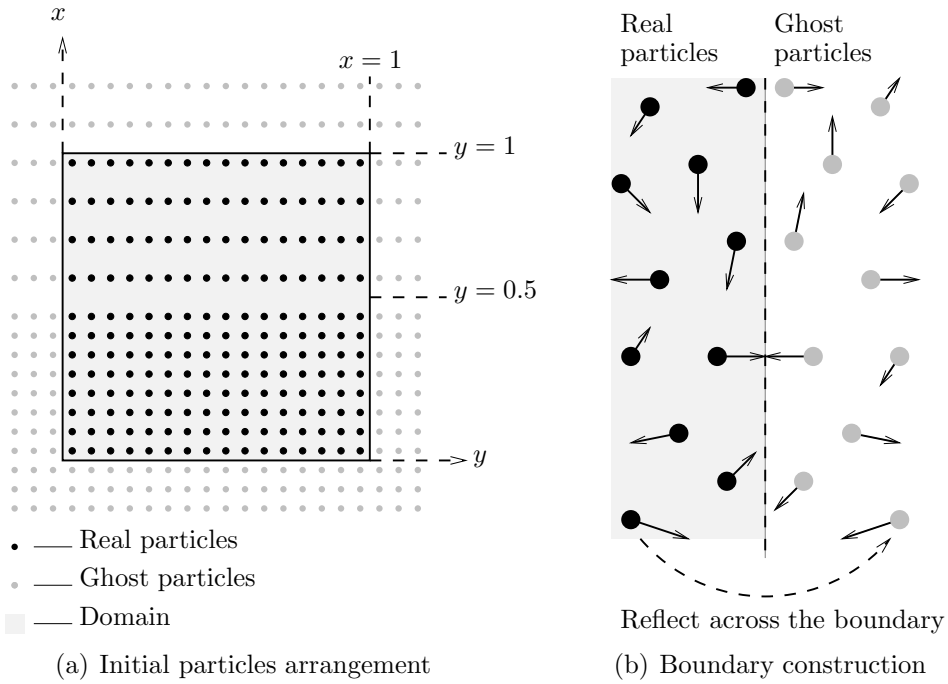

(a) Initial particles arrangement

(b) Boundary construction

Figure 4.4: 2D Shockwave particle arrangements

Chapter 5

Application to Navier-Stokes Equations

In this chapter, Navier-Stokes equations are stated in a very general form for the ease of deriving the weak SPH formulation, especially the energy equation. Then a brief description of LES is given for incompressible, and weakly incompressible fluids. We will be using the weakly incompressible formulation since water will be treated as a weakly incompressible fluid.

5.1 Navier-Stokes equations

Navier-Stokes equations [11] can be written in the conservative form

$$\frac{\partial \rho}{\partial t} + \nabla \cdot (\rho \mathbf{u}) = 0, \tag{5.1}$$

$$\frac{\partial (\rho \mathbf{u})}{\partial t} + \nabla \cdot (\rho \mathbf{u} \otimes \mathbf{u}) + \nabla p - \mu \nabla^2 \mathbf{u} - (\lambda + \mu) \nabla (\nabla \cdot \mathbf{u}) = \mathbf{f}, \tag{5.2}$$

$$\frac{\partial E}{\partial t} - \nabla \cdot (\mathbf{u} \cdot \varsigma) = 0, \tag{5.3}$$

where $E = \rho \left(e + \frac{1}{2} \mathbf{u}^2 \right)$ is the total energy, $\varsigma_{kl} = -p\delta_{kl} + \lambda (\nabla \cdot \mathbf{u}) \delta_{kl} + 2\mu S_{kl}$ is the stress tensor for a Newtonian fluid, $S_{kl} = \frac{1}{2}(\frac{\partial u_k}{\partial x_l} + \frac{\partial u_l}{\partial x_k})$ is the strain rate tensor, and $\mathbf{f}$ is the external force.

SP approximation of the viscous term $\nabla^2 \mathbf{u}$ is the main problem in the application of SP approximation to Navier-Stokes equations. A number of approximation are used for $\nabla^2 \mathbf{u}$ [8]. There are two direct methods to evaluate the viscous term. One method is using double summations:

$$\nabla^2 \mathbf{u}_i = \nabla \cdot \nabla \mathbf{u}_i \approx \nabla \cdot (\nabla \mathbf{u}_i)_h \approx \sum_j (\nabla_h \mathbf{u}_j - \nabla_h \mathbf{u}_i) \cdot \nabla_i \psi_{ij} \omega_j, \tag{5.4}$$

where

$$\nabla_h \mathbf{u}_i = \sum_j (\mathbf{u}_j - \mathbf{u}_i) \nabla_i \psi_{ij} \omega_j \tag{5.5}$$

is the SP approximation of the operator ∇. The other direct method to evaluate the viscous term is to transfer the Laplacian to the kernel function:

$$\nabla^2 \mathbf{u}_i \approx \sum_j (\mathbf{u}_j - \mathbf{u}_i) \nabla_i^2 \psi_{ij} \omega_j. \tag{5.6}$$

But (5.4) and (5.6) are rarely used: (5.4) is computationally expensive, and (5.6) requires higher-order spline kernels for accuracy. The method that is widely used for low Reynolds number flows was put forward by Morris [8] and is given by

$$\nabla^2 \mathbf{u}_i \approx 2 \sum_j \frac{\mathbf{u}_{ij} \mathbf{x}_{ij} \cdot \nabla_i \psi_{ij} \omega_j}{\|\mathbf{x}_{ij}\|^2}. \tag{5.7}$$

Formulation (5.7) combines a FD and SPH approximations (see Appendix A). Despite the high computational cost of using (5.4), in this thesis, (5.4) is used as renormalization can be easily applied to it.

5.2 Weak Formulation

In 2D, (5.1)-(5.3) can be written in the form

$$L_{\mathbf{u}}(\mathbf{\Phi}) + \nabla \cdot \mathbf{F}(\phi, \mathbf{x}, t) = \mathbf{M}(\mathbf{\Phi}, \mathbf{x}, t), \tag{5.8}$$

where

$$\mathbf{\Phi} = \begin{bmatrix} \rho \\ \rho u \\ \rho v \\ E \end{bmatrix}, \quad \mathbf{M} = \begin{bmatrix} 0 \\ f^{(1)} \\ f^{(2)} \\ 0 \end{bmatrix}, \tag{5.9}$$

$$\mathbf{F}_1 = \begin{bmatrix} 0 \\ p - \mu u_x - (\lambda + \mu) \nabla \cdot \mathbf{u} \\ -\mu v_x \\ up - \lambda u \nabla \cdot \mathbf{u} - 2\mu L^{(1)} \end{bmatrix}, \quad \mathbf{F}_2 = \begin{bmatrix} 0 \\ -\mu u_y \\ p - \mu v_y - (\lambda + \mu) \nabla \cdot \mathbf{u} \\ vp - \lambda v \nabla \cdot \mathbf{u} - 2\mu L^{(2)} \end{bmatrix}, \tag{5.10}$$

where the velocity $\mathbf{u} = (u, v)$, $\mathbf{F} = (\mathbf{F}_1, \mathbf{F}_2)$, $L^{(k)} = u_l S_{kl}$, $u_x = \frac{\partial u}{\partial x}$, and $\mathbf{f} = [f^{(1)}, f^{(2)}]$ and vice versa. Using (3.72), the momentum and energy equations can be written as

$$\frac{d\mathbf{u}_i}{dt} = -\sum_j \frac{m_j}{\rho_i \rho_j} (p_j + p_i) \nabla_i \psi_{ij}$$

$$
\begin{aligned}
&+\mu \sum_j \frac{m_j}{\rho_i \rho_j} \nabla_h \left(\mathbf{u}_i + \mathbf{u}_j\right) \cdot \nabla_i \psi_{ij} \\
&+(\lambda + \mu) \sum_j \frac{m_j}{\rho_i \rho_j} \left(\nabla_h \cdot \mathbf{u}_i + \nabla_h \cdot \mathbf{u}_j\right) \nabla_i \psi_{ij} \\
&+\frac{\mathbf{f_i}}{\rho_i} \qquad (5.11)
\end{aligned}
$$

$$
\begin{aligned}
\frac{de_i}{dt} &= \sum_j \frac{p_j m_j}{\rho_i \rho_j} \left(\mathbf{u}_i - \mathbf{u}_j\right) \nabla_i \psi_{ij} \\
&+\lambda \sum_j \frac{m_j}{\rho_i \rho_j} \left(\mathbf{u}_j \nabla_h \cdot \mathbf{u}_j + \mathbf{u}_i \nabla_h \cdot \mathbf{u}_i\right) \cdot \nabla_i \psi_{ij} \\
&-\mu \sum_j \frac{m_j}{\rho_i \rho_j} \left[\mathbf{u}_i \cdot \nabla_h \left(\mathbf{u}_i + \mathbf{u}_j\right) - 2\left(\mathbf{L}_i + \mathbf{L}_j\right)\right] \cdot \nabla_i \psi_{ij} \\
&-(\lambda + \mu) \sum_j \frac{m_j}{\rho_i \rho_j} \left(\nabla_h \cdot \mathbf{u}_i + \nabla_h \cdot \mathbf{u}_j\right) \mathbf{u}_i \cdot \nabla_i \psi_{ij} \qquad (5.12)
\end{aligned}
$$

where $\mathbf{L}_i = \left[L_i^{(1)}, L_i^{(2)}\right]$ and

$$
\nabla_h \mathbf{u}_i = \sum_j \left(\mathbf{u}_i - \mathbf{u}_j\right) \nabla_i \psi_{ij}. \qquad (5.13)
$$

As usual, we take $\lambda + \frac{2}{3}\mu = 0$, the Stokes assumption.

5.3 Large Eddy Simulation (LES)

Consider a physical quantity $u(\mathbf{x}, t)$, like velocity, which has many scales of variation, both spatially and temporally. For simplicity, let us restrict the description to spatial variations. In numerical simulations, due to the relatively large size of spatial discretization when compared to the smallest spatial variations exhibited by real fluids, the numerical scheme cannot account for the variations that are below the spatial discretization size. This inability to capture fine variations results in the inability of the numerical scheme to capture the natural energy cascade from largest scales to the smallest scales, a process which plays an important role in turbulence. LES is a methodology in which the small scale variations, which cannot be resolved by the spatial discretization, is filtered out from the governing equations, and the effects of unresolvable scales are modelled into the filtered governing equations. In LES terminology, scales not resolved by the numerical scheme are called sub-grid scales (SGS). The LES filtering operation is defined by [12]

$$
\bar{u}(\mathbf{x}, t) = \int_{\mathbb{R}^n} u(\mathbf{x} - \mathbf{r}, t) G(\mathbf{r}) d\mathbf{r}, \qquad (5.14)
$$

where the filter function G satisfies

$$
\int_{\mathbb{R}^n} G(\mathbf{r}) d\mathbf{r} = 1. \qquad (5.15)
$$

Some common 1D filter functions together with their transfer functions are given in Table 5.1. The plots of the three filters in physical and Fourier space is shown

Table 5.1: Filters in physical and Fourier space

Name	Filter (Physical Space)	Filter (Fourier Space)
General	$G(x)$	$\hat{G}(k) = \int_{-\infty}^{\infty} e^{ikr} G(x) dx$
Top-hat	$\frac{1}{\Delta} H\left(\frac{1}{2}\Delta - \lvert x\rvert\right)$	$\frac{\sin\left(\frac{1}{2}k\Delta\right)}{\frac{1}{2}k\Delta}$
Gaussian	$\left(\frac{6}{\pi\Delta^2}\right)^{1/2} \exp\left(-\frac{6x^2}{\Delta^2}\right)$	$\exp\left(-\frac{k^2\Delta^2}{24}\right)$
Spectral	$\frac{\sin(\pi x/\Delta)}{\pi x}$	$H\left(\frac{\pi}{\Delta} - \lvert k\rvert\right)$

in Figure 5.3. The top-hat filter does not have a sharp cut off wavenumber. Also, the top-hat filter, which is local in physical space, is non-local in Fourier space; in contrast, the spectral filter, which is local in Fourier space, is non-local in physical space. Often, 1D filters are used to generate 2D filters. Given a 1D filter $G(x)$, the corresponding 2D filter $G(\mathbf{x}) = \Pi_{i=1}^{2} G(x_i)$, where $\mathbf{x} = (x_1, x_2)$.

The three fundamental properties of this filtering operation which enables the easy manipulation of Navier-Stokes equations are

1. Conservation of constants: $\bar{a} = a,$ for any constant a
2. Linearity: $\overline{\phi + \psi} = \bar{\phi} + \bar{\psi},$ for functions ϕ and ψ
3. Commutation with derivation $\overline{\frac{\partial \phi}{\partial s}} = \frac{\partial \bar{\phi}}{\partial s},\ s = \mathbf{x}, t.$

In most applications where simulations are performed in physical space, the top-hat filter is used. For simulations in this thesis, the top-hat filter will be used.

5.4 SPH-LES of incompressible fluids

For simplicity, let us first consider the incorporation of LES to SPH in incompressible fluids [15]. The filtered incompressible Navier-Stokes equations in conservation form are given by

$$\frac{\partial \rho}{\partial t} + \nabla \cdot (\rho \bar{\mathbf{u}}) = 0, \tag{5.16}$$

$$\frac{\partial (\rho \bar{\mathbf{u}})}{\partial t} + \nabla \cdot (\rho \bar{\mathbf{u}} \otimes \bar{\mathbf{u}}) + \nabla \bar{p} - \mu \nabla^2 \bar{\mathbf{u}} - \nabla \cdot \tau = \bar{\mathbf{f}}, \tag{5.17}$$

where $\tau_{kl} = \rho(\overline{u_k u_l} - \bar{u}_k \bar{u}_l)$, and $\bar{\mathbf{u}}$ is velocity filtered with a homogeneous spatial filter. The isotropic residual stress $\tau_{mm}\delta_{kl}/3$ is absorbed in a modified pressure,

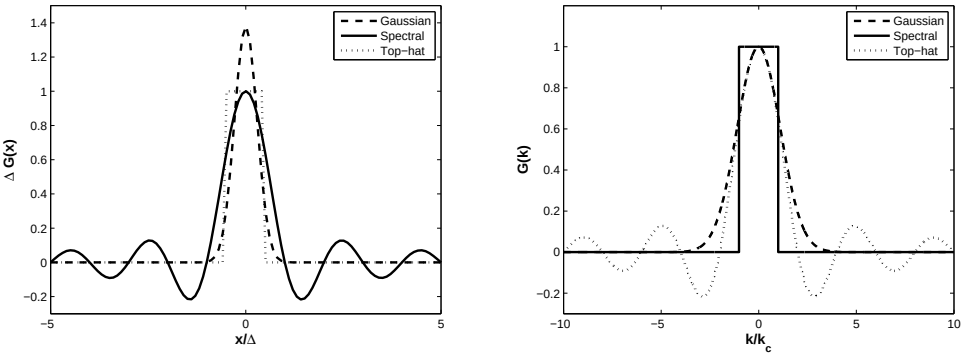

(a) Filters in physical space (b) Filters in Fourier space

Figure 5.1: Plots of filters in physical and wavenumber space

and the anisotropic residual-stress tensor τ_{ij}^r is modelled as

$$\tau_{kl}^r = \tau_{kl} - \frac{1}{3}\tau_{mm}\delta_{kl} = -2\nu_r \bar{S}_{kl}, \tag{5.18}$$

where the eddy viscosity ν_r is modelled as

$$\nu_r = l_s^2 \left|\bar{\mathbf{S}}\right| = (C_s\Delta)^2 \left|\bar{\mathbf{S}}\right|, \tag{5.19}$$

where l_s is the Smagorinsky lengthscale, C_s is the Smagorinsky coefficient, Δ is the filter width, $\bar{S}_{kl} = \frac{1}{2}\left(\frac{\partial \bar{u}_k}{\partial x_l} + \frac{\partial \bar{u}_l}{\partial x_k}\right)$ is the filtered rate of strain tensor, and $\left|\bar{\mathbf{S}}\right| = \sqrt{2\bar{S}_{kl}\bar{S}_{kl}}$. In SPH, the filter-width Δ is taken as the initial inter-particle distance. The resulting discretized SPH momentum equation is

$$\begin{aligned}
\frac{d\bar{\mathbf{u}}_i}{dt} &= -\sum_j \frac{m_j}{\rho_i\rho_j}\left(\bar{p}_i + \bar{p}_j\right)\nabla_i\psi_{ij} \\
&\quad + \sum_j \frac{m_j}{\rho_i\rho_j}\left(\tau_i^r + \tau_j^r\right)\cdot\nabla_i\psi_{ij} \\
&\quad + \mu\sum_j \frac{m_j}{\rho_i\rho_j}\nabla_h\left(\bar{\mathbf{u}}_i + \bar{\mathbf{u}}_j\right)\cdot\nabla_i\psi_{ij} \\
&\quad + \frac{\bar{\mathbf{f}}_i}{\rho_i},
\end{aligned} \tag{5.20}$$

where $\tau_i^r = (\tau_{kl}^r)_i$.

Physically, the effect of the anisotropic residual stress tensor τ_{ij}^r can be explained as follows [12]: denoting the filtered kinetic energy $\bar{E} = \frac{1}{2}\overline{\mathbf{u}\cdot\mathbf{u}}$, the kinetic energy of the filtered velocity $E_f = \frac{1}{2}\bar{\mathbf{u}}\cdot\bar{\mathbf{u}}$, and $\bar{E} = E_f + k_r$, where the residual kinetic energy $k_r = \frac{1}{2}\overline{\mathbf{u}\cdot\mathbf{u}} - \frac{1}{2}\bar{\mathbf{u}}\cdot\bar{\mathbf{u}} = \frac{1}{2}\tau_{mm}$, the conservation equation for E_f can be written

as

$$\frac{dE_f}{dt} - \frac{\partial}{\partial x_k}\left[\bar{u}_l\left(\frac{2\mu}{\rho}\bar{S}_{kl} - \tau^r_{kl} - \frac{\bar{p}}{\rho}\delta_{kl}\right)\right] = -\frac{2\mu}{\rho}\bar{S}_{kl}\bar{S}_{kl} - P_r, \tag{5.21}$$

where $P_r = -\tau^r_{kl}\bar{S}_{kl} = \nu_r\left|\bar{\mathbf{S}}\right|^2 \geq 0$ if $\nu_r \geq 0$. Hence, in the model given by equations (5.18) and (5.19), kinetic energy is removed from the mean flow. Observe also the kinetic energy removed due to the viscosity μ.

5.5 Weak incompressibility

Exact incompressibility can be imposed in SPH [13] by solving the Poisson equation for pressure at every time step. For the simulation of nearly incompressible fluids, the method often used in SPH is to allow the density to vary by a small amount, usually to within 1 percent of the mean density.

In particular, for the case of water, an equation of state [11] used in SPH is

$$p \;=\; B\left[\left(\frac{\rho}{\rho_0}\right)^{\gamma} - 1\right] + p_{atm}, \tag{5.22}$$

where p is the pressure, ρ is the density, $\gamma = 7.0$, ρ_0 is the density at atmospheric pressure, B is a constant to be determined, and p_{atm} is the atmospheric pressure. To avoid additional particles needed to enforce the atmospheric pressure above the water-level, we take $p_{atm} = 0$, thus avoiding additional computational effort.

Due to compressibility, the CFL condition restricts the timestep to small values for nearly incompressible fluids. To overcome this restriction to some extent, it is customary to use an artificial speed of sound in SPH. The artificial speed of sound is estimated as follows. It can be shown that the terms

$$\frac{\Delta\rho}{\rho} \text{ and } \frac{u^2}{c^2} \tag{5.23}$$

are of the same order, where $\Delta\rho$ is the allowed maximum variation in density, u is a typical velocity scale, and c is the speed of sound. Hence, as an approximate estimation, the speed of sound is chosen to be 10 times the maximum velocity expected in the experiment to keep the density variation to within 1 percent. Hence, the constant B in (5.22) is chosen so that the speed of sound

$$c^2 = (10u)^2 = \frac{\partial p}{\partial \rho} \approx \frac{B\gamma}{\rho_0}. \tag{5.24}$$

One problem in using (5.22) as the equation of state with $p_{atm} = 0$ is that the pressure can become negative, thus exhibiting non-physical behaviours in experiments.

5.6 SPH-LES of weakly incompressible fluids

As usual, for compressible fluids, density-weighted mean quantities are introduced. For any physical quantity f, the density-weighted mean $\tilde{f}$ is defined by

$$\tilde{f} = \frac{\overline{\rho f}}{\bar{\rho}}. \tag{5.25}$$

This operation is also called Favre-averaging. Applying (5.25) to Navier-Stokes equations and rearranging terms [3], we get

$$\frac{\partial \bar{\rho}}{\partial t} + \nabla \cdot (\bar{\rho}\tilde{\mathbf{u}}) = 0 \tag{5.26}$$

$$\frac{\partial (\bar{\rho}\tilde{\mathbf{u}})}{\partial t} + \nabla \cdot (\bar{\rho}\tilde{\mathbf{u}} \otimes \tilde{\mathbf{u}}) + \nabla \bar{p} - \nabla \cdot \tilde{\sigma} = A + B \tag{5.27}$$

$$\frac{\partial (\bar{\rho}\tilde{e})}{\partial t} + \nabla \cdot (\bar{\rho}\tilde{\mathbf{u}}\tilde{e}) + \bar{p}\nabla \cdot \tilde{\mathbf{u}} - \tilde{\sigma}\tilde{S} = -C - D + E \tag{5.28}$$

where

$$\begin{aligned} A &= -\nabla \cdot \left[\bar{\rho}(\mathbf{u}\widetilde{\otimes}\mathbf{u} - \tilde{\mathbf{u}} \otimes \tilde{\mathbf{u}})\right] = -\nabla \cdot \tau \\ B &= \nabla \cdot (\bar{\sigma} - \tilde{\sigma}) \\ C &= \nabla \cdot [\bar{\rho}\,(\widetilde{\mathbf{u}e} - \tilde{\mathbf{u}}\tilde{e})] \\ D &= \overline{p\nabla \cdot \mathbf{u}} - \bar{p}\widetilde{\nabla \cdot \mathbf{u}} \\ E &= \overline{\sigma\mathbf{S}} - \tilde{\sigma}\tilde{\mathbf{S}} \end{aligned} \tag{5.29}$$

and, in Einstein notation,

$$\begin{aligned} \sigma_{kl} &= \mu\left(\tfrac{\partial u_k}{\partial x_l} + \tfrac{\partial u_l}{\partial x_k} - \tfrac{2}{3}\tfrac{\partial u_m}{\partial x_m}\delta_{kl}\right) \\ \sigma\mathbf{S} &= \sigma_{kl}S_{kl} \\ S_{kl} &= \tfrac{1}{2}\left(\tfrac{\partial u_k}{\partial x_l} + \tfrac{\partial u_l}{\partial x_k}\right). \end{aligned} \tag{5.30}$$

A is the sub-grid scale (SGS) Reynolds stress tensor, C is the divergence of SGS heat flux, D is the SGS pressure dilation, and E is the SGS viscous dissipation. Term B is often neglected and the other terms are modelled [14]. The anisotropic part of $\tau_{kl} = \bar{\rho}\,(\widetilde{u_k u_l} - \tilde{u}_k\tilde{u}_l)$ is modelled as

$$\tau_{kl} - \frac{\delta_{kl}}{3}\tau_{mm} = -2\bar{\rho}\nu_r\left(\tilde{S}_{kl} - \frac{\delta_{kl}}{3}\tilde{S}_{mm}\right). \tag{5.31}$$

Moreover, the term τ_{mm} is expressed using the formula [16]

$$\tau_{mm} = 2C_I\bar{\rho}\Delta^2\left|\tilde{\mathbf{S}}\right|^2, \tag{5.32}$$

where the eddy viscosity $\nu_r = C_s\Delta^2\left|\tilde{\mathbf{S}}\right|$, $\left|\tilde{\mathbf{S}}\right| = (2\tilde{S}_{kl}\tilde{S}_{kl})^{1/2}$, $C_s = 0.12$ is the Smagorinsky constant, and $C_I = 0.0066$ is an empirical constant. For simplic-

ity, following Blin et al. [10], neglect terms B, C, D, and E in (5.27) and (5.28). Then the set of discretized SPH equations can be written as

$$\begin{aligned}
\frac{d}{dt}(\bar{\rho}_i \tilde{\mathbf{u}}_i) &= -\sum_j \frac{m_j}{\bar{\rho}_i \bar{\rho}_j} (\bar{p}_i + \bar{p}_j) \nabla_i \psi_{ij} \qquad (5.33) \\
&\quad + \sum_j \frac{m_j}{\bar{\rho}_i \bar{\rho}_j} (\tilde{\sigma}_i + \tilde{\sigma}_j) \cdot \nabla_i \psi_{ij} \\
&\quad - \sum_j \frac{m_j}{\bar{\rho}_i \bar{\rho}_j} (\tau_i + \tau_j) \cdot \nabla_i \psi_{ij}, \\
\frac{d}{dt}(\bar{\rho}_i \tilde{e}_i) &= -\bar{p}_i \sum_j \frac{m_j}{\bar{\rho}_i \bar{\rho}_j} (\tilde{\mathbf{u}}_j - \tilde{\mathbf{u}}_i) \cdot \nabla_i \psi_{ij} + \tilde{\sigma}_i \tilde{\mathbf{S}}_i. \qquad (5.34)
\end{aligned}$$

Equations (5.33) and (5.34) can be used to simulate fluid flows with lower artificial viscosity values; the dissipation introduced by the third term in (5.33) contributes to the stability of the numerically scheme.

Chapter 6

Simulations

In this chapter, we will first discuss how boundary conditions are imposed in SPH. Then some tools commonly used in SPH simulations are briefly explained. The remaining sections concentrate on simulations. In most simulations, we often refer to two constants α and β, which are constants found in the artificial viscosity Equation (3.18). In simulations and figures, SPH refers to the weak formulation given by (3.79)-(3.83), R-SPH refers to the weak renormalized formulation given by (4.19)-(4.23), and LES-SPH refers to weak non-renormalized SPH with the LES filter given by (5.33). For the simulations in Sections 6.3 and 6.4, Shepard filtering is applied every 40 iterations, and XSPH is not used (see Section 6.2).

6.1 Boundary conditions

Commonly used boundary conditions in CFD are given in the list below.

- Free-slip-absorbing
- No-slip-absorbing
- Free-slip-reflective
- No-slip-reflective
- Periodic

Let us consider how these boundary conditions are imposed in SPH. Let $\mathbf{u}_i = (u_i, v_i)$ be the velocity of particle i. We restrict the discussion to plane boundaries and corners formed by planes. For the ease of explanation, let us first sort particles into two categories: inner and boundary-influenced particles. For particles near a plane boundary, boundary-influenced particles are defined by the following procedure. For the purpose of illustration, we consider a vertical plane boundary located at $x = l$, and assume that the kernel used has a radius of influence 2ϵ. The radius

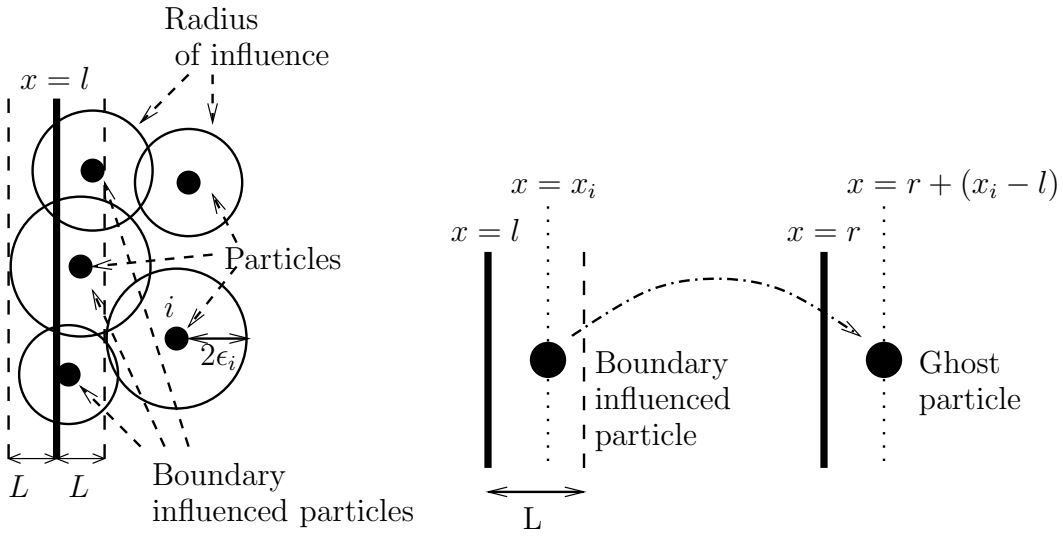

Figure 6.1: Creating ghost particles

of influence is 2ϵ if the kernel (2.19) is used, where ϵ is the smoothing length. As Figure 6.1 illustrates, the domain is assumed to be on the right side of the boundary. We take

$$L = \max_i \{2\epsilon_i - (x_i - l)\}, \tag{6.1}$$

and define the set of boundary-influenced particles B as

$$B = \{i | x_i - l < L\} \tag{6.2}$$

To create a free-slip-reflective boundary, boundary-influenced particles are projected orthogonally. The reflected particles, called ghost particles, are assigned the same density, pressure, smoothing length, and internal energy as their corresponding real particles. Since we require a free-slip-reflective boundary condition for the velocity, the same vertical velocity is assigned but the horizontal velocity is reversed in direction. For the no-slip-reflective boundary condition, both velocities are reversed in the ghost particle.

Now consider two vertical boundaries at positions $x = l$ and $x = r$, and assume that the domain is within these two vertical boundaries, as shown in Figure 6.1. To impose periodic boundary conditions, if i is a boundary-influenced particle near the left boundary, the corresponding ghost particle is created and placed at $r + (x_i - l)$. Obviously, the velocities of real particles are not altered when assigning to ghost particles. Furthermore, if particle re-injection is required, we carry out the following procedure. Consider a particle i that crosses the left boundary located at $x = l$. Then it is placed at the position $r + (x_i - l)$ in the next iteration, where $x = r$ is the position of the right boundary.

6.2 Commonly used tools

Shepard filtering

In simulations, especially those with free-surfaces or inter-facial flows, non-physical effects such as bumpy surfaces can be observed. In SPH, non-physical bumpy interfaces are smoothed by using a higher value of artificial viscosity. If the artificial viscosity used is very small, these non-physical effects have to be corrected by other means. As the artificial viscosity used in SPH-LES will be small, rugged free-surfaces are smoothed by using Shepard filtering, which is a density filter given by

$$\rho_i = \frac{\sum_j \rho_j \omega_j \psi_{ij}}{\sum_j \omega_j \psi_{ij}}. \tag{6.3}$$

Shepard filtering is an averaging procedure. Shepard filtering is actually a correction for the zeroth order consistency. In the continuum, the kernel function satisfies the normalization condition

$$\int_\Omega \psi_\epsilon(x) = 1. \tag{6.4}$$

Once discretized, this property is lost:

$$\sum_j \omega_j \psi_\epsilon(x_j) \approx 1. \tag{6.5}$$

Thus, by performing Shepard filtering, zeroth order consistency is restored in the discretized integral. For simulations in this thesis, Shepard filtering is applied to the whole domain every 40 time steps.

XSPH

This is a method whereby a particle is moved with a velocity that is closer to the average velocity in its neighbourhood. XSPH helps keep particles orderly. It has been shown that XSPH increases dispersion, but does not increase dissipation [17]. In XSPH, particle position is updated using

$$\frac{d\mathbf{r}_i}{dt} = \mathbf{u}_i + \epsilon \sum_j \frac{m_j}{\bar{\rho}_{ij}} \mathbf{u}_{ji} \psi_{ij}, \tag{6.6}$$

where $\bar{\rho}_{ij} = \frac{\rho_i + \rho_j}{2}$ and $0 \leq \epsilon \leq 1$; $\epsilon = 0.5$ is commonly used. XSPH will not be used for the simulations in this thesis.

NOTE: Shepard filtering and XSPH methods require the evaluation of ψ_{ij}, which requires extra computational effort.

Repulsive boundary particles

In this thesis, boundaries are created using ghost particles. As described in Section 6.1, boundary conditions are imposed using ghost particles by reflecting boundary-influenced particles across boundaries and assigning appropriate appropriate velocities. In complex geometries, it is sometimes impossible to impose perfect boundary conditions.

Complex geometries are easiest to construct if repulsive boundary particles are used. This involves placing particles with repulsive forces along the boundary. No-slip boundary condition is imposed by considering the velocity of boundary particles to be zero and including the repulsive boundary particles when calculating the velocities of non-boundary particles. When free-slip boundary conditions are imposed, inner particles interact with repulsive boundary particles only by the force they exert. A simple boundary force f takes the Lennard-Jones form [17]

$$f(r) = \begin{cases} D\left(\left(\frac{r_0}{r}\right)^{p_1} - \left(\frac{r_0}{r}\right)^{p_2}\right)\frac{\mathbf{r}}{r^2}, & \text{if } r \leq r_0, \\ 0 & \text{otherwise,} \end{cases} \tag{6.7}$$

where $p_1 \geq p_2$, $\mathbf{r}$ is a vector with direction away from the boundary particle, $r = \|\mathbf{r}\|$ is the distance between the boundary and boundary-influenced particles (see Figure 6.2), and $D, r_0 \geq 0$ are constants. (6.7) creates a rugged boundary. More sophisticated boundary forces are used to create smoother boundaries [9].

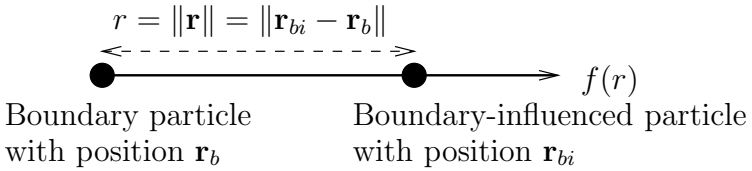

Figure 6.2: Lennard-Jones force

Handling particles that cross boundaries

Sometimes a particle may pass through a boundary. For simulations in this thesis, either those particles are removed from the domain or are placed back to the domain using the following procedure. Consider a particle i passing through a vertical boundary located at $x = l$. The domain is assumed to be on the right of the boundary. Then the x-coordinate of the particle is given by the value

$$x_i = l + \Delta z, \tag{6.8}$$

where Δz is a small fixed number, which depends on the initial inter-particle distance. In particle methods, there are many other techniques used to handle particles that cross boundaries.

6.3 2D dam breaking

The initial profile is shown in Figure 6.3(a). Particles are placed in a rectangular area, the blue region in the figure. The number of particles used is roughly 3000 and the time-step used is 5.0×10^{-5} sec.

In Figures 6.3(b)-6.5, free-slip boundary condition is imposed; in the figures, red indicates higher and blue indicates lower horizontal velocity. This experiment has been carried out before using SPH Equations (3.50)-(3.54) [17] with boundaries constructed by repulsive boundary particles. We compare the results with those obtained for R-SPH given by (4.19)-(4.23), and SPH given by (3.79)-(3.83). Table 6.1 gives the distance the water front travels with time. H is the maximum height of the water column, and L is the maximum horizontal distance travelled; "exp" indicates results obtained by a real experiment, and "SPH" refers to results obtained by using SPH. Figures 6.4 and 6.5 show the profile at the two times $t = 1.1$, 2.2

Table 6.1: Data from the dam breaking problem

Time	H(exp)	H(SPH)	L(exp)	L(SPH)
1.1	22.5	22.5	33.3	39.0
2.2	19.0	18.7	56.2	62.5

sec for SPH and R-SPH with free-slip boundary conditions. Observe that R-SPH gives a smoother velocity profile. The distance travelled is very nearly the same for both methods.

Results for the same experiment with no-slip boundary condition is shown in Figure 6.6. According to Table 6.1, the horizontal distance travelled when $t = 2.2$ is 56.2; thus, the profile at $t = 2.2$ given by the simulations is much closer to the experimental results when no-slip boundary conditions are used.

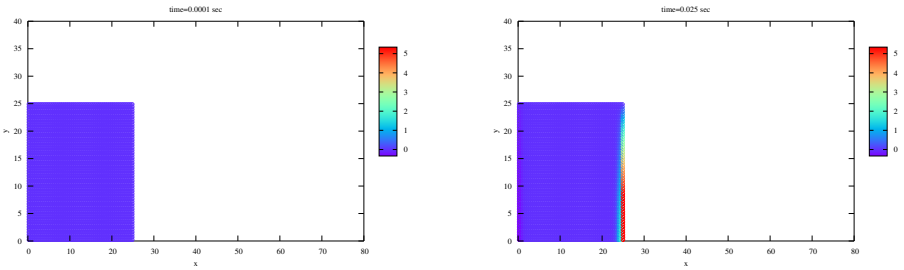

(a) Initial profile (b) Just after release

Figure 6.3: Dam break, free-slip, initial profiles

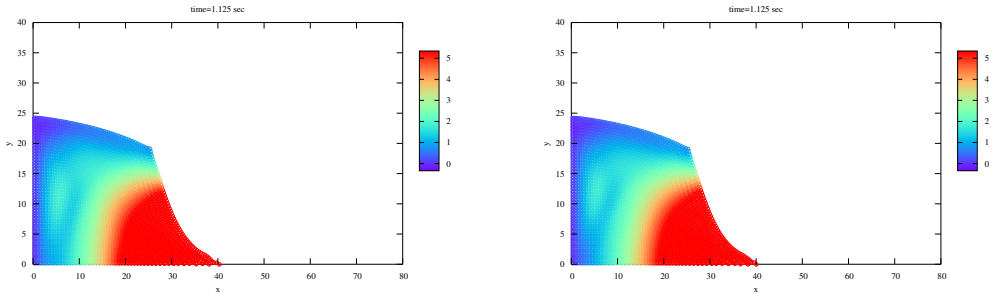

(a) SPH (b) R-SPH

Figure 6.4: Dam break, free-slip, $t = 1.1$ sec

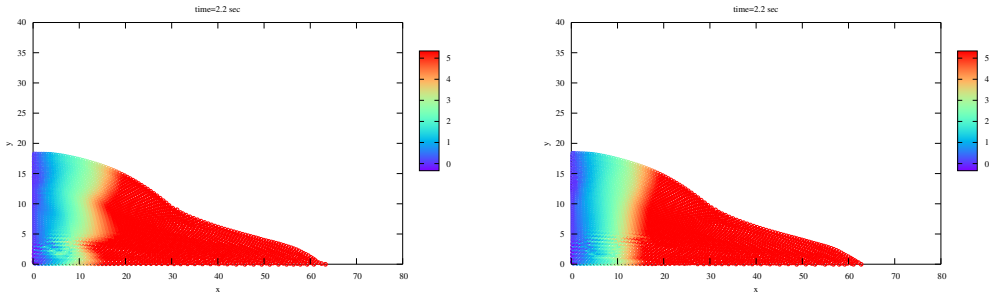

(a) SPH (b) R-SPH

Figure 6.5: Dam break, free-slip, $t = 2.2$ sec

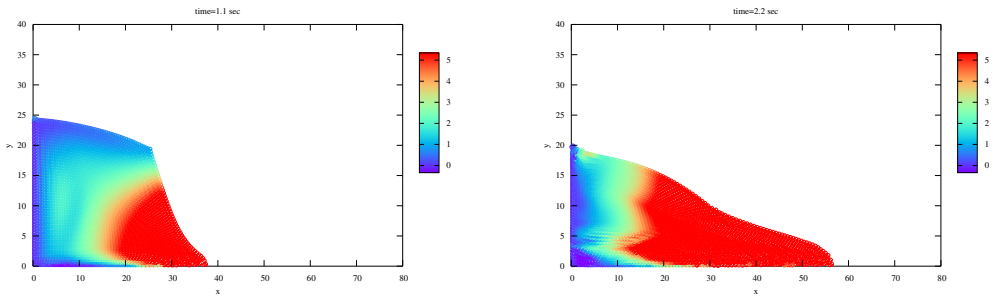

(a) SPH, $t = 1.1$ sec (b) SPH, $t = 2.2$ sec

Figure 6.6: Dam break, no-slip

6.4 2D Surface waves

Consider Figures 6.7(a)-(f), which show a rolling wave on a sloping beach. The simulation was carried out by Dalrymple and Rogers [9] using LES-SPH. Figures 6.7(d)-(f) seem to capture fine details of particle motion after the wave breaks. In Figures 6.7(a)-(f), red indicates higher horizontal velocity.

The simulation in [9] has not been validated with real data. Given the way the

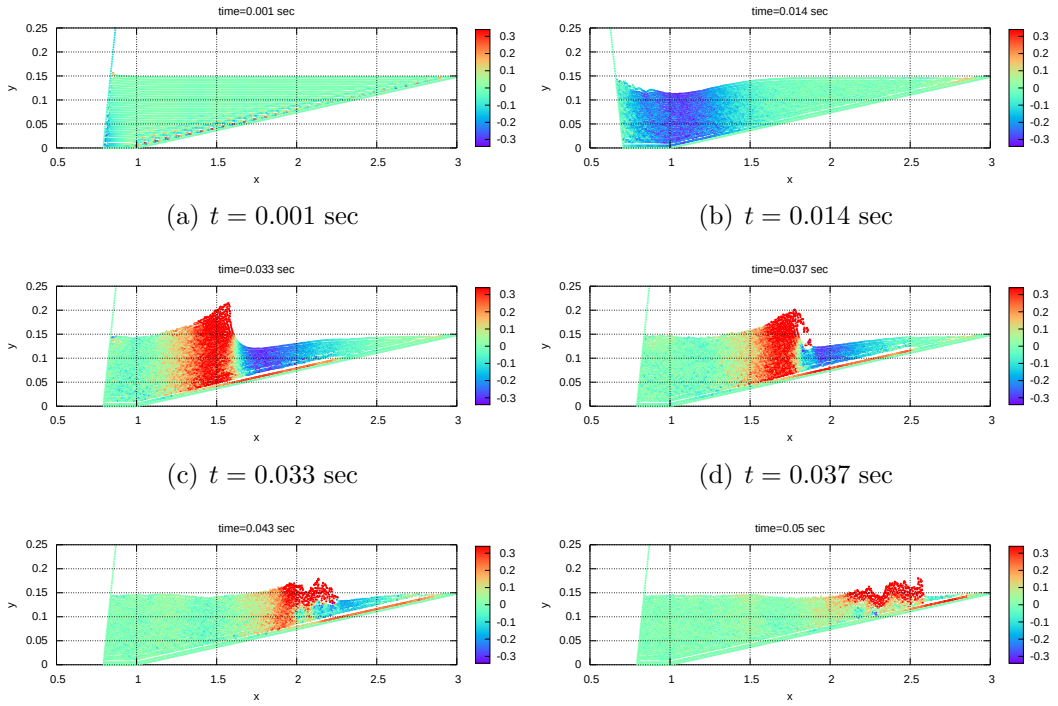

(a) $t = 0.001$ sec (b) $t = 0.014$ sec

(c) $t = 0.033$ sec (d) $t = 0.037$ sec

(e) $t = 0.044$ sec (f) $t = 0.050$ sec

Figure 6.7: Wave tank with a paddle, SPH

experiment is set up, it is difficult to gauge the accuracy of the structures seen in the Figures 6.7(d)-(f). Apart from the small-scale details, Figures 6.7(a)-(c) seem to also suggest that the paddle of the wave generator helps break the wave. In Section 6.4.1, a number of simulations will be carried out using solitary waves to determine the accuracy of the SPH scheme for predicting stable, and breaking solitary waves.

To highlight the differences in the simulation we perform and that in [9], we give exactly how the simulation was set up in [9]. The initial configuration of the simulation is shown in Diagram 6.8. The left boundary, the piston-paddle, is the only moving boundary; the bottom and the left slopes are fixed. The piston flaps as it moves, thus the name piston-paddle. In CFD, some of the common boundary conditions imposed are given in Section 6.1. In [9], such boundary conditions are not imposed. Instead of ghost particles, repulsive particles are used to make the boundary. The paddle is moved with sufficient amplitude and frequency to generate

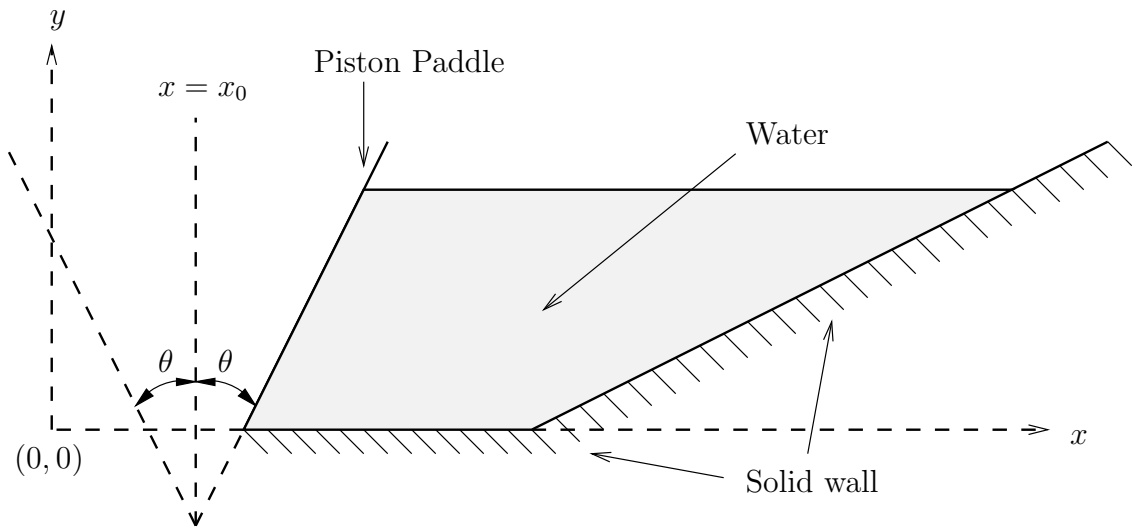

Figure 6.8: Wave tank with paddle and slope

breaking waves. In the simulation, any point (x, y) in the paddle is moved according to the relation

$$x = x_0 + \frac{1}{2}\left(\frac{y + \alpha_0}{y_0 + \alpha_0}\right) A(t), \tag{6.9}$$

where $\alpha_0 = 0.1344$, $y_0 = 0.15$, $A(t) = A\cos(\omega t)$, $A = 0.2442$, and $\omega = 2\pi f$. The form of the equation is not important. The idea is to create breaking waves. The boundary force used takes the form [18]

$$\mathbf{f} = \mathbf{n} R(y) P(x), \tag{6.10}$$

where $\mathbf{n}$ is the unit direction vector normal to the boundary, x is the tangential distance from a boundary particle, y is perpendicular distance from the boundary, Δp is the initial particle spacing,

$$R(y) = \begin{cases} \frac{A}{\sqrt{q}}(1 - q), & \text{if } q \leq 1, \\ 0, & \text{otherwise,} \end{cases} \tag{6.11}$$

$$P(x) = \begin{cases} \frac{1}{2}\left(1 + \cos\left(\frac{\pi x}{\Delta p}\right)\right), & \text{if } x \leq \Delta p, \\ 0, & \text{otherwise.} \end{cases} \tag{6.12}$$

Function (6.10) is designed to mimic the force exerted by a smooth boundary, instead of the rugged boundary created by boundary particles exerting central forces similar to Lennard-Jone forces. For simulations in this thesis, repulsive boundary particles are not used. Instead, ghost particles are used to create boundaries, as discussed in Section 6.1. In addition, a paddle is not used to generate waves. In

[9], Morris's formulation (5.7) is used to model the viscous term; however, in this thesis, (5.4) is used.

6.4.1 Solitary waves

Solitary wave was first observed by J. Scott Russel in 1834. A solitary wave has the ability to travel long distances without decaying or changing shape. Solitary waves can be easily generated and observed in nature. Surface solitary waves can be observed as bell-shaped translating waves on liquid surfaces. Solitary waves acquire stability by a fine balance between weak non-linearity and dispersion. Some parameters that characterizes a solitary waves is shown in Diagram 6.9. H is the water depth, A is the amplitude of the solitary wave, λ is the wave width. Now we define some secondary parameters which characterizes the solitary waves. The shallow water linear wave speed c_l in a liquid of depth H is given by

$$c_l = \sqrt{gH}, \tag{6.13}$$

where $g = 9.81$ is gravitational constant. The KdV equation that governs solitary waves is given by

$$\eta_t = -c_l\eta_x - \frac{3}{2}\frac{c_l}{H}\eta\eta_x - \frac{1}{6}H^2\eta_{xxx}, \tag{6.14}$$

where η defines the wave profile. One of the solutions of (6.14) is a solitary wave given by

$$\eta(x,t) = A\ \mathrm{sech}^2\left(\frac{x - Vt}{\lambda}\right), \tag{6.15}$$

where

$$V = c_l\left(1 + \frac{A}{2H}\right), \tag{6.16}$$

$$\lambda = \sqrt{\frac{4H^3}{3A}}. \tag{6.17}$$

The width λ is the horizontal distance from the peak position at which $\eta \approx 0.4A$.

One of the remarkable properties of KdV solitary waves is their ability to overtake and interact with other solitary waves and reemerge unchanged.

The stability of solitary waves depend on the depth of the water. An approximate condition for stable solitary waves at a *constant depth* is [22]

$$\frac{A}{H} < 0.78. \tag{6.18}$$

Beyond this limit, solitary waves will continuously steepen and eventually break.

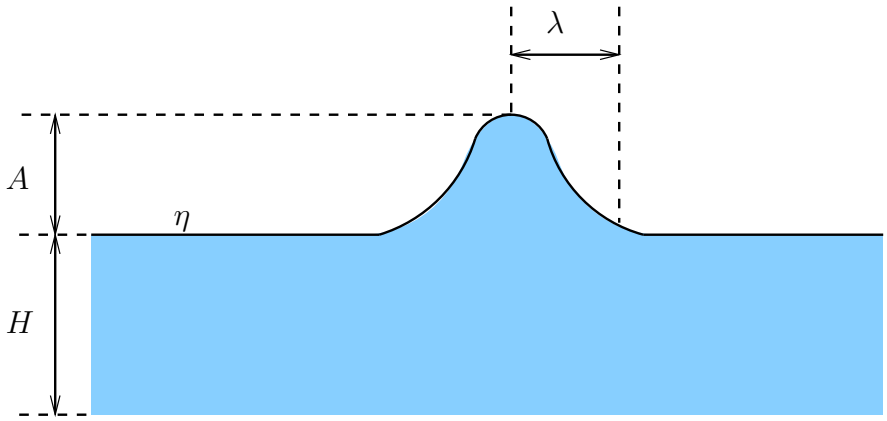

Figure 6.9: Solitary wave parameters

An approximate condition for the stability of solitary waves in a beach with *plane slope* is [23]

$$\frac{A}{H} < 16.9s^2, \tag{6.19}$$

where s is the slope ratio. Solitary waves that do not satisfy condition (6.19) will break as a plunging, surging, collapsing, or spilling breaker. Moreover, a simple relation categorizing the type of the breaker is given in Table 6.2, where S_0 is given by

$$S_0 = 1.521\frac{s}{\sqrt{\frac{A}{H}}}. \tag{6.20}$$

Table 6.2: Conditions determining breaker types

Type of breaker	Condition
Surging	$0.3 < S_0 < 0.37$
Plunging	$0.025 < S_0 < 0.30$
Spilling	$S_0 < 0.025$

Speed of solitary waves in a long tank

The initial configuration of the simulation is shown in Figure 6.10. The length of the tank $L = 12$ m, and water height $H = 0.15, 0.20$ m. The water surface is

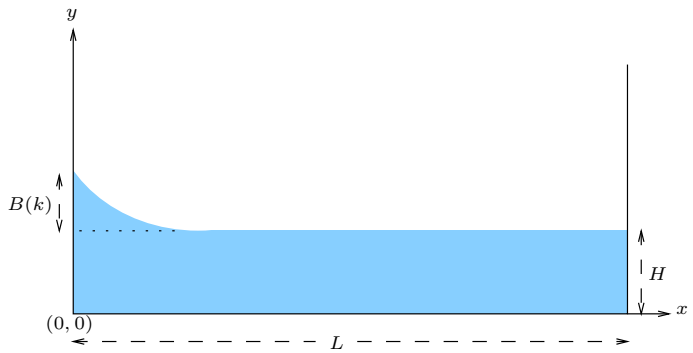

Figure 6.10: Simulation set up of the tank

defined by

$$y = B(k)\exp(-kx) + H, \tag{6.21}$$

where $B(k)$ is a function of k. Values of k used are given in Table 6.3. The form of

Table 6.3: Values of k and B used

k	B(k)
1.5	0.25
2.0	0.12
2.5	0.07

(6.21) is not important, the idea is to create a solitary wave. We compare the wave speed given by SPH, R-SPH, LES-SPH, and the speed given by (6.16). The number of particles used for the experiment is roughly 20,000 for H=0.15, and 25,000 for H=0.20. The time-step used is 5.0×10^{-5}. The speed of sound used is 83 m/s.

The evolution of the wave amplitude for $H = 0.15$ and $k = 2.0$ is shown in Figure 6.11(a). Observe the significant difference in amplitude when SPH-LES is used. LES[1] uses a smaller time step compared to LES[2]. The dependence of the profile on the time step can be an indication of an instability. For the smaller time step used in LES[1], the reduction in the amplitude of the wave can be due to the higher frequency at which Shepard filtering is applied; Shepard filtering smooths density, hence resulting in the smoothing of pressure, velocity, and energy fields as well. Shepard filtering occurs every 40 iterations. Observe also the growth in the amplitude with time. Figure 6.11(b) is a plot of the position of the wave-peak with time. The slope of the curve gives the speed of the wave.

Wave speeds and heights for $H = 0.15$ and $k = 2.0, 2.5$ are shown in Figures 6.11 and 6.13; readings taken from the figures are given in Table 6.4. The speeds were taken for the time interval 3.0 to 7.0 seconds. For both SPH and R-SPH, $\alpha = 0.5$ and $\beta = 1.0$, where α and β are constants in the artificial viscosity (3.18). "sim" indicates results taken directly from the simulation. The amplitude in the middle row was calculated using the speed taken from the simulation and (6.16). One entry

Table 6.4: Simulation results for $H = 0.15$

k	2.0			2.5		
Method	SPH	R-SPH	LES-SPH	SPH	R-SPH	LES-SPH
Speed(sim)	1.423	1.392	1.456	1.359	1.295	1.347
Amplitude	0.052	0.044	0.060	0.036	0.020	0.033
Amplitude(sim)	0.030	0.030	0.060	N/A	0.013	0.027

is not available (N/A) as the wave amplitude showed non-physical growth. For the same initial conditions, the speeds are different for SPH and R-SPH. In Table 6.4, observe that the amplitudes obtained by R-SPH and LES-SPH are closest to that predicted by (6.16) for the smaller amplitude wave ($k = 2.5$). For the higher amplitude wave ($k = 2.0$), SPH and R-SPH under-determines the amplitude compared to LES-SPH. This underestimation is as expected since the diffusivity is higher in SPH and R-SPH as $\alpha = 0.5$, whereas $\alpha = 0.0$ in LES-SPH. For the data in Table 6.4, $0.13 < A/H < 0.33$.

For $H = 0.20$, wave speed and height of solitary waves for the SPH and R-SPH schemes are shown in Figures 6.14-6.16; readings taken from the figures are given in Table 6.5. The speeds were taken for the time interval 3.0 to 7.0 seconds. For both SPH and R-SPH, $\alpha = 0.5$ and $\beta = 1.0$. As before, for the speeds given by the simulation, the wave amplitude given by (6.16) is calculated and compared with the wave amplitude given by the simulation. Again, we can observe that the wave amplitude given by the simulation is smaller than expected. For the R-SPH, the difference between the amplitude obtained by the simulation and (6.16) is much less.

Table 6.5: Simulation results for $H = 0.20$

k	1.5		2.0		2.5	
Method	SPH	R-SPH	SPH	R-SPH	SPH	R-SPH
Speed(sim)	1.785	1.785	1.602	1.538	1.537	1.454
Amplitude	0.110	0.110	0.058	0.039	0.039	0.015
Amplitude(sim)	0.070	0.085	0.030	0.032	0.016	0.014

Let us now make a rough estimation of the parameters of the solitary wave that will be formed if all the water initially above the $y = H$ level is used for the formation of the solitary wave. Equating the areas

$$\int_0^\infty [y(x) - H]dx = \int_{-\infty}^\infty \eta(x)dx, \tag{6.22}$$

we get the relation

$$A = \frac{3}{H^3}\left[\frac{B(k)}{4k}\right]^2. \tag{6.23}$$

In Table 6.6, for each k, the amplitude A and speed is obtained from (6.23) and (6.16); then, for each pair (k, A), the ratio A/H is calculated using (6.23) and compared with (6.18) for stability. We compare the values of k for the formation

Table 6.6: Stability of solitary waves in constant depth

H	k	A	Speed	A/H	Stability
0.15	1.5	1.54	7.44	10.28	No
	2.0	0.20	2.02	1.33	No
	2.5	0.04	1.37	0.29	Yes
0.20	1.5	0.65	3.18	3.25	No
	2.0	0.08	1.46	0.42	Yes
	2.5	0.02	1.27	0.09	Yes

of a stable soliton with those obtained by simulations and listed in Tables 6.4 and 6.5. For $H = 0.15$, only $k = 2.5$ can be considered since the ratio A/H is much larger than 1 for cases $k = 1.5$ and $k = 2.0$. For $k = 2.5$, data indicates that all the water used to create the soliton have not been trapped in the soliton; the same is observed for $H = 0.20$, but the difference between the amplitudes given by (6.23) and the simulation is less. The diffusivity in the simulations, which tends to spread the soliton (see Section 6.4.2) more than that predicted by (6.15), may also increase the difference between the amplitudes obtained by (6.23) and the simulations.

Figures 6.17-6.19 show the wave profile for SPH, R-SPH, and LES-SPH for $k = 1.5$, 2.0, and $H = 0.15$; in the figures, red indicate higher horizontal velocity. As Table 6.6 indicates, the soliton formed for $k = 1.5$ is expected to be unstable. Observe the loss of symmetry due to the steepening of the solitary wave in the higher-amplitude wave. In LES-SPH, we can also see the larger soliton separating into two smaller solitons.

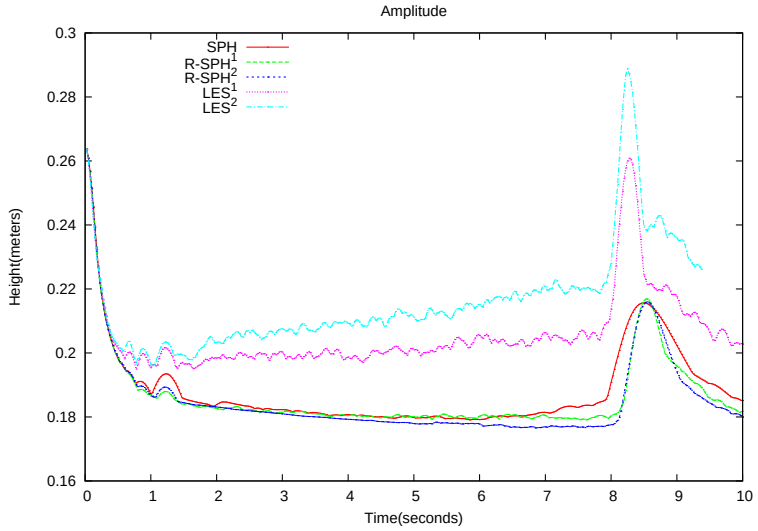

(a) Wave amplitude

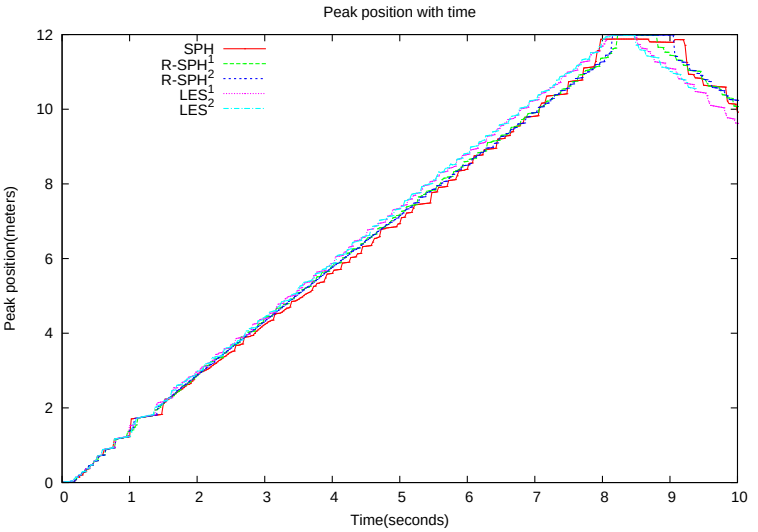

(b) Wave speed

Figure 6.11: Height and speed of the wave, long tank, H=0.15, k=2.0

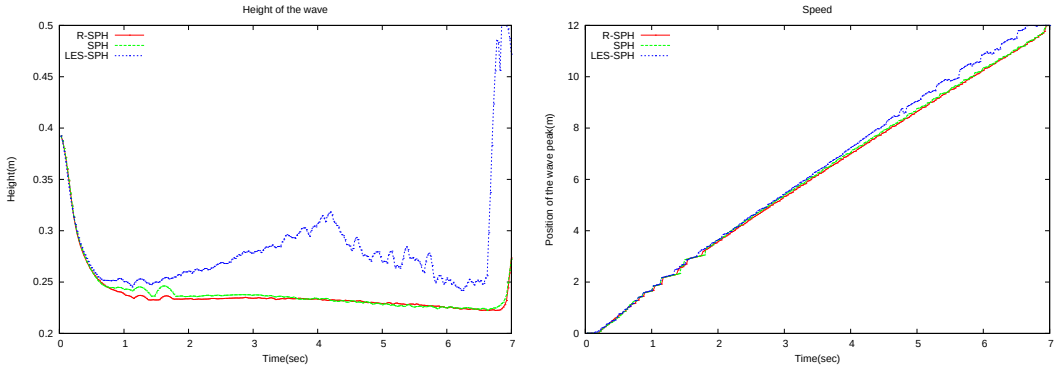

(a) Wave amplitude (b) Wave speed

Figure 6.12: Height and speed of the wave, long tank, $k = 1.5$, H=0.15

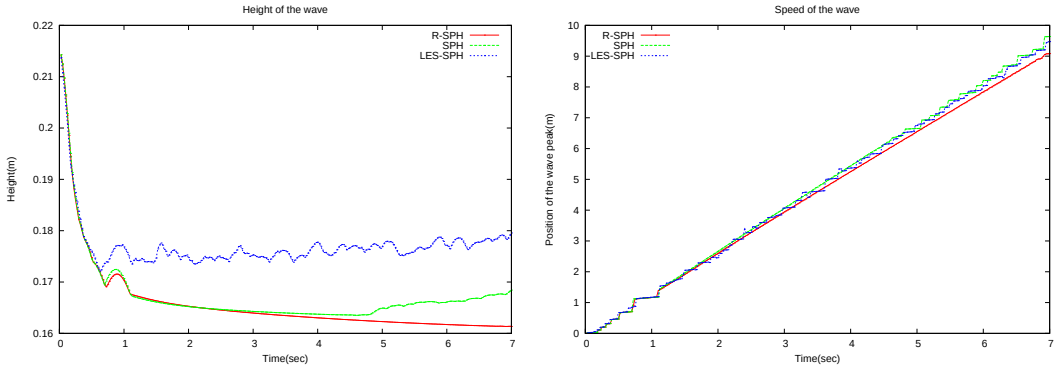

(a) Wave amplitude (b) Wave speed

Figure 6.13: Height and speed of the wave, long tank, $k = 2.5$, H=0.15

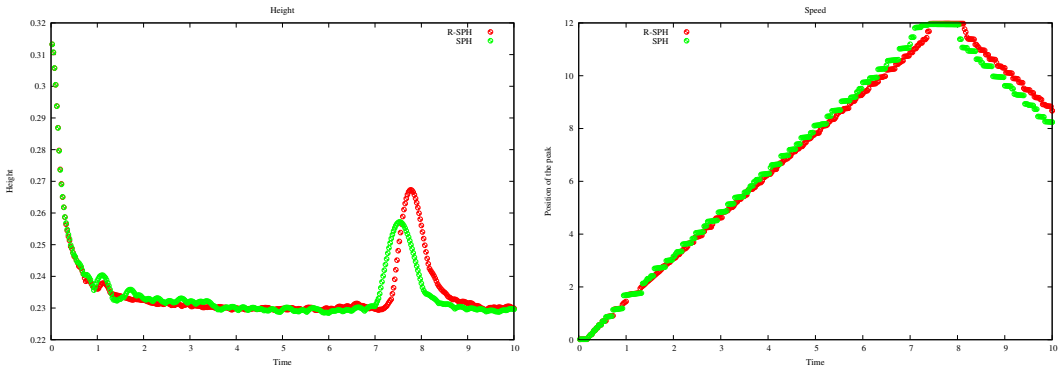

(a) Wave amplitude (b) Wave speed

Figure 6.14: Height and speed of the wave, long tank, k=2.0, H=0.20

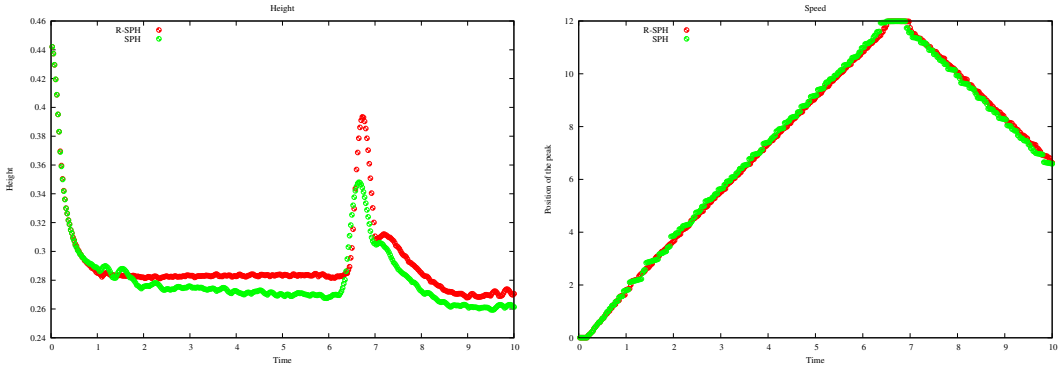

(a) Wave amplitude (b) Wave speed

Figure 6.15: Height and speed of the wave, long tank, k=1.5, H=0.20

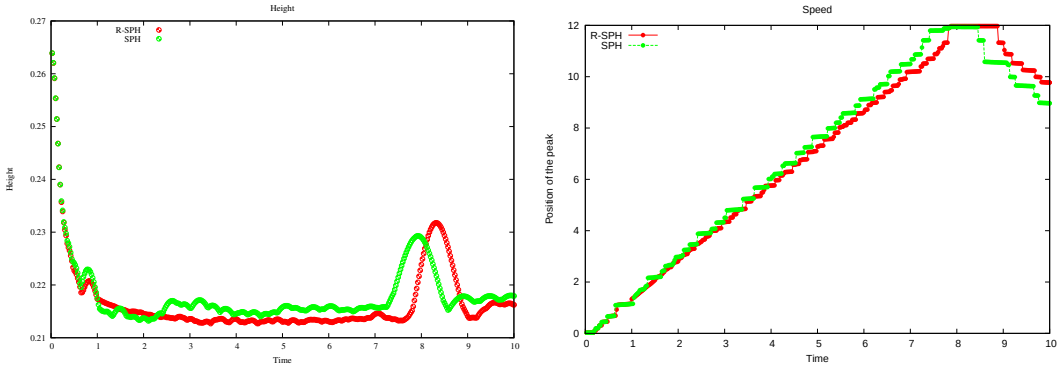

(a) Wave amplitude (b) Wave speed

Figure 6.16: Height and speed of the wave, long tank, k=2.5, H=0.20

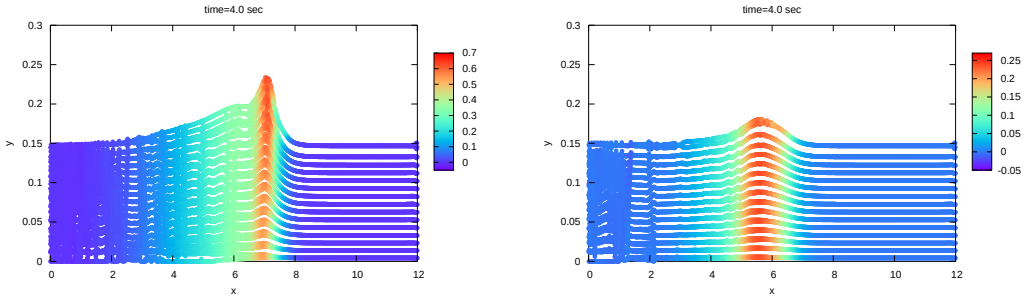

(a) k=1.5 (b) k=2.0

Figure 6.17: Wave profile, SPH, H=0.15, $t = 4.0$ sec

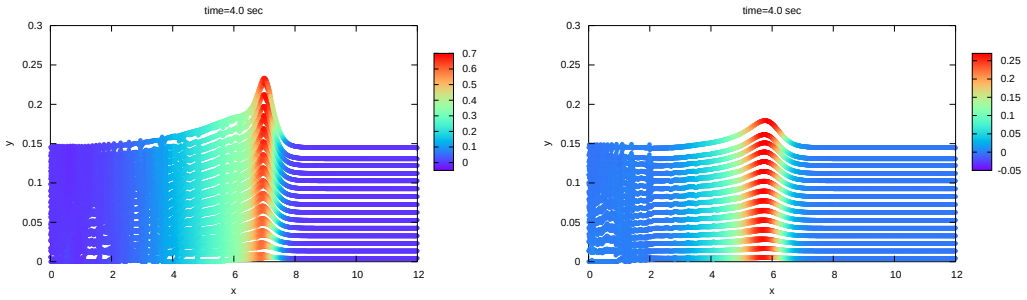

(a) k=1.5 (b) k=2.0

Figure 6.18: Wave profile, R-SPH, H=0.15, $t = 4.0$ sec

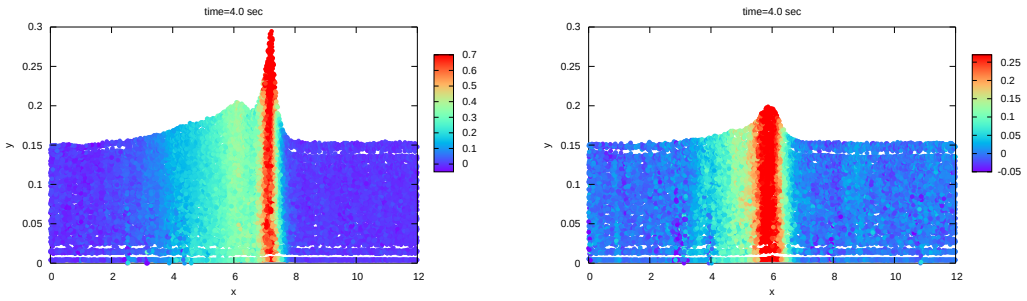

(a) k=1.5 (b) k=2.0

Figure 6.19: Wave profile, SPH-LES, H=0.15, $t = 4.0$ sec

6.4.2 Solitary waves in a periodic tank

Here we consider solitary waves in a tank with periodic boundary conditions. The length of the tank is shorter compared to the one investigated in Section 6.4.1, thus allowing the use of fewer particles. The downside of this method is that the front of the wave may interact with its tail unless the length of the tank is much larger compared to the width of the soliton. We use the same solitons as the ones used in Section 6.4.1.

In order to create the wave, we first use a tank with non-periodic boundary conditions and apply periodic boundary conditions once the wave has been formed ($t > 4$ sec). Since solitons transfer mass, particle re-injection is required at both boundaries. For this simulation, SPH and R-SPH use $\alpha = 0.5$ and $\beta = 1.0$. In LES-SPH, $\alpha = 0.0$ and $\beta = 0.0$. The number of particles used is roughly 10,000. The time-step used is 5.0×10^{-5} sec. The speed of sound used is 83 m/s.

Wave speed

Figures 6.20(a) and (b) show the speed and height of a solitary wave for $k = 2.0$ and $H = 0.15$; in the figures, red indicate higher horizontal velocity. Table 6.7 summarizes the speeds obtained for $k = 2.0$. The second time range is the time during which the wave travels across the tank for the second time; the second time range corresponds to the second line in Figure 6.20(a).

Table 6.7: Wave speed for $k = 2.0$

Time range	1.0-3.5	4.5-7.5
SPH	1.407	1.408
R-SPH	1.453	1.387
LES-SPH	1.477	1.431

Results obtained for $k = 2.5$ and $k = 1.5$ are shown in Figures 6.21 and 6.22. Table 6.8 summarizes the speed obtained for $k = 2.5$. Table 6.9 summarizes the

Table 6.8: Wave speed for $k = 2.5$

Time range	1.0-3.5	5.8-8.0
SPH	1.417	1.343
R-SPH	1.356	1.295
LES-SPH	1.370	1.338

speed obtained for $k = 1.5$. Observe that the speed of the wave generally slows

Table 6.9: Wave speed for $k = 1.5$

Time range	1.0-3.0	3.5-6.5
SPH	1.834	1.622
R-SPH	1.799	1.620
LES-SPH	1.823	1.769

down. On average, the slowdown is highest for R-SPH, followed by SPH, and LES-SPH. The wave may slowdown for a number of reason. One reason of interest here is the possibility of the wave slowing down due the way the tank is constructed. If the viscosity is high, the soliton may create a drag causing a slow up-current in the tank. This may cause the soliton to see a slower speed, thus decreasing its amplitude and speed. One possible solution to this problem is to use no-slip boundary conditions for the tank. However, diffusivity will also slowdown the wave, and aggravate the slowdown if no-slip boundary conditions are imposed.

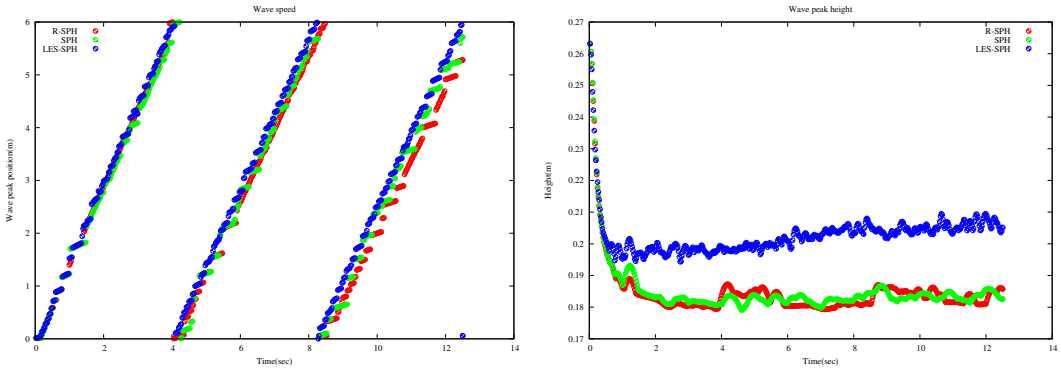

(a) Wave speed (b) Wave height

Figure 6.20: Speed and height of the wave, periodic tank, H=0.15, k=2.0

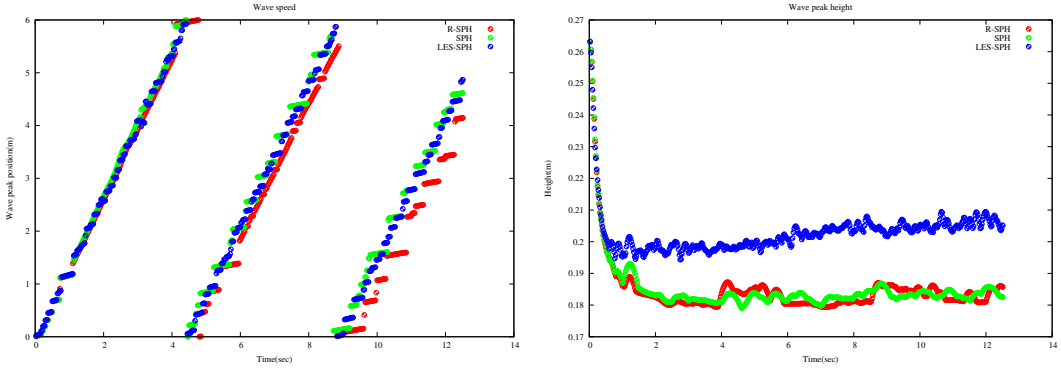

(a) Wave speed (b) Wave height

Figure 6.21: Speed and height of the wave, periodic tank, H=0.15, k=2.5

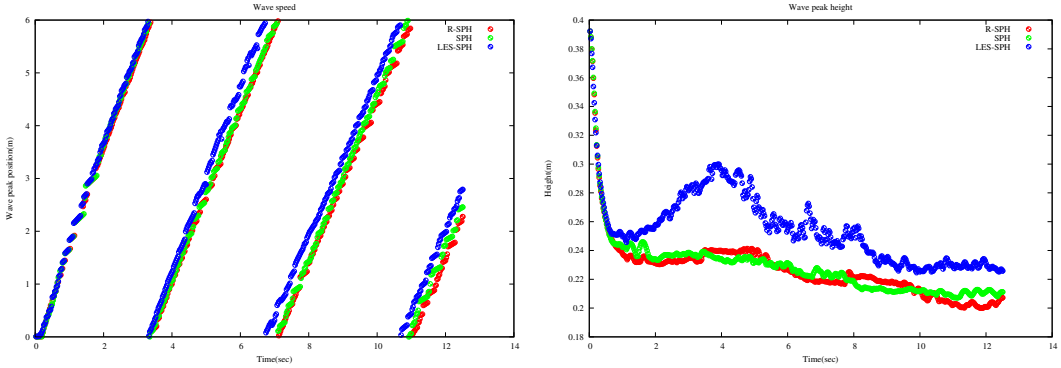

(a) Wave speed (b) Wave height

Figure 6.22: Speed and height of the wave, periodic tank, H=0.15, k=1.5

Wave shape

Here we compare the wave shape given by SPH, R-SPH, and LES-SPH methods. Figures 6.23-6.25 show the wave profile at time 2.5 seconds. The depth of the water is approximately 0.15 meters. For the wave profile generated, the amplitude is measured and the wave shape is compared with that given by (6.15). The line in green is the peak height of the wave; the line in blue is the curve defined by (6.15) for the amplitude obtained by the simulation. In Figures 6.25(a)-(c), red indicates higher horizontal velocity.

Observe that the wave generated by the simulation is slightly spread compared to the curve defined by (6.15). The difference between the curve defined by (6.15) and results obtained by the simulation is highest for $k = 2.0$, followed by $k = 2.5$. The case $k = 1.5$ was not compared since the soliton shows steepening, an indication that it is not stable. The reason for the larger spread is likely to be related to the diffusivity in the simulation. For this experiment, SPH and R-SPH show nearly the same profile. In LES-SPH, the water-air boundary is not well defined. The smaller diffusivity in the LES-SPH seems to make particles less orderly. Notice also that simulations using LES-SPH show steepening even for the case $k = 2.0$; higher artificial viscosity in R-SPH and SPH reduces the steepening effect.

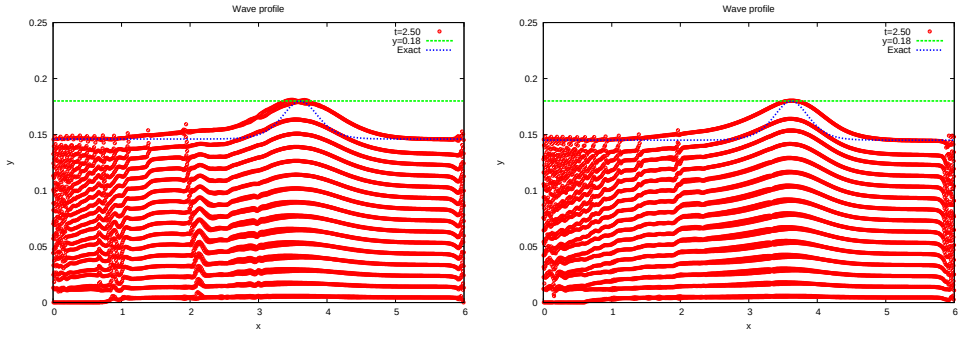

(a) SPH

(b) R-SPH

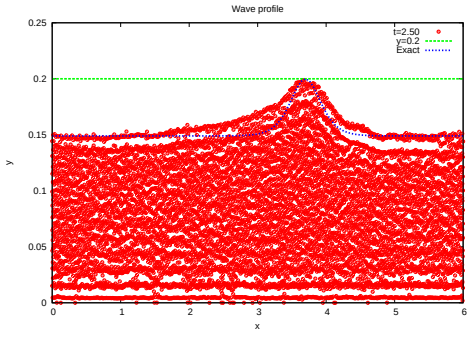

(c) LES-SPH

Figure 6.23: Wave profile, periodic tank, $k = 2.0$, $t = 2.5$ sec

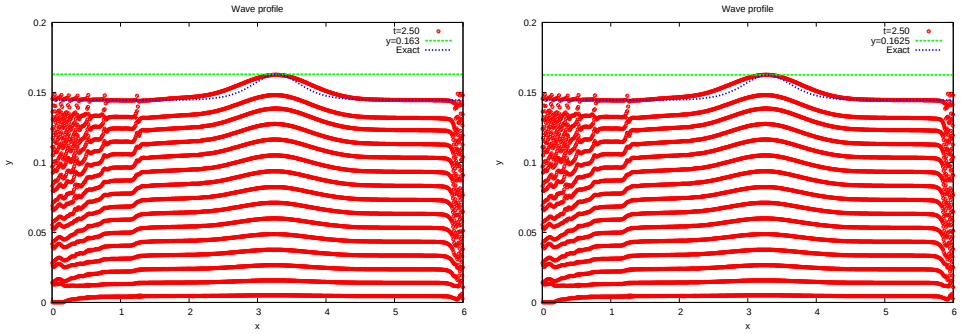

(a) SPH (b) R-SPH

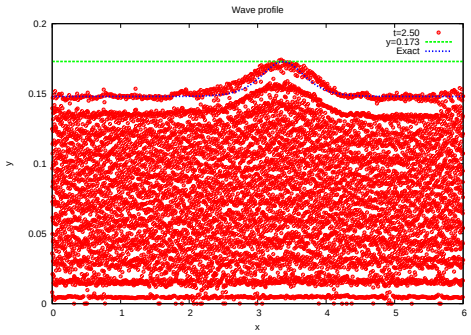

(c) SPH-LES

Figure 6.24: Wave profile, periodic tank, $k = 2.5$, $t = 2.5$ sec

---

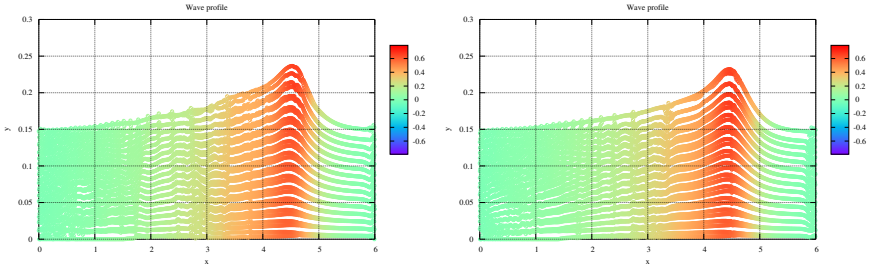

(a) SPH (b) R-SPH

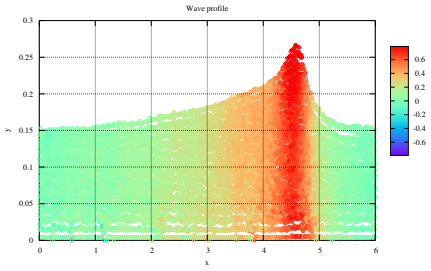

(c) LES-SPH

Figure 6.25: Wave profile, periodic tank, SPH, k=1.5, $t = 2.5$ sec

Interacting solitary waves

Figures 6.26(a)-(e) show the interaction of two solitary waves; in the figures, red indicate higher horizontal velocity. The bigger solitary wave is travelling to the right and the smaller one is travelling to the left. It is expected that the two solitary waves will re-emerge after interaction. We identify the solitons by their amplitude. Roughly 13,000 particles were used for the simulation. The simulation uses the values $\alpha = 0.1$ and $\beta = 0.0$, where α and β are constants in the artificial viscosity (3.18). The simulation was also carried out using R-SPH and LES-SPH.

The amplitudes of the solitons before interaction and after interaction for $\alpha = 0.1$ and $\beta = 0.0$ are given in Table 6.10. "Initial" refers to the wave heights before interaction, "First" and "Second" refers to the wave heights after the first and second interactions in a tank with periodic boundary conditions. Observe that both

Table 6.10: Solitary wave interaction results (SPH, R-SPH)

Wave	Large wave			Small wave		
Interaction	Initial	First	Second	Initial	First	Second
SPH	0.191	0.192	0.194	0.172	0.176	0.178
R-SPH	0.190	0.192	0.193	0.173	0.173	0.173

methods give nearly the same wave heights; also, the wave is steepening slightly. Table 6.11 shows results for SPH with $\alpha = 0.0$ and LES-SPH. Here we see an

Table 6.11: Solitary wave interaction results (SPH, LES-SPH)

Wave	Large wave			Small wave		
Interaction	Initial	First	Second	Initial	First	Second
SPH	0.196	0.198	0.200	0.180	0.180	0.182
LES-SPH	0.196	0.199	0.200	0.179	0.180	0.182

increase in the amplitude of the larger wave. This is likely caused by steepening of the solitary wave. Observe also that LES-SPH and SPH with $\alpha = 0.0$ gives results that are very close to each other.

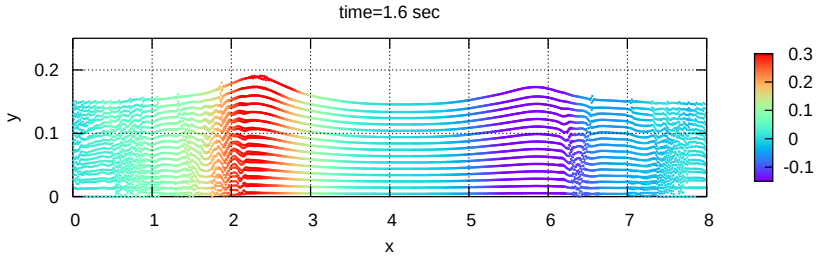

(a) Initial solitons

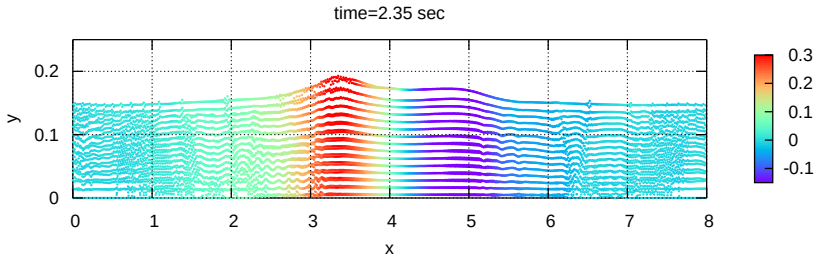

(b) Just before interacting

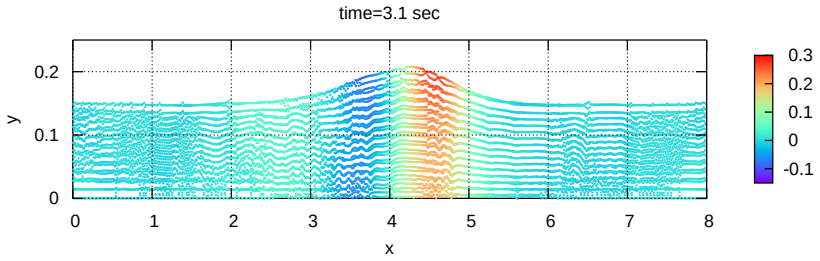

(c) Interacting

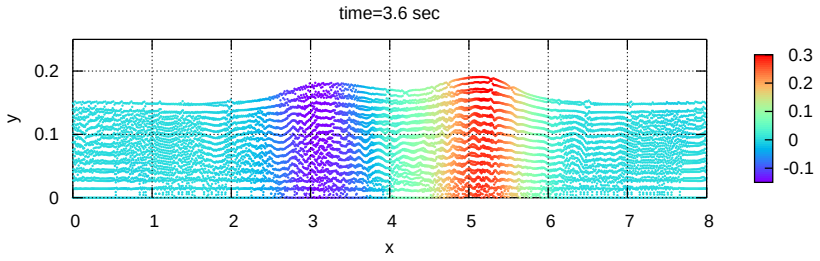

(d) Just after interacting

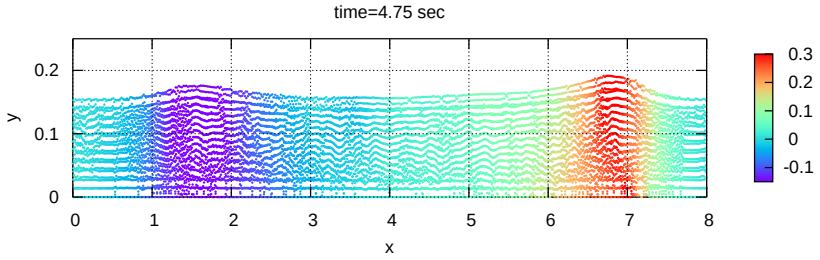

(e) Final solitons

Figure 6.26: Soliton interaction, SPH, $\alpha = 0.1$

Breaking solitary waves

Figures 6.27-6.30 show breaking solitary waves at constant depth; in the figures, red indicate higher horizontal velocity. The initial condition used for this experiment is $k = 2.5$ and $B(k) = 0.35$. The solitary wave formed steepens and eventually breaks.

Figures 6.27(a)-(e) show the simulation using SPH with $\alpha = 0.0$. The figures show the wave before breaking, just before breaking, and just after breaking. Figures 6.28-6.30 show the same experiment using R-SPH and LES-SPH for various values of α; images show only the section of the wave, not the whole domain.

Observe that the wave steepens and breaks faster for the methods LES-SPH and SPH with $\alpha = 0.0$. Table 6.12 shows the time at which the wave breaks for each method. Observe the effect that α has on breaking waves. Higher values of

Table 6.12: Time of soliton breaking

Method	α	Time
SPH	0.1	3.250
R-SPH	0.1	3.375
SPH	0.0	2.550
LES-SPH	0.0	2.575

α delay breaking by a large margin. R-SPH seems to delay breaking even further. For SPH with $\alpha = 0.0$ and LES-SPH, the breaking time is nearly the same.

The differences in the time of wave breaking is also due to the diffusivity. From this simulation, we can conclude that LES-SPH is having a diffusivity that is nearly zero; the LES filter in LES-SPH does not seem to make a significant contribution to diffusivity.

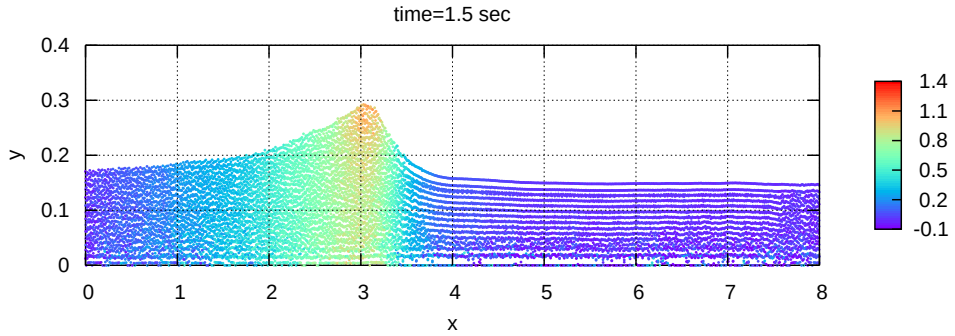

(a) Steepening

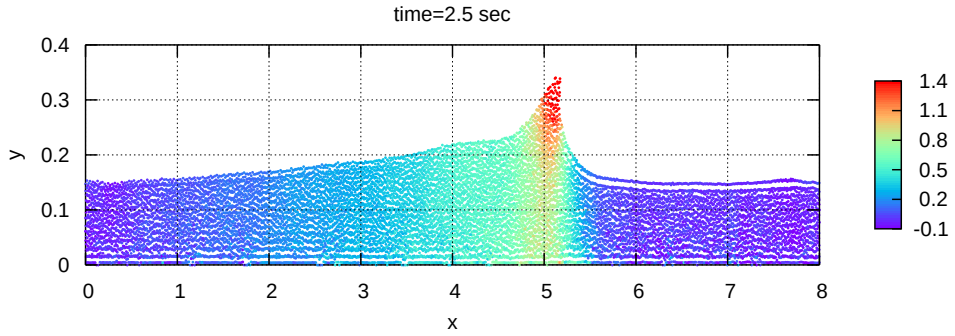

(b) Before breaking

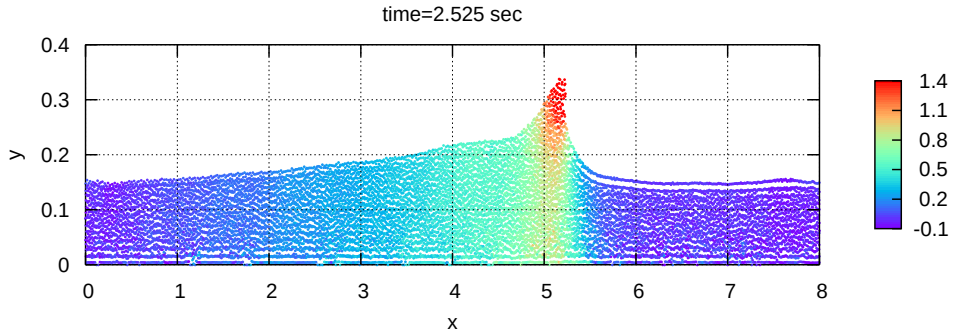

(c) Just before breaking

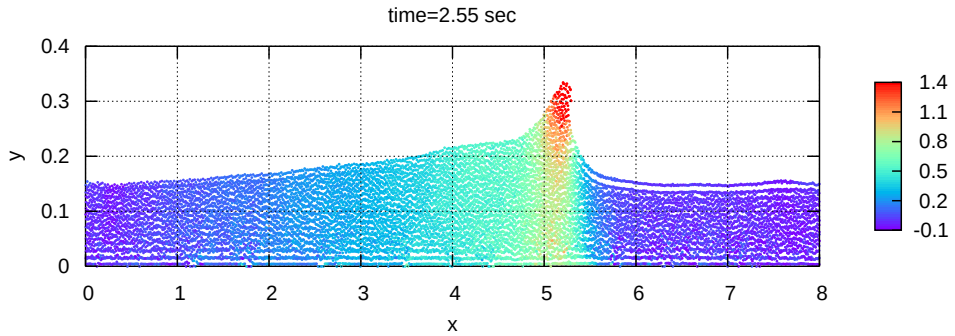

(d) Breaking

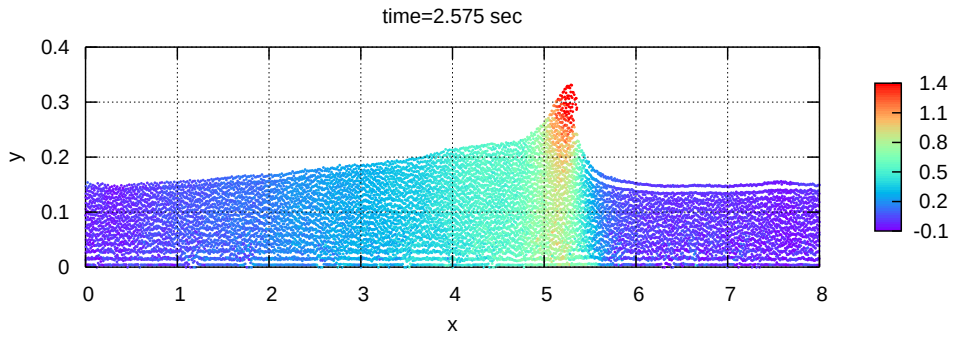

(e) Just after breaking

Figure 6.27: Breaking soliton at a constant depth, SPH, $\alpha = 0.0$

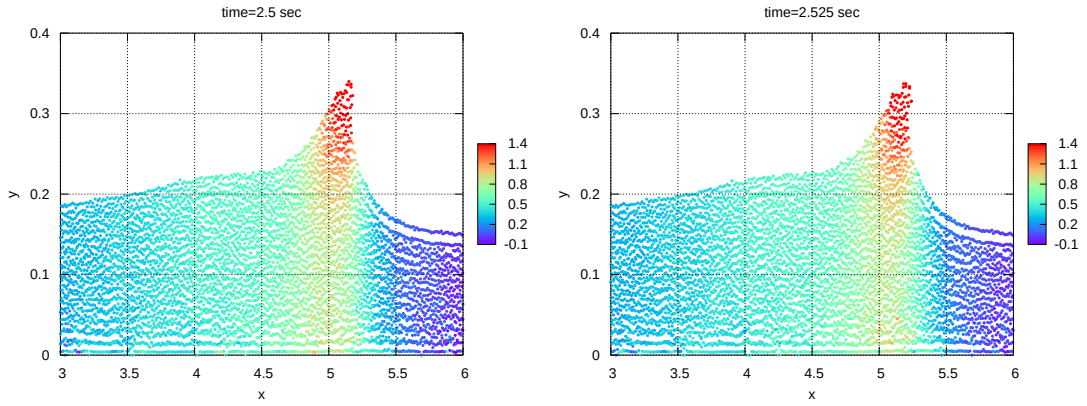

(a) Before breaking

(b) Just before breaking

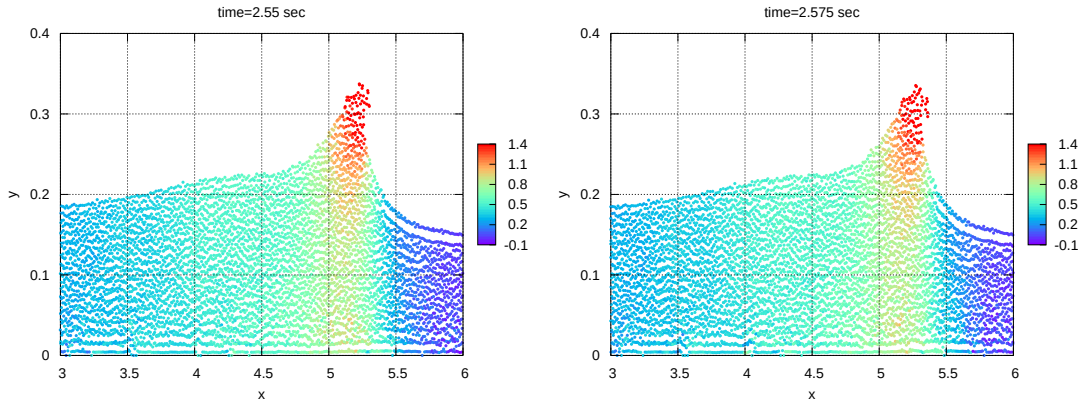

(c) Breaking

(d) Just after breaking

Figure 6.28: Breaking soliton at a constant depth, SPH-LES

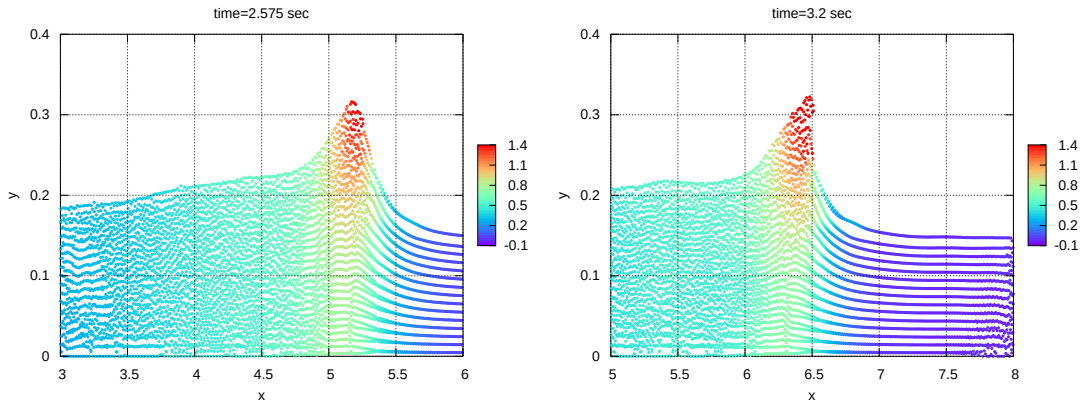

(a) Before breaking

(b) Just before breaking

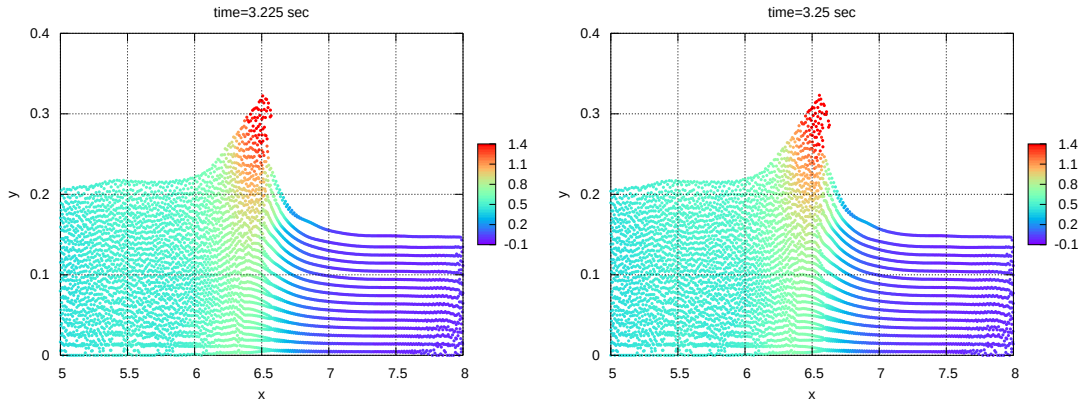

(c) Breaking (d) Just after breaking

Figure 6.29: Breaking soliton at a constant depth, SPH, $\alpha = 0.1$

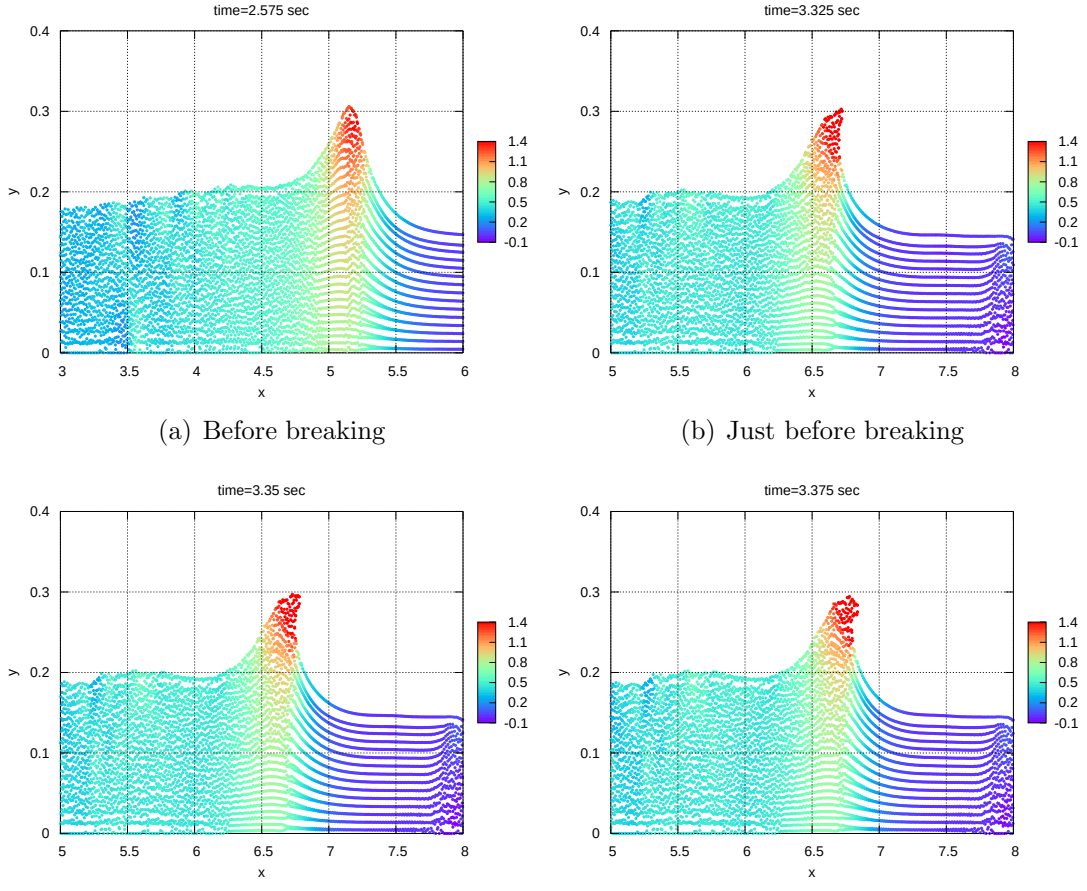

(a) Before breaking (b) Just before breaking

(c) Breaking (d) Just after breaking

Figure 6.30: Breaking soliton at a constant depth, R-SPH, $\alpha = 0.1$

Shoaling solitary waves

For this simulation, the same solitary waves generated with $k = 1.5$, 2.0, and 2.5 in Section 6.4.1 are used. From Section 6.4.1, we know the amplitude of the solitary wave generated for $k = 1.5$, 2.0, and 2.5. The amplitudes of the solitons are again listed in Table 6.13, together with the breaking criteria based on the inequality (6.19).

Table 6.13: Stability of solitary waves in a sloping beach of slope ratio 1 : 8

k	2.0		2.5
Method	SPH	LES-SPH	LES-SPH
Amplitude	0.030	0.060	0.027
A/H	0.20	0.40	0.18
Breaking	No	Yes	No

The values in Table 6.13 indicate that the wave generated with $k = 2.0$ using LES-SPH will break. But Figures 6.31-6.33 show that even the wave generated by $k = 1.5$ does not break for any method, including LES-SPH. Instead it dissipates as a surging wave. In Figures 6.31-6.33, red indicate higher vertical velocity.

Figures 6.34-6.36 show the same waves ($k = 1.5$) in a beach with slope 1:15; in the figures, red indicate higher vertical velocity. Table 6.14 shows whether the wave will break according to (6.19). For the number of particles used, the resolution

Table 6.14: Stability of solitary waves in a sloping beach of slope ratio 1 : 15

k	2.0		2.5
Method	SPH	LES-SPH	LES-SPH
Amplitude	0.030	0.060	0.027
A/H	0.20	0.40	0.18
Breaking	Yes	Yes	Yes

provided by the particle scheme was not enough to check whether the waves for $k = 2.0$ or 2.5 break. This is because the small waves generated for $k = 2.0$ and $k = 2.5$ become less defined close to the inclined plane. As the figures show, the wave generated for $k = 1.5$ breaks for all methods used. The time of breaking is delayed for SPH with $\alpha = 0.1$.

Figures 6.37-6.39 show simulations with an inclined plane of ratio 1:35; in the figures, red indicate higher vertical velocity. As expected, all waves break before reaching the inclined plane. In addition, the dynamics after breaking is different in all methods.

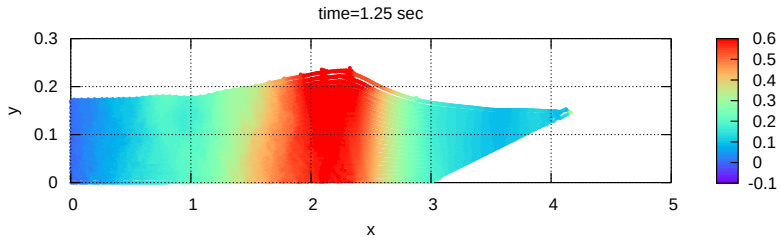

(a) $t = 1.25$ sec

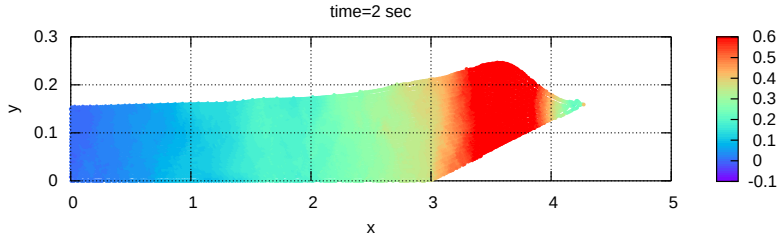

(b) $t = 2.00$ sec

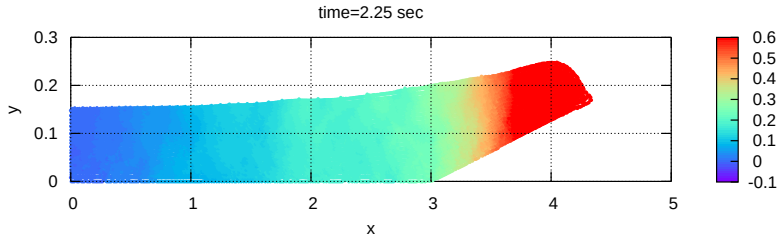

(c) $t = 2.25$ sec

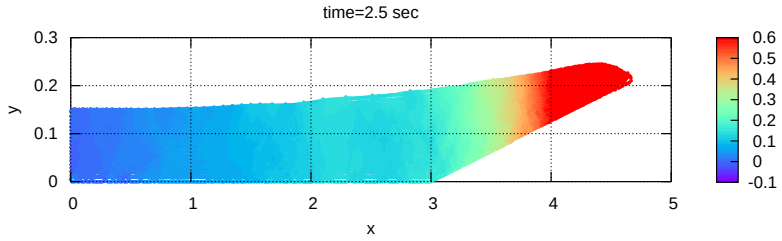

(d) $t = 2.50$ sec

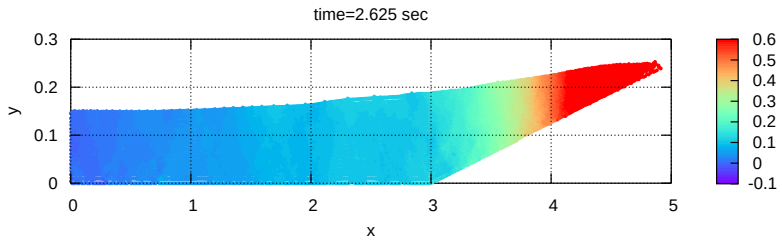

(e) $t = 2.63$ sec

Figure 6.31: SPH, 1:8 slope, $k = 1.5$, $\alpha = 0.1$

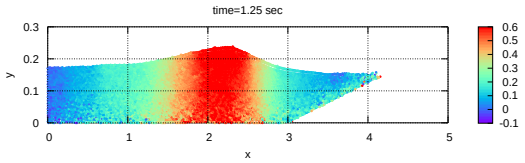

(a) $t = 1.25$ sec

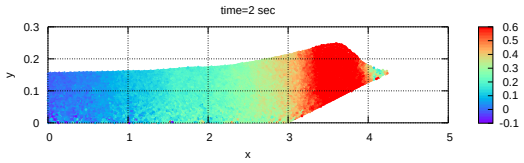

(b) $t = 2.00$ sec

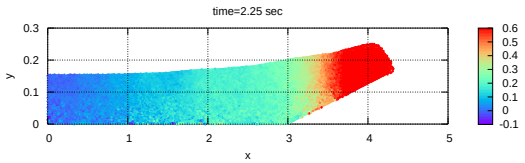

(c) $t = 2.25$ sec

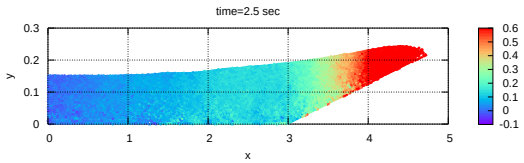

(d) $t = 2.50$ sec

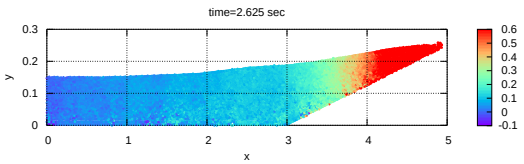

(e) $t = 2.63$ sec

Figure 6.32: SPH, 1:8 slope, $k = 1.5$, $\alpha = 0.0$

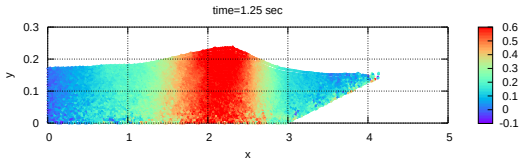

(a) $t = 1.25$ sec

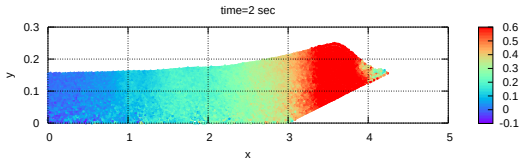

(b) $t = 2.00$ sec

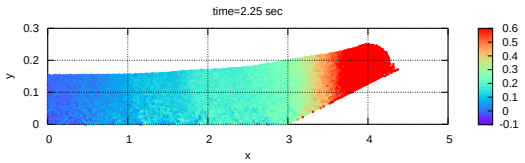

(c) $t = 2.25$ sec

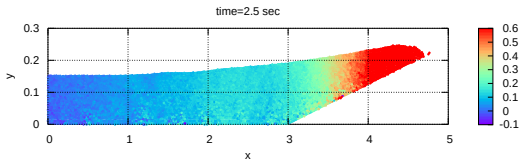

(d) $t = 2.50$ sec

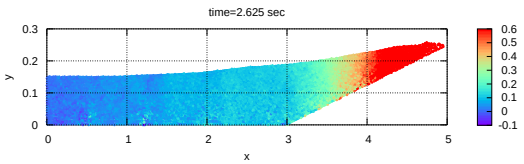

(e) $t = 2.63$ sec

Figure 6.33: LES-SPH, 1:8 slope, $k = 1.5$

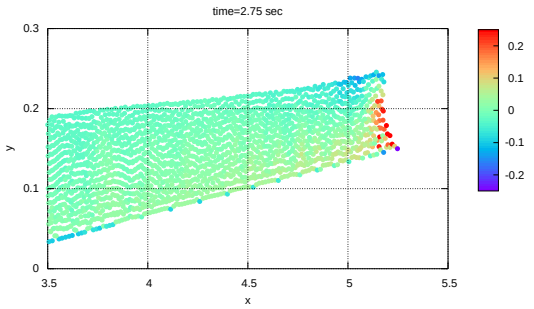

(a) $t = 2.750$ sec

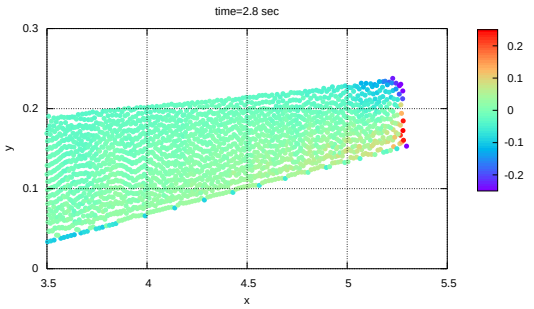

(b) $t = 2.800$ sec

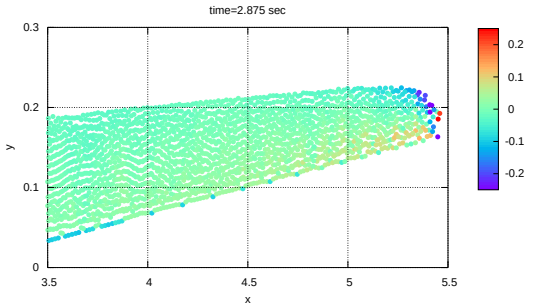

(c) $t = 2.875$ sec

Figure 6.34: SPH, 1:15 slope, $k = 1.5$, $\alpha = 0.1$

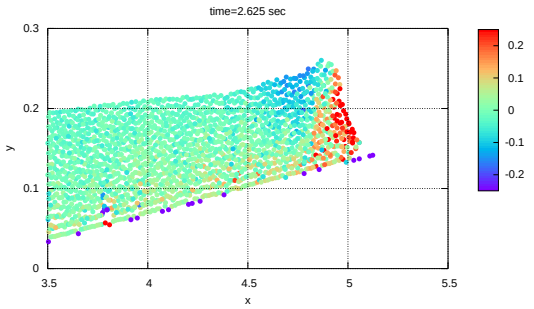

(a) $\alpha = 0.0$, $t = 2.625$ sec

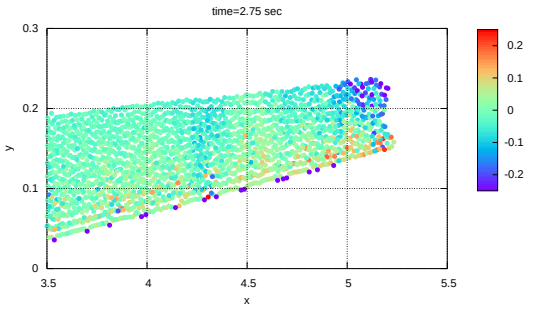

(b) $\alpha = 0.0$, $t = 2.750$ sec

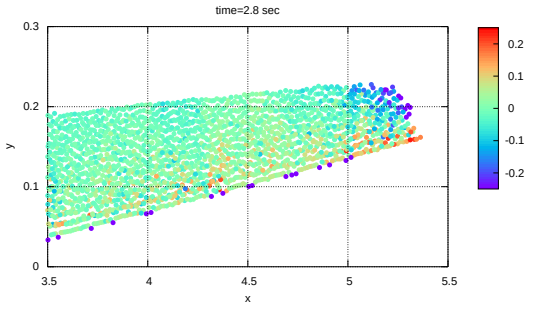

(c) $\alpha = 0.0$, $t = 2.800$ sec

Figure 6.35: SPH, 1:15 slope, $k = 1.5$, $\alpha = 0.0$

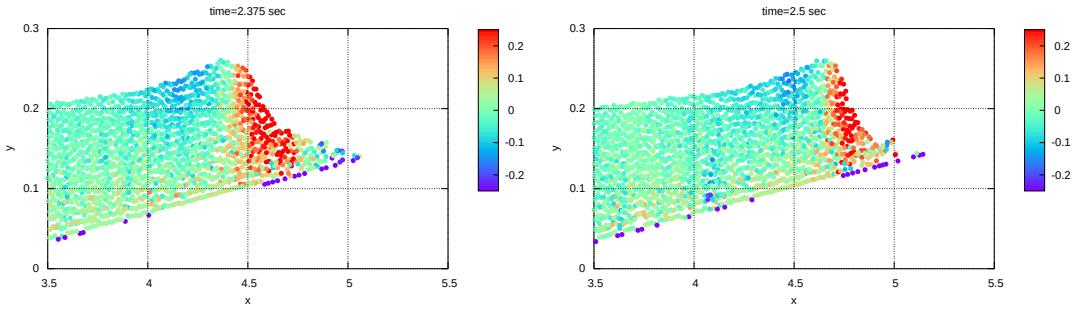

(a) $t = 2.375$ sec (b) $t = 2.500$ sec

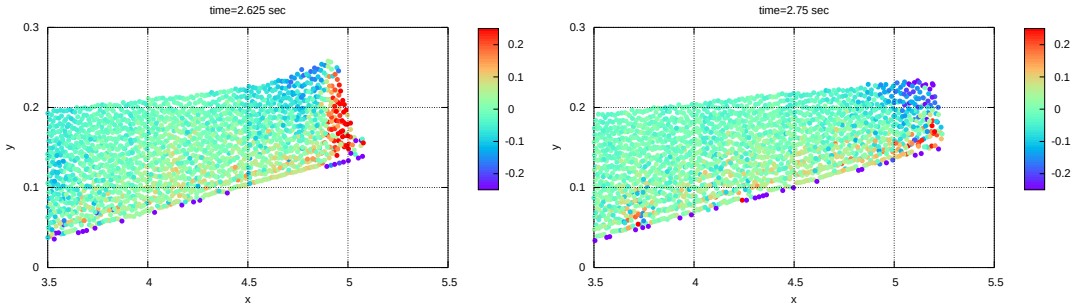

(c) $t = 2.625$ sec (d) $t = 2.750$ sec

Figure 6.36: LES-SPH, 1:15 slope, $k = 1.5$

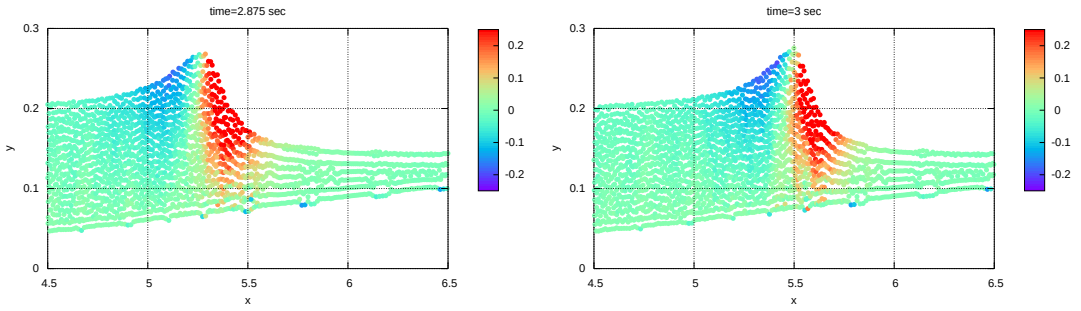

(a) $t = 2.875$ sec (b) $t = 3.000$ sec

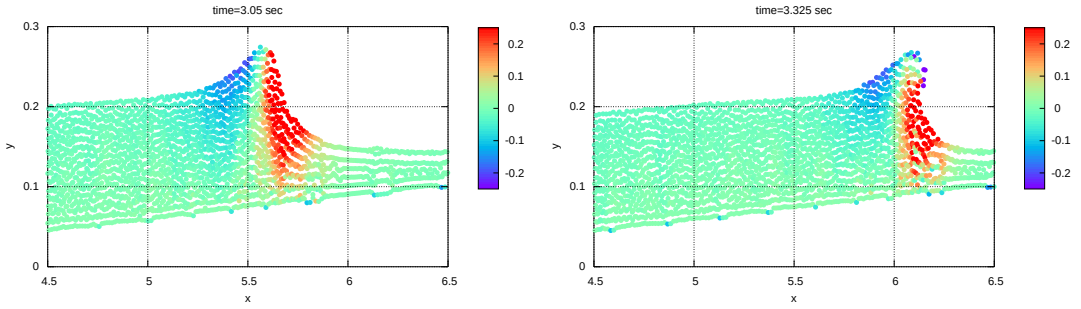

(c) $t = 3.050$ sec (d) $t = 3.325$ sec

Figure 6.37: SPH, 1:35 slope, $k = 1.5$, $\alpha = 0.1$

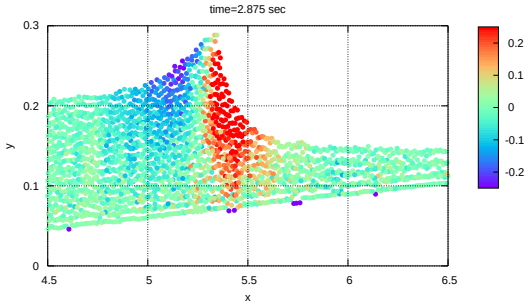

(a) $t = 2.875$ sec

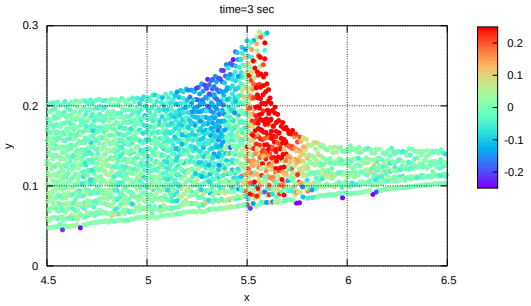

(b) $t = 3.000$ sec

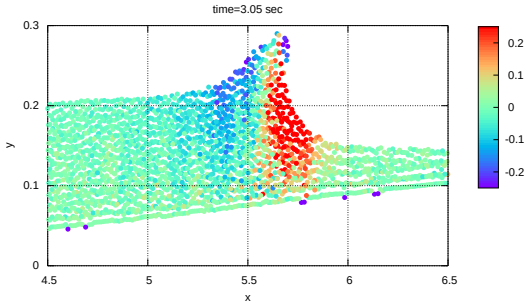

(c) $t = 3.050$ sec

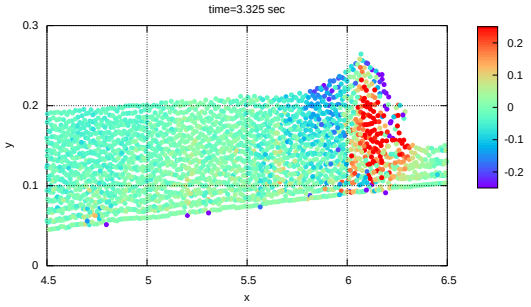

(d) $t = 3.325$ sec

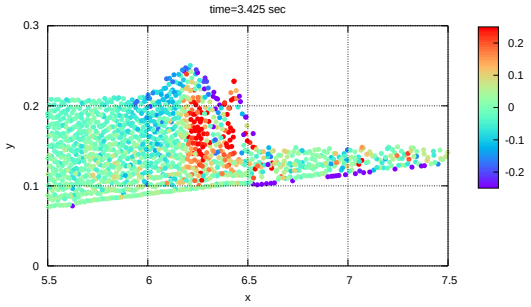

(e) $t = 3.425$ sec

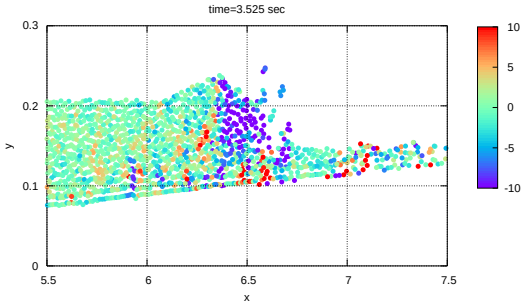

(f) $t = 3.525$ sec

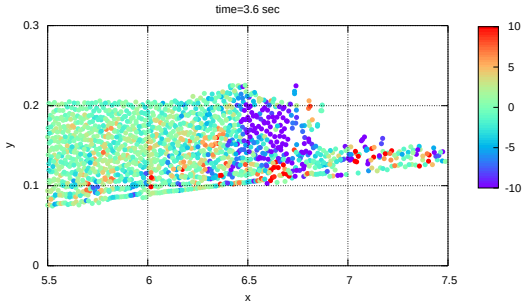

(g) $t = 3.600$ sec

Figure 6.38: SPH, 1:35 slope, $k = 1.5$, $\alpha = 0.0$

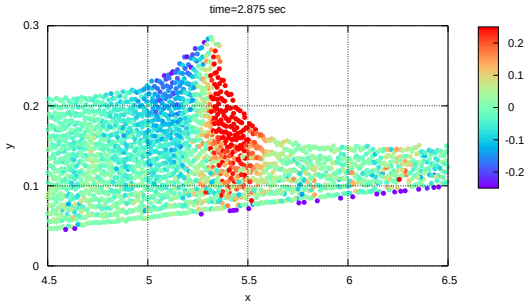

(a) $t = 2.875$ sec

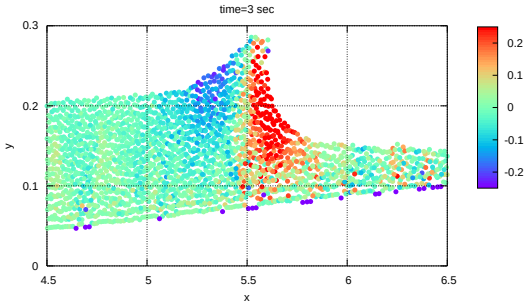

(b) $t = 3.000$ sec

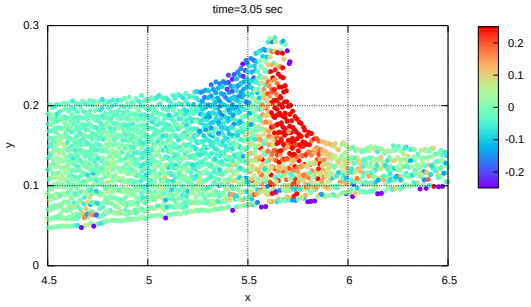

(c) $t = 3.050$ sec

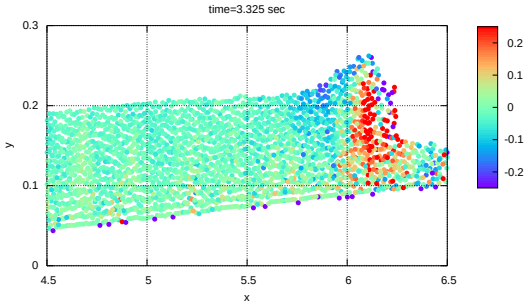

(d) $t = 3.325$ sec

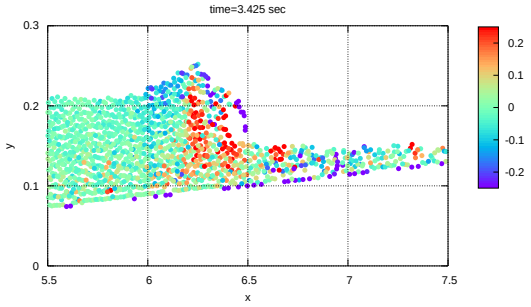

(e) $t = 3.425$ sec

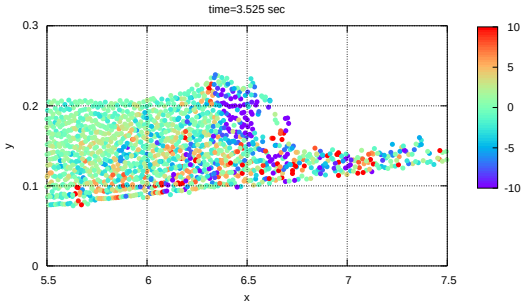

(f) $t = 3.525$ sec

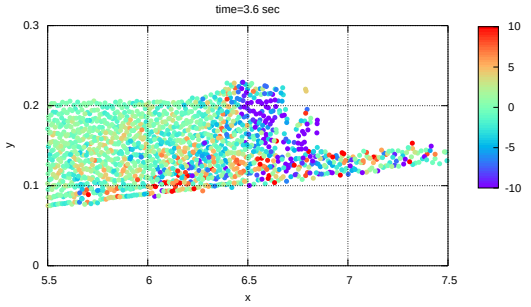

(g) $t = 3.600$ sec

Figure 6.39: LES-SPH, 1:35 slope, $k = 1.5$

6.4.3 Water impact

Here we will observe the effect of the artificial diffusivity in a more dynamic fluid motion. We have seen in Sections 6.4.1 and 6.4.2 that the artificial diffusivity has a significant effect on surface waves. This section shows the change in the evolution of a lump of water upon impacting with the water surface. This simulation is done for the sole purpose of illustrating the way artificial viscosity alters the dynamics significantly. The simulation results are not compared with other experiments or theory. The simulation is carried out using roughly 8000 particles. The time-step used is 1×10^{-5} sec.

A circular-shaped liquid is dropped from a height of 0.5 from the liquid surface. The velocity of the mass of liquid a moment before impact is shown in Figure 6.40. Blue indicates higher vertical velocity and red lower. Observe that the liquid is travelling at a speed of about 3m/s just before impact. Figures 6.41-6.44 show the profile after impact for SPH and R-SPH with $\alpha = 1.0$, 0.0025.

Figures 6.41(a)-(c) show that R-SPH tends to keep the particles together. Observe that the higher diffusivity suppresses the formation of thin surface waves: compare Figures 6.42(a) and (c) taken at $t = 0.74$ with $\alpha = 1.0$ and $\alpha = 0.0025$ respectively. On the other hand, a lower diffusivity is unable to keep particles from breaking away from the liquid body: in Figure 6.42(c) and 6.43(c), observe the way particles are flying off near the edges. Figures 6.45(a)-(c) show how the impact of a few particles rips the surface. The arrow in red indicates a few particles that impact upon the surface, creating a hole on the free-surface. As time progresses, as shown in Figures 6.44(a)-(c), the difference between the evolutions for different values of α is significantly different. This shows that diffusivity plays an important role in surface wave simulations in SPH. Higher diffusivity may result in loss of information.

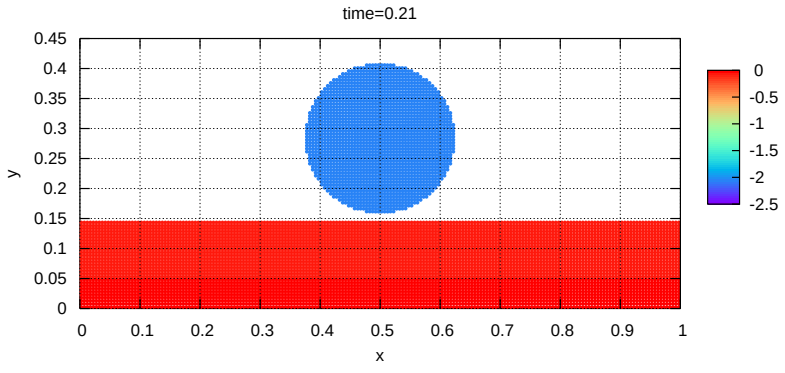

Figure 6.40: Initial profile, SPH, $\alpha = 1.0$

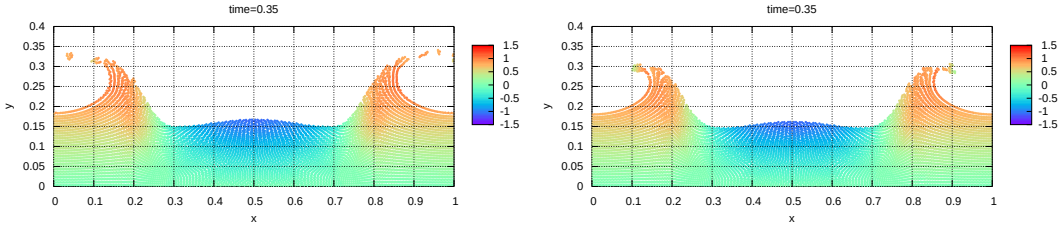

(a) SPH, $\alpha = 1.0$ (b) R-SPH, $\alpha = 1.0$

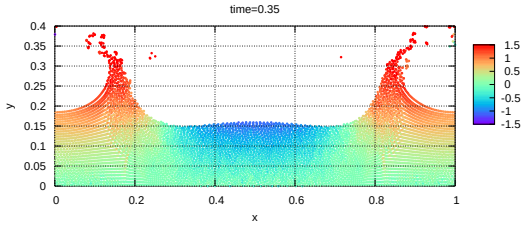

(c) SPH, $\alpha = 0.0025$

Figure 6.41: Water drop, $t = 0.35$ sec

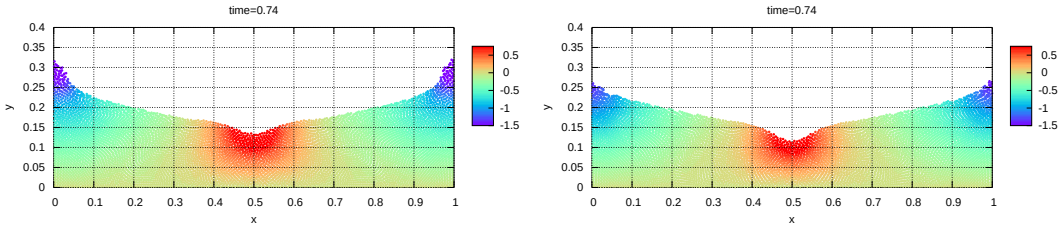

(a) SPH, $\alpha = 1.0$ (b) R-SPH, $\alpha = 1.0$

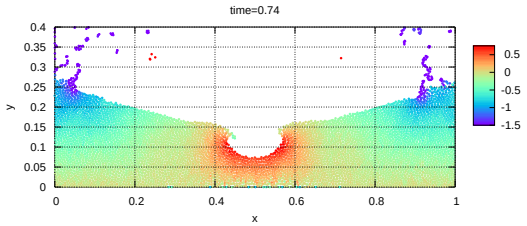

(c) SPH, $\alpha = 0.0025$

Figure 6.42: Water drop, $t = 0.74$ sec

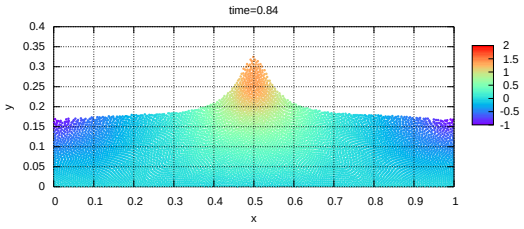

(a) SPH, $\alpha = 1.0$

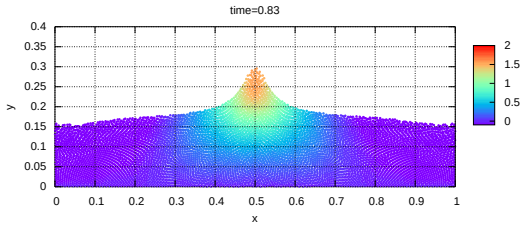

(b) R-SPH, $\alpha = 1.0$

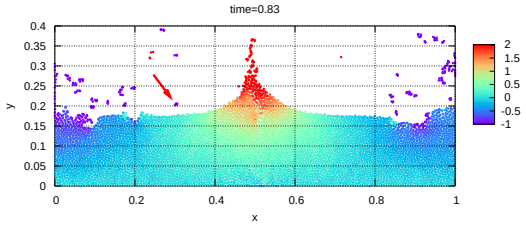

(c) SPH, $\alpha = 0.0025$

Figure 6.43: Water drop, $t = 0.84$ sec

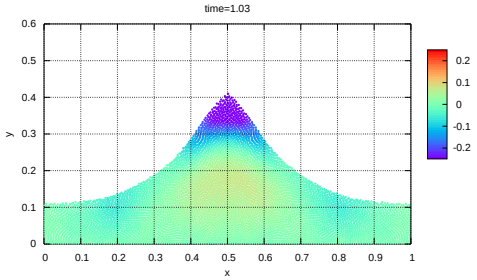

(a) SPH, $\alpha = 1.0$

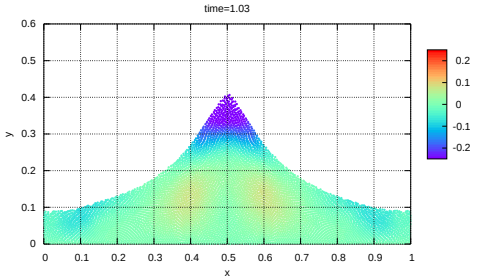

(b) R-SPH, $\alpha = 1.0$

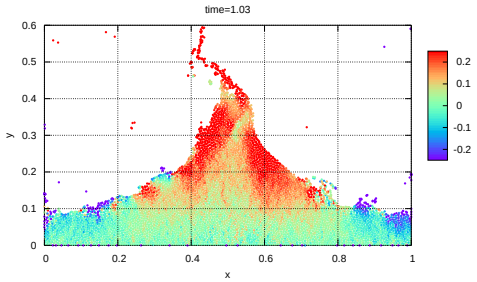

(c) SPH, $\alpha = 0.0025$

Figure 6.44: Water drop, $t = 1.03$ sec

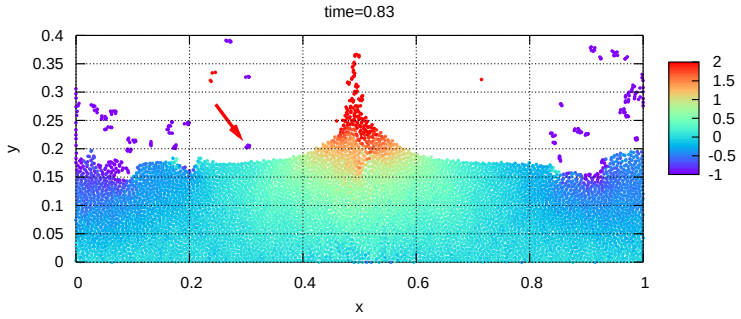

(a) SPH, $t = 0.83$

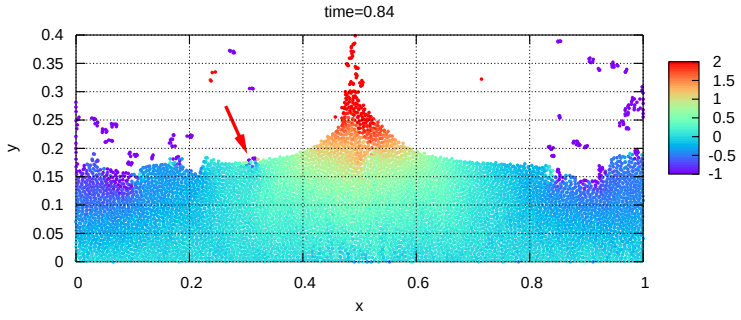

(b) SPH, $t = 0.84$

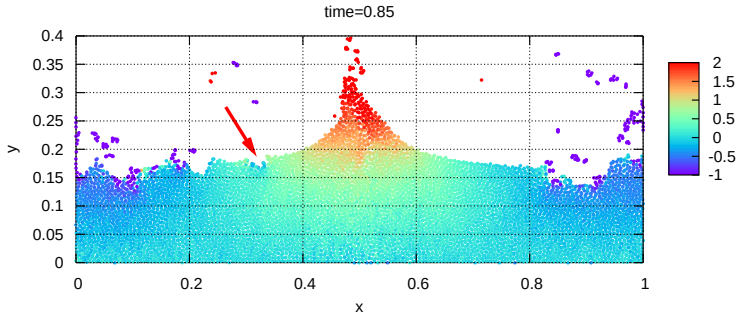

(c) SPH, $t = 0.85$

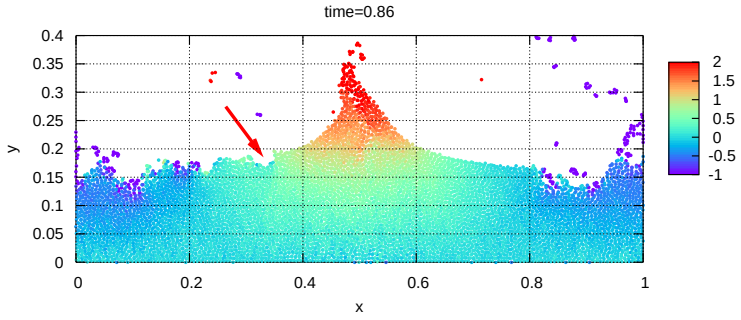

(d) SPH, $t = 0.86$

Figure 6.45: Water drop, water surface rupture, $\alpha = 0.0025$

6.5 Hidden effects

The variation in the water level with time for a tank filled with undisturbed water is shown in Figures 6.46. Again we observe the initial oscillations. The water level eventually reaches a height slightly higher than the initial height. In Figure 6.46(a), S_N indicates the frequency at which the Shepard filter is applied. In all simulations done earlier, $S_N = 40$.

The variation of average density during the initial stages in a tank with undisturbed water is shown in Figure 6.47. The wave like motion is due to the fact that the liquid is slightly compressible, thus giving a spring like initial motion. The scale of this oscillation is small.

The density fluctuations in SPH, R-SPH, and LES-SPH for the simulation of a solitary wave in a long tank are shown in Figure 6.48. In both SPH and R-SPH, density fluctuation remain well within the range $1010 - 990$ kg m^{-3}, the expected range of density fluctuations. But in LES-SPH, density fluctuations are very large, ranging from $940 - 1120$. Thus, for LES-SPH, if density fluctuations are to be kept in the required range, a higher speed of sound may be needed, which in turn requires a small time-stepping.

The maximum density fluctuations in SPH and R-SPH for the simulation of a solitary wave in a long tank is shown in Figure 6.49. Observe that the density fluctuations are slightly higher in R-SPH. Figure 6.50 shows the variation of average density for the same simulation. Observe the fluctuation of average density during the first one or two seconds. Observe also that the average density eventually reaches a value slightly higher than 1000 kg m^{-3}.

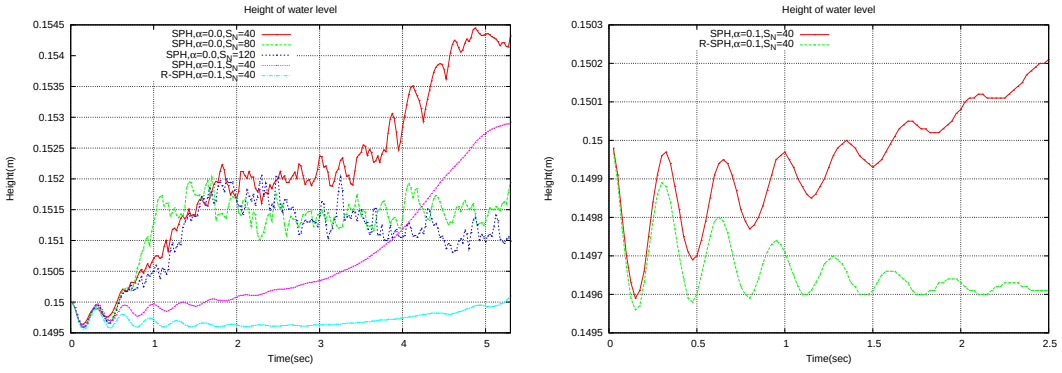

(a) All mothods (b) SPH and R-SPH

Figure 6.46: Variation in water level

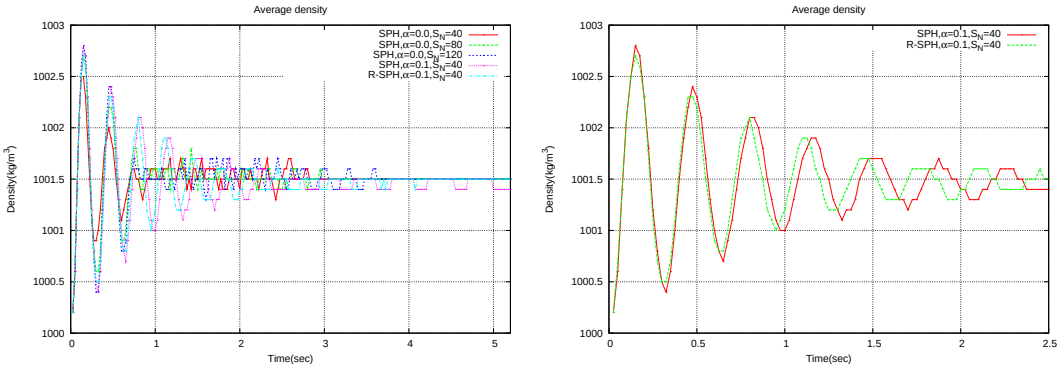

(a) All methods (b) SPH and R-SPH

Figure 6.47: Variation of average density

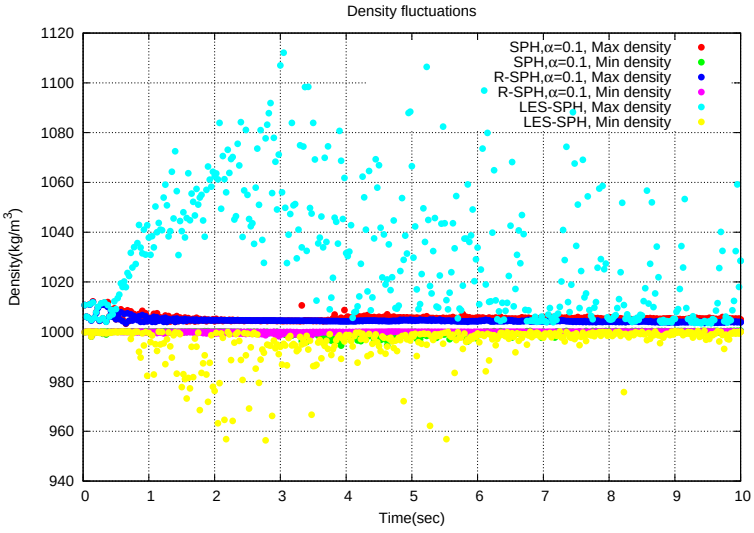

Figure 6.48: Density fluctuations

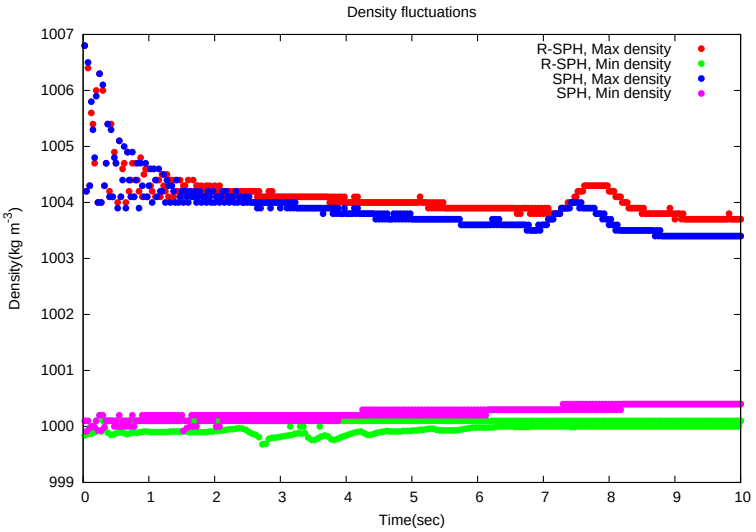

Figure 6.49: Density fluctuations

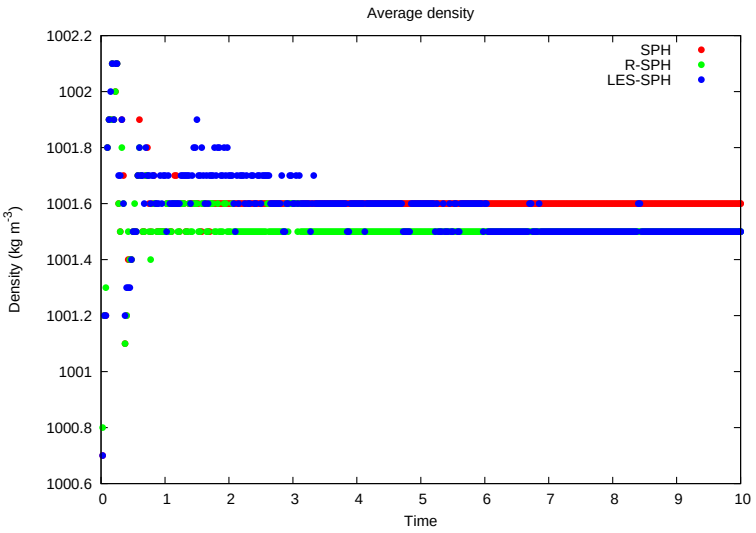

Figure 6.50: Average density

Chapter 7

Conclusions

7.1 Summary

In this thesis, we first presented the basic idea behind particle approximations. Then the important step of obtaining the SP approximation was discussed. The application of the SP approximation to Euler equations led to the notion of particle mass. Direct application of SP approximation to Euler equations gave many different formulae, some of which exhibited non-physical characteristics such as the lack of conservation of momentum and energy. Then it was discussed how equations with conservative properties can be derived. It was also noted that there was no unique way of representing Euler equations using SPH. The direct application of SP approximation to Euler equations was followed by the derivation of the weak formulation. The weak formulation led to equations that had conservative properties. Then it was shown that there was the lack of consistency in SPH. Hence, a method used to restore first order consistency were discussed. It was shown that the R-SPH gives better results for the shock wave problem.

An introductory discussion on LES was given. The application of LES filter to the incompressible Navier-Stokes equations was discussed. The weakly incompressible Navier-Stokes equations were handled by the use of Favre-averaging. If solving the Poisson equation for pressure is to be avoided, SPH requires weak incompressibility. Thus, how water is treated as a weakly incompressible fluid was discussed.

In the section on simulations, the way boundaries are created in SPH was briefly discussed. Some tools used in simulations were also given. For the dam breaking problem, R-SPH method gave a smoother velocity profile. The use of no-slip boundary conditions gave results that are close to experimental data. For 2D free-surface waves, simulations indicated that the LES-SPH method captures fine details of breaking surface waves. Thus, we carried out a controlled simulation using solitons to see how well the LES-SPH method performs when compared to SPH and R-SPH.

The speed of solitary waves was checked. Different SPH methods gave different wave profiles for the same initial conditions. As a result, the wave speeds were

varied for different SPH methods when the same initial conditions were used. The difference in speed was observed to be significantly different if the values of α were significantly different. Given that other parameters are the same, R-SPH had more diffusivity than SPH. For values of α small, SPH gave results close to those of LES-SPH. But, for the wave profile that each method gave, the corresponding speed given by (6.16) was close to the expected value for small values of A/H. R-SPH and LES-SPH showed superior results for speed. The speed was also checked in a tank with periodic boundary conditions. The observed slowdown in the speed of the soliton was slightly larger in R-SPH. A brief discussion was also given for the possible reasons to explain the slowdown of the wave.

For small values of A/H, the soliton shape was also compared with that given by (6.15). The profile given by various SPH formulations was slightly more spread than expected. In addition, the wave boundary of the profile given by LES-SPH was less defined and was also steepening. Steepening is most likely caused by the higher amplitude wave generated by the LES-SPH method.

Then an experiment was run to check the results of two interacting solitary waves. By comparing the height of the solitons, it was observed that soliton interactions are well reproduced by SPH and R-SPH methods. However, in LES-SPH and SPH with $\alpha = 0.0$, the solitary wave steepened slightly. Steepening is mostly likely caused by the high amplitude of the solitary wave created by these two methods.

For breaking solitary waves at a constant depth, the time of breaking was delayed when using SPH and R-SPH with $\alpha = 0.1$. As expected, the delay in the wave breaking was highest for R-SPH. Again, this difference was most likely caused by the difference in the amplitude of the solitary waves formed by the R-SPH and SPH methods. For $\alpha = 0.1$, the solitary waves created were smaller in amplitude, hence taking the longer time to break. A similar trend was observed in shoaling solitary waves in a beach. For waves with smaller A/H, it was difficult to resolve whether or not the wave breaks, due to the low resolution of the numerical method.

On the whole, the R-SPH method did not show marked improvements compared to the SPH method. This is most likely because the fluid is weakly incompressible. Weak incompressibility helps keep the particles at a nearly even distribution, thus not exposing the lack of consistency in SPH. LES-SPH and SPH with small α gave results that were very nearly the same.

Also, it was observed that the density fluctuations in LES-SPH were much higher compared to SPH and R-SPH with $\alpha = 0.1$. Comparing SPH and R-SPH methods, the density fluctuations were lower for the SPH method. Oscillations in density and water height were also observed. Moreover, the water level eventually approached a level higher than the initially assigned height.

Finally, considering all the results, for the resolution used in the simulations, it can be concluded that SPH without any modification is as good as R-SPH or LES-SPH for the simulation of weakly incompressible fluids in 2D.

7.2 Future work

This section will outline some of the problems encountered and possible solutions. Furthermore, some possible extensions to the work done in this thesis will be discussed.

LES filter

As the simulations indicate, and theory predicts, the LES filter is expected to impart turbulence-related effects only in 3D. In 2D, the only visible effect that the LES filtered Navier-Stokes equations showed was an increase in diffusivity. Hence, the code has to be extended to 3D, and effects of the LES filter in 3D have to be investigated. Also, since 3D simulations will require far more memory compared to 2D simulations, ways to optimize the code for speed must be investigated.

Viscosity

For Navier-Stokes equations, as the simulations indicated, the artificial viscosity (3.18) played a major role: results changed significantly depending on the value of α in the artificial viscosity. Investigations need to be carried out to use a natural viscosity, like the viscosity term in the Navier-Stokes equations instead of the usual standard artificial viscosity (3.18) used in SPH. In addition, it will be interesting to investigate how well SPH can simulate fluids with higher viscosity; for fluids with a higher viscosity, it will be possible to remove the use of artificial viscosity while maintaining the smoothness of air-water interface.

Godunov's methods have been recently applied to SPH [4]. The inherent diffusivity present in Godunov's methods could be very small. It is interesting to see how smooth interfaces are when Godunov's method is used in SPH. If the inherent diffusivity in Godunov's method is very small, and if the method can also maintain reasonably smooth interfaces, Godunov's methods will be preferred over basic SPH or R-SPH methods.

Weak incompressibility

It was observed that the assumption of weak incompressibility is a poor approximation, especially when the artificial diffusivity is low. Even if the artificial viscosity is high, the allowed density change of 1 percent is a poor approximation for most liquids. Hence exact incompressibility has to be imposed to obtain more reliable results [13].

Shepard filtering

Shepard filtering was used to make the air-water interface smoother. In simulations with very low diffusivity, there was an indication that Shepard filtering may alter the solution significantly. Hence, methods have to be investigated that will help keep the interfaces smooth while not imparting significant side effects to the solution.

Air-water interface

Simulations can be performed with air above the air-water interface; in the simulations which were done in this thesis, the space above water was empty. For breaking waves, after the wave breaks, the evolution is expected to be different from the solutions obtained in this thesis. Also, techniques have to be developed that can be used to remove the few particles that make the air-water interfaces bumpy.

APPENDICES

A-1 Appendix A

The following integrals will be used in this section.

$$\begin{aligned}
\int_\Omega \frac{x^3}{\|\mathbf{r}\|^2}\psi_x(\mathbf{r}) &= \int_\Omega \frac{x^2(x^2+3y^2)}{\|\mathbf{r}\|^4}\psi(\mathbf{r}) = \frac{1}{4}, \\
\int_\Omega \frac{xy^2}{\|\mathbf{r}\|^2}\psi_x(\mathbf{r}) &= \int_\Omega \frac{y^2(y^2-x^2)}{\|\mathbf{r}\|^4}\psi(\mathbf{r}) = \frac{3}{4}, \\
\int_\Omega x^2\psi_x(\mathbf{r})d\mathbf{r} &= \int_\Omega xy\psi_x(\mathbf{r})d\mathbf{r} = 0.
\end{aligned} \tag{A.1.1}$$

where $\mathbf{r}=(x,y)$, $\frac{\partial\psi_\epsilon(\mathbf{r})}{\partial x}=\psi_x(\mathbf{r})$. Equations (A.1.1) follow from $\int_\Omega \psi(\mathbf{r})d\mathbf{r}=1$ and the symmetry of $\psi(\mathbf{r})$.

Diffusive nature of the artificial viscosity

The explanation will be restricted to 2D.

$$\begin{aligned}
I(\mathbf{r}) &= \sum_j \frac{[\mathbf{u}(\mathbf{r})-\mathbf{u}(\mathbf{r}_j)]\cdot[\mathbf{r}-\mathbf{r}_j]}{\|\mathbf{r}-\mathbf{r}_j\|^2}\nabla\psi_\epsilon(\mathbf{r}-\mathbf{r}_j)\omega_j \\
&\approx \int_\Omega \frac{[\mathbf{u}(\mathbf{r})-\mathbf{u}(\mathbf{r}')]\cdot[\mathbf{r}-\mathbf{r}']}{\|\mathbf{r}-\mathbf{r}'\|^2}\nabla\psi_\epsilon(\mathbf{r}-\mathbf{r}')d\mathbf{r}'.
\end{aligned} \tag{A.1.2}$$

Let $\mathbf{u}=(u,v)$, $I(\mathbf{r})=(I^x(\mathbf{r}),I^y(\mathbf{r}))$, and

$$\begin{aligned}
I^x = &\underbrace{\int_\Omega \frac{(u(\mathbf{r})-u(\mathbf{r}'))(x-x')}{\|\mathbf{r}-\mathbf{r}'\|^2}\psi_x(\mathbf{r}-\mathbf{r}')d\mathbf{r}'}_{I^{x_1}} \\
&+\underbrace{\int_\Omega \frac{(v(\mathbf{r})-v(\mathbf{r}'))(y-y')}{\|\mathbf{r}-\mathbf{r}'\|^2}\psi_x(\mathbf{r}-\mathbf{r}')d\mathbf{r}'}_{I_{x^2}},
\end{aligned} \tag{A.1.3}$$

where $d\mathbf{r}' = dx'dy'$. Using the Taylor expansion about $\mathbf{r}$, we get

$$\begin{aligned} I^{x_1} &= u_x(\mathbf{r}) \int_\Omega \frac{(x'-x)^2}{\|\mathbf{r}-\mathbf{r}'\|^2} \psi_x(\mathbf{r}-\mathbf{r}')d\mathbf{r}' \\ &+u_y(\mathbf{r}) \int_\Omega \frac{(x'-x)(y'-y)}{\|\mathbf{r}-\mathbf{r}'\|^2} \psi_x(\mathbf{r}-\mathbf{r}')d\mathbf{r}' \\ &+\frac{1}{2}u_{xx}(\mathbf{r}) \int_\Omega \frac{(x'-x)^3}{\|\mathbf{r}-\mathbf{r}'\|^2} \psi_x(\mathbf{r}-\mathbf{r}')d\mathbf{r}' \\ &+u_{xy}(\mathbf{r}) \int_\Omega \frac{(x'-x)^2(y'-y)}{\|\mathbf{r}-\mathbf{r}'\|^2} \psi_x(\mathbf{r}-\mathbf{r}')d\mathbf{r}' \\ &+\frac{1}{2}u_{yy}(\mathbf{r}) \int_\Omega \frac{(x'-x)(y'-y)^2}{\|\mathbf{r}-\mathbf{r}'\|^2} \psi_x(\mathbf{r}-\mathbf{r}')d\mathbf{r}' \\ &+O((x'-x)^3, (x'-x)^2(y'-y), (x'-x)(y'-y)^2, (y'-y)^3). \end{aligned} \tag{A.1.4}$$

Using equations (A.1.1), we get

$$\begin{aligned} I^{x_1} &\approx +\frac{1}{2}u_{xx}(\mathbf{r}) \int_\Omega \frac{(x'-x)^3}{\|\mathbf{r}-\mathbf{r}'\|^2} \psi_x(\mathbf{r}-\mathbf{r}')d\mathbf{r}' \\ &\quad +\frac{1}{2}u_{yy}(\mathbf{r}) \int_\Omega \frac{(x'-x)(y'-y)^2}{\|\mathbf{r}-\mathbf{r}'\|^2} \psi_x(\mathbf{r}-\mathbf{r}')d\mathbf{r}' \\ &= \frac{3}{8}u_{xx}(\mathbf{r}) + \frac{1}{8}u_{yy}(\mathbf{r}). \end{aligned} \tag{A.1.5}$$

Similarly, for I^{x_2} we get

$$I^{x_2} \approx \frac{1}{8}v_{xy}(\mathbf{r}). \tag{A.1.6}$$

Therefore,

$$I^{x} \approx \frac{3}{8}u_{xx}(\mathbf{r}) + \frac{1}{8}u_{yy}(\mathbf{r}) + \frac{1}{8}v_{xy}(\mathbf{r}) \tag{A.1.7}$$

Since this term contains diffusive terms, we conclude that $I(\mathbf{r}) = (I^x, I^y)$ has diffusive properties.

Morris' formulation for ∇^2

The explanation will be restricted to 2D. Let

$$I = \sum_j \frac{[u(\mathbf{r}) - u(\mathbf{r}_j)]\,(\mathbf{r}-\mathbf{r}_j)\cdot\nabla\psi(\mathbf{r}-\mathbf{r}_j)\omega_j}{\|\mathbf{r}-\mathbf{r}_j\|^2}$$

$$\approx \underbrace{\int_\Omega \frac{(x-x')}{\|\mathbf{r}-\mathbf{r}'\|^2}\left(u(\mathbf{r})-u(\mathbf{r}')\right)\psi_x(\mathbf{r}-\mathbf{r}')d\mathbf{r}'}_{I^x} + \underbrace{\int_\Omega \frac{(x-x')}{\|\mathbf{r}-\mathbf{r}'\|^2}\left(u(\mathbf{r})-u(\mathbf{r}')\right)\psi_x(\mathbf{r}-\mathbf{r}')d\mathbf{r}'}_{I^y} \quad (A.1.8)$$

Let us now consider

$$I^x = \int_\Omega \frac{(x-x')}{\|\mathbf{r}-\mathbf{r}'\|^2}\left(u(\mathbf{r})-u(\mathbf{r}')\right)\psi_x(\mathbf{r}-\mathbf{r}')d\mathbf{r}'. \quad (A.1.9)$$

Using Taylor expansion about $\mathbf{r}$ for $\mathbf{u}(\mathbf{r})$, we get

$$\begin{aligned} I^x = & u_x(\mathbf{r})\int_\Omega \frac{(x'-x)^2}{\|\mathbf{r}-\mathbf{r}'\|^2}\psi_x(\mathbf{r}-\mathbf{r}')d\mathbf{r} \\ & + u_y(\mathbf{r})\int_\Omega \frac{(x'-x)(y'-y)}{\|\mathbf{r}-\mathbf{r}'\|^2}\psi_x(\mathbf{r}-\mathbf{r}')d\mathbf{r} \\ & + \frac{1}{2}u_{xx}(\mathbf{r})\int_\Omega \frac{(x'-x)^3}{\|\mathbf{r}-\mathbf{r}'\|^2}\psi_x(\mathbf{r}-\mathbf{r}')d\mathbf{r} \\ & + u_{xy}(\mathbf{r})\int_\Omega \frac{(x'-x)^2(y'-y)}{\|\mathbf{r}-\mathbf{r}'\|^2}\psi_x(\mathbf{r}-\mathbf{r}')d\mathbf{r}d\mathbf{r} \\ & + \frac{1}{2}u_{yy}(\mathbf{r})\int_\Omega \frac{(x'-x)(y'-y)^2}{\|\mathbf{r}-\mathbf{r}'\|^2}\psi_x(\mathbf{r}-\mathbf{r}')d\mathbf{r} \\ & + O((x'-x)^3,(x'-x)^2(y'-y),(x'-x)(y'-y)^2,(y'-y)^3). \end{aligned} \quad (A.1.10)$$

Using equations (A.1.1), we get

$$I^x = \frac{1}{8}u_{xx}(\mathbf{r}) + \frac{3}{8}u_{yy}(\mathbf{r}). \quad (A.1.11)$$

Similarly, for the I^y we get

$$I^y = \frac{3}{4}u_{xx}(\mathbf{r}) + \frac{1}{4}u_{yy}(\mathbf{r}). \quad (A.1.12)$$

Therefore

$$I = I^x + I^y = \frac{1}{2}(u_{xx}(\mathbf{r}) + u_{yy}(\mathbf{r})) = \frac{1}{2}\nabla^2 u(\mathbf{r}). \quad (A.1.13)$$

A-2 Appendix B

Artificial viscosity for shockwave treatment

Sharp increases in density, pressure or other quantities of interest occur in nature. For mathematical analysis, these are idealized as discontinuities. Differential equations that govern the physics, like Euler equations, does not directly admit discontinuities.

Let us restrict the explanation to the classic 1D shock tube problem. Discontinuities can be directly handled by differential equations by treating the point of discontinuity as a moving boundary. Either side of the discontinuity is handled by the differential equation, and two regions are connected by Rankine-Hugoniot equation, which is a statement of the conservation laws across a discontinuity. Implementing such boundary conditions over moving shock boundaries in higher dimensions is difficult.

VonNeumann and Richtmyer [21] introduced a method by which discontinuities can be directly handled by Euler equations: by smoothing the discontinuity over a suitably small distance. This smoothing was accomplished by adding an extra pressure term, called the artificial viscosity, to Euler equations:

$$\frac{du}{dt} = -\frac{1}{\rho}\frac{\partial}{\partial x}(p+q), \tag{A.2.1}$$

$$\frac{de}{dt} = -\frac{p+q}{\rho}\frac{\partial u}{\partial x}, \tag{A.2.2}$$

$$\frac{d\rho}{dt} = -\rho\frac{\partial u}{\partial x}. \tag{A.2.3}$$

It is further shown that the expression

$$q = \begin{cases} \beta\rho\left(\Delta x\frac{\partial u}{\partial x}\right)^2, & \text{if } \frac{\partial u}{\partial x} < 0, \\ 0, & \text{otherwise,} \end{cases} \tag{A.2.4}$$

provides the desired smoothness of the discontinuity: q is small over much of the domain due to the term $(\Delta x)^2$, but relatively large near a shock since $\frac{\partial u}{\partial x}$ is large near a shock. $\beta > 0$ is a dimensionless constant used to control the width over which a shock is smoothed and is usually chosen $O(1)$ to spread the shock over a few grid spaces. The restriction $\frac{\partial u}{\partial x} < 0$ is a modification to prevent q been applied to the rarefaction wave.

Viscosity for damping and stability

Compared to VonNeumann viscosity, an artificial viscosity which is less sensitive to $\frac{\partial u}{\partial x}$ is the Landshoff viscosity, which takes the form

$$q = \begin{cases} -\alpha\rho c\Delta x\frac{\partial u}{\partial x}, & \text{if } \frac{\partial u}{\partial x} < 0, \\ 0, & \text{otherwise,} \end{cases} \tag{A.2.5}$$

where c is the speed of sound, and $\alpha > 0$ is a dimensionless constant used to control the diffusivity. This viscosity helps damp out oscillations and, in particular, helps stabilize unstable finite difference schemes. This will also help smooth weak shocks when α is of order $O(1)$, but the diffusivity imparted to the whole domain is significant for this order of α. Hence, in order to use it as an stabilizing diffusivity for unstable numerical schemes, α is often chosen $O(10^{-1})$ or smaller. Here, the restriction $\frac{\partial u}{\partial x} < 0$ is a modification to satisfy the entropy condition.

Viscosity for treating shockwaves and giving stability

Combining (A.2.4) and (A.2.5), we get

$$q = \begin{cases} -\alpha\rho c\Delta x\frac{\partial u}{\partial x} + \beta\rho\left(\Delta x\frac{\partial u}{\partial x}\right)^2, & \text{if } \frac{\partial u}{\partial x} < 0, \\ 0, & \text{otherwise,} \end{cases} \tag{A.2.6}$$

which provides diffusivity to handle shocks and gives stability to unstable finite difference schemes. The first term is dominant outside a shock, and the second is dominant inside a shock.

In situations where there are no strong shocks, we can take $\beta = 0$. In simulations done in this thesis, with the exception of the shocktube problem, there are no shocks involved. Hence, we can safely take $\beta = 0$.

SPH form

In SPH, considering a particle i, Δx is equivalent to the smoothing length ϵ_i, and

$$\frac{\partial u_i}{\partial x} = \sum_j \frac{m_j}{\rho_j}(u_j - u_i)\frac{\partial \psi_{\epsilon_{ij}}}{\partial x}. \tag{A.2.7}$$

But it has been found [7] that this formulation is not good at preventing oscillations at scales smaller than ϵ_i, since it involves averaging over all neighbours. Better results are obtained by using

$$\frac{\partial u_i}{\partial x} = \frac{u_j - u_i}{x_j - x_i}. \tag{A.2.8}$$

To avoid singularities that may arise due to $|x_j - x_i| \ll 0$, (A.2.8) is replaced by

$$\frac{(u_j - u_i)(x_j - x_i)}{|x_j - x_i|^2 + \eta^2}. \tag{A.2.9}$$

Thus, the viscous pressure for a particle i takes the form

$$\Pi_i = -\alpha \rho_i c_i \epsilon_i \frac{(u_j - u_i)(x_j - x_i)}{|x_j - x_i|^2 + \eta^2} + \beta \rho_i \left[\epsilon_i \frac{(u_j - u_i)(x_j - x_i)}{|x_j - x_i|^2} \right]^2. \tag{A.2.10}$$

To ensure symmetry in i, j, ρ_i, c_i, ϵ_i is replaced by $\bar{\rho}_{ij}, \bar{c}_{ij}, \bar{\epsilon}_{ij}$. Furthermore, Π_i is extended to higher dimensions and we get

$$\Pi_{ij} = -\alpha \bar{\rho}_{ij} \bar{c}_{ij} \bar{\epsilon}_{ij} \frac{(\mathbf{u}_j - \mathbf{u}_i) \cdot (\mathbf{x}_j - \mathbf{x}_i)}{|\mathbf{x}_j - \mathbf{x}_i|^2 + \eta^2} + \beta \bar{\rho}_{ij} \left[\bar{\epsilon}_{ij} \frac{(\mathbf{u}_j - \mathbf{u}_i) \cdot (\mathbf{x}_j - \mathbf{x}_i)}{|\mathbf{x}_j - \mathbf{x}_i|^2 + \eta^2} \right]^2 \tag{A.2.11}$$

Note that when $\beta = 0$, Π_{ij} is purely diffusive in 1D. But, as shown in Appendix A, in higher dimensions Π_{ij} is not purely diffusive.

A-3 Appendix C

In this section, we make use of the formula

$$\int_\Omega f(\mathbf{x}) \nabla \cdot \mathbf{F} = \int_{\partial\Omega} f(\mathbf{x}) \mathbf{F} \cdot \hat{\mathbf{n}} dA - \int_\Omega \nabla f(\mathbf{x}) \cdot \mathbf{F} d\mathbf{x}, \tag{A.3.1}$$

where $\Omega \in \mathbb{R}^n$ is an open bounded set with piecewise smooth boundary $\partial\Omega$, $\hat{\mathbf{n}}$ is the outward unit surface normal, f and F are continuously differentiable in the closure of Ω. Consider the model

$$L_{\mathbf{u}}(\Phi) + \nabla \cdot \mathbf{F}(\Phi, \mathbf{x}, t) = S(\Phi, \mathbf{x}, t). \tag{A.3.2}$$

Let the test functions $\phi(\mathbf{x}, t) \in C_0^2(\mathbb{R}^n,]0, T[)$, for some $T > 0$. We look for a solution that satisfies the condition

$$\int_{\mathbb{R}^n \times]0,T[} \left(L_{\mathbf{u}}(\Phi) + \nabla \cdot \mathbf{F}(\Phi, x, t) - S(\Phi, x, t) \right) \phi(x, t) d\mathbf{x} dt = 0, \tag{A.3.3}$$

for all $\phi(\mathbf{x}, t) \in C_0^2(\mathbb{R}^n,]0, T[)$. For clarity, let us consider (A.3.3) in parts:

$$\underbrace{\int_{\Omega \times]0,T[} L_{\mathbf{u}} \phi(\mathbf{x}, t) d\mathbf{x} dt}_{I_L} + \underbrace{\int_{\Omega \times]0,T[} \nabla \cdot \mathbf{F} \phi(\mathbf{x}, t) d\mathbf{x} dt}_{I_F} - \underbrace{\int_{\Omega \times]0,T[} S \phi(\mathbf{x}, t) d\mathbf{x} dt}_{I_S} = 0, \tag{A.3.4}$$

where

$$\begin{aligned} I_L &= \int_{\Omega\times]0,T[} L_{\mathbf{u}}\phi(\mathbf{x},t)d\mathbf{x}dt \\ &= \int_{\Omega\times]0,T[}\left(\frac{\partial\Phi}{\partial t}+\nabla\cdot(\mathbf{u}\Phi)\right)\phi(\mathbf{x},t)d\mathbf{x}dt \\ &= \underbrace{\int_\Omega \Phi\phi(\mathbf{x},t)|_0^T\, d\mathbf{x}}_{*} - \int_\Omega \Phi\frac{\partial\phi}{\partial t}(\mathbf{x},t)d\mathbf{x}dt \\ &\quad + \underbrace{\int_{\partial\Omega\times]0,T[}\Phi\phi(\mathbf{x},t)\mathbf{u}\cdot\hat{\mathbf{n}}dAdt}_{**} - \int_\Omega \nabla\phi\cdot(\mathbf{u}\Phi)d\mathbf{x}dt, \end{aligned} \tag{A.3.5}$$

using (A.3.1), assuming that functions and fields involved are regular enough. Since $\phi(\mathbf{x},t)\in C_0^2(\mathbb{R}^n,]0,T[)$, the terms with label $*$ and $**$ evaluates to zero. Hence

$$\begin{aligned} I_L &= -\int_\Omega \Phi\left(\frac{\partial\phi}{\partial t}+\mathbf{u}\cdot\nabla\phi\right)d\mathbf{x}dt \\ &= -\int_\Omega \Phi\frac{d\phi}{dt}d\mathbf{x}dt \\ &= -\int_{]0,T[}\int_{\mathbb{R}^n}\Phi\frac{d\phi}{dt}d\mathbf{x}dt \\ &\approx -\int_{]0,T[}\sum_j \Phi_j\frac{d\phi_j}{dt}\omega_j dt, \end{aligned} \tag{A.3.6}$$

where the last step is obtained by approximating the spatial component. Using integration by parts we get

$$\begin{aligned} I_L &\approx -\sum_j\left[\phi_j\Phi_j\omega_j|_0^T - \int_{]0,T[}\phi_j\frac{d}{dt}(\Phi_j\omega_j)dt\right] \\ &= \int_{]0,T[}\sum_j\phi_j\frac{d}{dt}(\Phi_j\omega_j)dt. \end{aligned} \tag{A.3.7}$$

By a similar procedure, we get

$$I_F \approx -\int_{]0,T[}\sum_j \mathbf{F}_j\cdot\nabla\phi_j\omega_j dt, \tag{A.3.8}$$

$$I_S \approx \int_{]0,T[}\sum_j S_j\phi_j\omega_j dt. \tag{A.3.9}$$

Thus,

$$I_L+I_F-I_S \approx \sum_j\int_{]0,T[}\left(\phi_j\frac{d}{dt}(\Phi_j\omega_j)-\mathbf{F}_j\cdot\nabla\phi_j\omega_j - S_j\phi_j\omega_j\right)dt. \tag{A.3.10}$$

Now putting the SP approximation

$$\nabla\phi_j \;=\; \sum_k(\phi_k-\phi_j)\nabla_{\mathbf{x}_j}\psi_{\epsilon_{jk}}\omega_k, \tag{A.3.11}$$

we get

$$\begin{aligned} I_L+I_F-I_S &\approx \sum_j\int_{]0,T[}\left(\phi_j\frac{d}{dt}(\Phi_j\omega_j)-\mathbf{F}_j\cdot\sum_k(\phi_k-\phi_j)\nabla_{\mathbf{x}_j}\psi_{\epsilon_{jk}}\omega_k\omega_j-S_j\phi_j\omega_j\right)dt \\ &= \int_{]0,T[}\sum_j\phi_j\frac{d}{dt}(\Phi_j\omega_j)-\int_{]0,T[}\sum_j S_j\phi_j\omega_j dt \\ &- \int_{]0,T[}\left[\underbrace{\sum_j\sum_k\phi_k\mathbf{F}_j\cdot\nabla_{\mathbf{x}_j}\psi_{\epsilon_{jk}}\omega_k\omega_j dt}_{*}-\sum_j\sum_k\phi_j\mathbf{F}_j\cdot\nabla_{\mathbf{x}_j}\psi_{\epsilon_{jk}}\omega_k\omega_j\right]dt. \end{aligned} \tag{A.3.12}$$

Interchanging j and k in the term with label $*$, we get

$$\begin{aligned} I_L+I_F-I_S &\approx \int_{]0,T[}\sum_j\phi_j\frac{d}{dt}(\Phi_j\omega_j)-\int_{]0,T[}\sum_j S_j\phi_j\omega_j dt \\ &- \int_{]0,T[}\left[\sum_j\sum_k\phi_j\mathbf{F}_k\cdot\nabla_{\mathbf{x}_k}\psi_{\epsilon_{kj}}\omega_k\omega_j dt-\sum_j\sum_k\phi_j\mathbf{F}_j\cdot\nabla_{\mathbf{x}_j}\psi_{\epsilon_{jk}}\omega_k\omega_j\right]dt \\ &= \int_{]0,T[}\sum_j\phi_j\frac{d}{dt}(\Phi_j\omega_j)-\int_{]0,T[}\sum_j S_j\phi_j\omega_j dt \\ &\quad+\int_{]0,T[}\sum_j\sum_k\phi_j\left(\mathbf{F}_k+\mathbf{F}_j\right)\cdot\nabla_{\mathbf{x}_k}\psi_{\epsilon_{jk}}\omega_k\omega_j dt \\ &= \int_{]0,T[}\sum_j\left\{\frac{d}{dt}(\Phi_j\omega_j)+\sum_k\left(\mathbf{F}_k+\mathbf{F}_j\right)\nabla_{\mathbf{x}_k}\psi_{\epsilon_{kj}}\omega_k\omega_j-S_j\omega_j\right\}\phi_j dt. \end{aligned} \tag{A.3.13}$$

Assuming that the functions and fields are regular enough, since (A.3.13) tend to zero for any $T>0$ as the partition used for the spatial integral is refined, we get

$$\frac{d}{dt}(\Phi_j\omega_j)+\sum_k\left(\mathbf{F}_k+\mathbf{F}_j\right)\nabla_{\mathbf{x}_k}\psi_{\epsilon_{kj}}\omega_k\omega_j\to S_j\omega_j, \tag{A.3.14}$$

for any $T>0$ as the partition used for the spatial integral is refined.

A-4 Appendix D

Moving Least Square SPH (MLSPH)

MLSPH is a correction to SPH suggested by Dilts [19],[20]. A brief outline of his idea is given in this section. As mentioned before, the aim is to construct a method that can reproduce polynomials exactly. In 3D, linear polynomial reproducibility requires $1, x, y, z$ to be exactly reproducible. Denote the set of polynomials that we aim to reproduce exactly by $\mathbf{p}^T = [1, x, y, x^2, xy, ...]$. Let $u^h(x)$ be the approximation to the set of n data points $\{u_i = u(x_i)|i \in \{1, 2, 3, ...n\}\}$. The best approximation to the data of the form

$$u^h(\mathbf{x}) = \mathbf{p}^T(\mathbf{x}) \cdot \mathbf{a}(\mathbf{x}) \tag{A.4.1}$$

is found, with $\mathbf{a}(\mathbf{x})$ chosen to minimize

$$J = \sum_j \left(\mathbf{p}_j^T \cdot \mathbf{a}(\mathbf{x}) - u_j\right)^2 \psi_\epsilon(\mathbf{x} - (\mathbf{x}_j)), \tag{A.4.2}$$

where $p_j = p(\mathbf{x}_j)$ and ψ_ϵ is a smooth function with compact support. As in SPH, we require ψ_ϵ to be smooth to take the derivatives, and compact support to reduce the computational cost. The solution for $\mathbf{a}(\mathbf{x})$ that minimizes J is given by

$$\mathbf{a}(\mathbf{x}) = A^{-1}(\mathbf{x}) \cdot \sum_j \mathbf{p}_j u_j \psi_\epsilon(\mathbf{x} - (\mathbf{x}_j)), \tag{A.4.3}$$

where $A(\mathbf{x}) = \sum_j \mathbf{p}_j \mathbf{p}_j^T \psi_\epsilon(\mathbf{x} - (\mathbf{x}_j))$. Then $u^h(\mathbf{x})$ is given by

$$u^h(\mathbf{x}) = \sum_j u_j \psi_\epsilon(\mathbf{x} - (\mathbf{x}_j)) \varpi(\mathbf{x}, \mathbf{x}_j), \tag{A.4.4}$$

where $\varpi(\mathbf{x}, (\mathbf{x}_j)) = p(\mathbf{x})^T \cdot A(\mathbf{x})^{-1} \cdot \mathbf{p}(\mathbf{x}_j)$. Comparing equations (A.4.4) and (2.13) and recalling that $\omega_j(t) = \frac{m_j}{\rho_j(t)}$, the volume $\omega_j(t) = \omega(\mathbf{x}_j, t) = \frac{m_j}{\rho_j(t)}$ have been replaced by the volume $\varpi(\mathbf{x}, \mathbf{x}_j) = \mathbf{p}(\mathbf{x})^T \cdot A(\mathbf{x})^{-1} \cdot \mathbf{p}(\mathbf{x}_j)$ in MLSPH. Note that

$$\begin{aligned} \sum_j \mathbf{p}_j^T \psi_\epsilon(\mathbf{x} - (\mathbf{x}_j)) \varpi(\mathbf{x}, \mathbf{x}_j) &= \mathbf{p}^T(\mathbf{x}) \cdot A(\mathbf{x})^{-1} \cdot \sum_j \mathbf{p}_j \mathbf{p}_j^T \psi_\epsilon(\mathbf{x} - \mathbf{x}_j) \varpi(\mathbf{x}, \mathbf{x}_j) \\ &= \mathbf{p}^T(\mathbf{x}) \cdot A(\mathbf{x})^{-1} \cdot A(\mathbf{x}) \\ &= \mathbf{p}^T(\mathbf{x}) \end{aligned} \tag{A.4.5}$$

Hence polynomials are reproduced exactly. In particular, if $\mathbf{p} = [1]$, we get

$$\textstyle\sum_j \psi_\epsilon(x - (x_j)) \varpi(x, x_j) = 1 \quad \text{and} \quad u^h(\mathbf{x}) = \frac{\sum_j u_j \psi_\epsilon(x - x_j)}{\sum_j \psi_\epsilon(x - x_j)}. \tag{A.4.6}$$

If $\mathbf{p} = [1, x, y]$, we get

$$\begin{array}{lll} \sum_j \psi_\epsilon(\mathbf{x} - (\mathbf{x}_j))\varpi(\mathbf{x}, \mathbf{x}_j) = 1 & , & \sum_j x_j \psi_\epsilon(\mathbf{x} - \mathbf{x}_j)\varpi(\mathbf{x}, \mathbf{x}_j) = x \\ \sum_j y_j \psi_\epsilon(\mathbf{x} - (\mathbf{x}_j))\varpi(\mathbf{x}, \mathbf{x}_j) = y & , & \sum_j z_j \psi_\epsilon(\mathbf{x} - \mathbf{x}_j)\varpi(\mathbf{x}, \mathbf{x}_j) = z. \end{array} \tag{A.4.7}$$

Consider the equations written in conservative form

$$\rho \frac{d}{dt}\left(\frac{1}{\rho}\right) = \nabla \cdot \mathbf{u}, \tag{A.4.8}$$

$$\rho \frac{d\mathbf{u}}{dt} = -\nabla p, \tag{A.4.9}$$

$$\rho \frac{dE}{dt} = \nabla \cdot (\mathbf{u}p), \tag{A.4.10}$$

where $\frac{d}{dt}$ is the material derivative, $\mathbf{u} = (u, v)$ is the velocity, and E is the total energy. In 2D, (A.4.8)-(A.4.10) can be written as

$$\rho \frac{d\mathbf{\Phi}}{dt} = \nabla \cdot \mathbf{F}, \tag{A.4.11}$$

where $\mathbf{F} = (F_1, F_2)$,

$$\mathbf{\Phi} = \begin{bmatrix} 1/\rho \\ u \\ v \\ E \end{bmatrix}, \quad F_1 = \begin{bmatrix} u \\ -p \\ 0 \\ up \end{bmatrix}, \quad F_2 = \begin{bmatrix} v \\ 0 \\ -p \\ vp \end{bmatrix}. \tag{A.4.12}$$

For brevity, let us denote $\vartheta_i(x) = \psi_\epsilon(x - x_i)\varpi(x, x_i)$. Galerkin methods is applied to (A.4.11) with $\{\vartheta_i | i \in \{1, 2, 3, ..., n\}\}$ as the basis functions:

$$\begin{aligned} \int_{\Omega(t)} \vartheta_i \rho \frac{d\mathbf{\Phi}}{dt} d\mathbf{x} &= \int_{\Omega(t)} \vartheta_i \nabla \cdot \mathbf{F} d\mathbf{x} \\ &= -\int_{\Omega(t)} \mathbf{F} \cdot \nabla \vartheta_i d\mathbf{x} + \int_{\partial\Omega(t)} \vartheta_i \mathbf{F} \cdot \hat{\mathbf{n}} d\sigma, \end{aligned} \tag{A.4.13}$$

where $\Omega(t)$ is a material volume. The next customary step is to write $u(\mathbf{x}) = \sum_j u_j \vartheta_j(\mathbf{x})$. In order to avoid difficulties arising from non-linearity, the flux $\mathbf{F}$ is expanded directly into

$$\mathbf{F} = \sum_j \mathbf{F}_j \vartheta_j(\mathbf{x}). \tag{A.4.14}$$

Putting (A.4.14) in (A.4.13) and using the one-point approximation

$$\int_\Omega f(\mathbf{x})\vartheta_i(\mathbf{x})dx \approx V_i f(\mathbf{x}_i) \tag{A.4.15}$$

gives

$$m_i \frac{d\mathbf{\Phi}_i}{dt} = \sum_j \mathbf{F}_j \cdot K_{ij}, \tag{A.4.16}$$

$$m_i \frac{d\mathbf{\Phi}_i}{dt} = \sum_j \mathbf{F}_j \cdot \left(-K_{ji} + M_{ij}\right), \tag{A.4.17}$$

where $m_i = V_i \rho_i$, $K_{ij} = \int_{\Omega(t)} \vartheta_i \nabla \vartheta_j$, $M_{ij} = \int_{\partial\Omega(t)} \vartheta_i \vartheta_j \hat{\mathbf{n}}$ and V_i is the volume associated with particle i. Equations (A.4.16) and (A.4.17) do not guarantee local conservation of momentum and energy. By using the relations

$$\textstyle\sum_j K_{ij} = 0 \quad \text{and} \quad \sum_j \left(-K_{ji} + M_{ij}\right) = 0, \tag{A.4.18}$$

(A.4.16), and (A.4.17), a formulation that guarantees local conservation is obtained:

$$m_i \frac{d\mathbf{\Phi}_i}{dt} = \sum_j \frac{1}{2} \left(\mathbf{F}_i + \mathbf{F}_j\right) \left(K_{ij} - K_{ji} + M_{ij}\right). \tag{A.4.19}$$

The final equations with the numerical diffusivity for the MLSPH method is given by

$$m_i \frac{d}{dt}\left(\frac{1}{\rho_i}\right) = \frac{1}{2} \sum_j \left(\mathbf{u}_j - \mathbf{u}_i\right) \cdot \left(K_{ij} - K_{ji} + M_{ij}\right), \tag{A.4.20}$$

$$m_i \frac{d\mathbf{u}_i}{dt} = -\frac{1}{2} \sum_j \left(p_j + p_i + \Pi_{ij}\right) \left(K_{ij} - K_{ji} + M_{ij}\right), \tag{A.4.21}$$

$$m_i \frac{de_i}{dt} = -\frac{1}{2} \sum_j \left(p_j + \frac{1}{2}\Pi_{ij}\right) \left(\mathbf{u}_j - \mathbf{u}_i\right) \cdot \left(K_{ij} - K_{ji} + M_{ij}\right), \tag{A.4.22}$$

where e is the specific internal energy.

Bibliography

[1] Monaghan J.J., Smooth Particle Hydrodynamics, *Annu. Rev. Astro. Astrophys*, 30: 543-74, 1992.

[2] Shaofan Li, Wing Kam Liu, *Meshfree Particle Methods*, Springer-Verlag, 2004.

[3] Blazek J., *Computational Fluid Dynamics: Principles and Applications*, Elsevier, 2001.

[4] Lanson N., Vila J.P., Renormalized Meshfree Schemes I: Consistency, Stability, and Hybrid Methods for Conservation Laws, *SIAM Journal of Numerical Analysis* 1912-1934, 46, Issue 4, 2008.

[5] Monaghan J.J., Smooth Particle Hydrodynamics, Institute of Physics Publishing, Monash University, Rep. Prog. Phys. 68 1703-1759, 2005.

[6] Monaghan J.J., On the Problem of Penetration in Particle Methods, *Journal of Computational Physics*, 82, 1-15, 1989.

[7] Monaghan J.J., Shock Simulation by the Particle Method SPH, *Journal of Computational Physics*, 52, 374-389, 1983.

[8] Morris J.P., Fox P.J., and Zhu Y., Modeling Low Reynolds Number Incompressible Flows Using SPH, *Journal of Computational Physics*, 136, 214-226, 1997.

[9] Dalrymple R. A., Rogers B. D., Numerical modelling of water waves with SPH method, *Coastal Engineering*, 53, 141-147, 2006.

[10] Blin L., Hadjadj A., Vervisch L., Large eddy simulation of turbulent flows in reversing systems *Journal of Turbulence*, 4, N1, 2003.

[11] Bachelor G. K., *An Introduction to Fluid Dynamics*, Cambridge University Press, 1967.

[12] Stephen B. Pope, *Turbulence Flows*, Cambridge University Press, 2000.

[13] Cummins S. J., Rudman M., An SPH Projection Method, *Journal of Computational Physics*, 152, 584-607, 1999.

[14] Vreman B., Geurts B., Kuerten H., Subgrid-Modelling in LES of Compressible Flow, *Applied Scientific Research*, 54, 191-203, 1995.

[15] Lo E., Shao S., Simulation of near-shore solitary wave mechanics by an incompressible SPH method, *Applied Ocean Research*, 24, 275-286, 2002.

[16] Yoshizawa A., Statistical theory for compressible turbulent shear flows, with applications to subgrid modeling, *Physics of Fluids*, Vol. 29, No. 7, 1986.

[17] Monaghan J. J., Simulating Free Surface Flows with SPH, *Journal of Computational Physics*, 110, 399-406, 1994.

[18] Monaghan J. J., Kos A., Solitary Waves on a Cretan Beach, *Journal of Waterway, Port, Coastal, and Ocean Engineering*, 125, No. 3, 145-154, 1999.

[19] Dilts G. A., Moving least-squares particle hydrodynamics I: Consistency and Stability, *International Journal for Numerical Methods in Engineering*, 44, 1115-1155, 1999.

[20] Dilts G. A., Moving least-squares particle hydrodynamics II: conservation and boundaries, *International Journal for Numerical Methods in Engineering*, 48, 1503-1524, 2000.

[21] Von Neumann J, Richtmyer R.D., A Method for the Numerical Calculation of Hydrodynamic Shocks, *Journal of Applied Physics*, 21, 232-237, 1950.

[22] Tanaka M., Dold J.W., Lewy M., Peregrine D. H., Instability and breaking of a solitary wave, *Journal of Fluid Mechanics*, 185, 235-248, 1987.

[23] Grilli S.T., Svendsen I. A., Subramanya R., Breaking Criterion and Characteristics for Solitary Waves on Slopes, *Journal of Waterways, Port, Coastal, and Ocean Engineering*, , 102-112, 1997.

[24] Lusy L. B., A numerical approach to the testing of the fission hypothesis, The Astronomical Journal, 1013-1024, 82, Number 12, 1977.

[25] Gingold R. A., Managhan J. J., MNRAS,181:375.

[26] Oger G., Doring M., Alessandrini B., Ferrant P., Two-dimensional SPH simulation of wedge water entries, *Journal of Computational Physics*, 803-822, 213, 2006.

[27] Colagrossi A., Landrini M., Numerical Simulation of interfacial flows by SPH, *Journal of Computational Physics*, 448-475, 191, 2003.

[28] Shao S., Incompressible SPH simulation of wave breaking and overtopping with turbulence modelling, *International Journal for Numerical Methods in Fluids*, 597-621, 50, 2005.

[29] Edmond Y. M., Shao S., Simulation of near-shore solitary wave mechanics by an incompressible SPH method, *Applied Ocean Research*, 275-286, 24, 2002.